THESIS FOR THE DEGREE OF DOCTOR OF PHILOSOPHY

Microscopic Theory of Externally Tunable Exciton Signatures of Two-Dimensional Materials

Maja Feierabend

Department of Physics

CHALMERS UNIVERSITY OF TECHNOLOGY

Göteborg, Sweden 2021

Microscopic Theory of Externally Tunable Exciton Signatures of Two-Dimensional Materials
Maja Feierabend

ISBN 978-91-7905-471-7
Doktorsavhandlingar vid Chalmers tekniska högskola
Ny serie nr 4938
ISSN 0346-718X

Department of Physics
Chalmers University of Technology
SE-412 96 Göteborg
Sweden
Telephone + 46 (0)31-772 1000

Cover illustration: Activation of dark excitons via molecules.

Printed at Chalmers Reproservice
Göteborg, Sweden 2021

Microscopic Theory of Externally Tunable Exciton Signatures of Two-Dimensional Materials
Maja Feierabend
Department of Physics
Chalmers University of Technology

Abstract

Atomically thin transition metal dichalcogenides (TMDs) are in the focus of current research due to their efficient light-matter interaction and the remarkably strong Coulomb interaction that leads to tightly bound excitons. Due to their unique band structure, TMDs show a variety of *bright* and optically inaccessible *dark* excitonic states. Moreover, the optimal surface-to-volume ratio makes these materials very sensitive to changes in their surroundings, which opens up the possibility of tailoring their optical properties via adsorption of molecules, application of strain, and deposition of defects.

The aim of this thesis is to use a microscopic many-particle theory to predict different strategies to externally control the optical fingerprint of TMDs.

We show that specific molecules can activate dark excitons leading to new pronounced resonances in optical spectra. We also find that these dark states are very sensitive to strain, leading to significant energy shifts and intensity changes. This renders 2D materials suitable for optical sensing of molecules and strain. Moreover, we investigate how local defects due to single molecules or local strain can trap excitons. We show direct signatures of localized bright excitonic states as well as indirect phonon-assisted side bands of localized momentum-dark excitons. We find that the visibility of these localized states is determined by the interplay between defect-induced exciton capture and intervalley exciton–phonon scattering. Finally, we investigate the formation dynamics and optical signatures of spatially separated interlayer excitons at interfaces of acene-based molecular crystals and 2D materials, which play a crucial role for conversion of light to electricity in photodetecting devices.

Overall, the work contributes to a better microscopic understanding of exciton optics and its control via strain, molecules, magnetic fields and impurities in atomically thin semiconductors.

Keywords: transition metal dichalcogenides, density matrix formalism, Bloch equations, dark excitons, strain, localized states, magnetic field, organic/inorganic heterostructures

List of publications

This thesis consists of an introductory text and the following papers:

I. **Optical fingerprint of non-covalently functionalized transition metal dichalcogenides**
M. Feierabend, E. Malic, A. Knorr, and G. Berghaeuser
J. Phys. Condens. Matter 29, 384003 (2017)

II. **Proposal for dark exciton based chemical sensors**
M. Feierabend, G. Berghaeuser, A. Knorr, and E. Malic
Nature Commun. 8, 14776 (2017)

III. **Molecule signatures in photoluminescence spectra of transition metal dichalcogenides**
M. Feierabend, G. Berghaeuser, M. Selig, S. Brem, T. Shegai, S. Eigler, E. Malic
Phys. Rev. Materials 2, 014004 (2018)

IV. **Impact of strain on the optical fingerprint of monolayer transition metal dichalcogenides**
M. Feierabend, A. Morlet, G. Berghaeuser, E. Malic
Phys. Rev. B 96, 045425 (2017)

V. **Dark-exciton based strain sensing in transition metal dichalcogenides**
M. Feierabend, Z. Khatibi, G. Berghaeuser, E. Malic
Physical Review B 99 (19), 195454 (2019)

VI. **Optical fingerprint of bright and dark localized excitonic states in atomically thin 2D materials**
M. Feierabend, S. Brem, E. Malic
Physical Chemistry Chemical Physics 21 (47), 26077-26083 (2019)

VII. **Brightening of spin-and momentum-dark excitons in transition metal dichalcogenides**
M. Feierabend, A. Ekman, S. Brem, E. Malic
2D Mater. 8, 015013 (2020)

VIII. **Dark interlayer excitons in WS_2/tetracene heterostructures**
M. Feierabend, E. Malic
In preparation (2021)

PUBLICATIONS NOT APPENDED IN THIS THESIS:

IX. **A method and a sensor for detecting the presence of molecules with a dipole moment**
M. Feierabend, G. Berghaeuser, A. Knorr, and E. Malic
Patent, WO/2018073356/A1 (2017)

X. **Optical response from functionalized atomically thin nanomaterials**
E. Malic, G. Berghaeuser, M. Feierabend, and A. Knorr
Annalen der Physik 1700097 (2017)

XI. **Dark excitons in transition metal dichalcogenides**
E. Malic, M. Selig, M. Feierabend, S. Brem, D. Christiansen, F. Wendler, A. Knorr, G. Berghaeuser
Phys. Rev. Materials 2, 014002 (2018)

XII. **Disorder-induced broadening of excitonic resonances in transition metal dichalcogenides**
M. Dwedari, S. Brem, M. Feierabend, E. Malic
Phys. Rev. Mat. 3, 074004 (2019)

XIII. **Impact of strain on the excitonic linewidth in transition metal dichalcogenides**
Z. Khatibi, M. Feierabend, M. Selig, S. Brem, C. Linderaelv, P. Erhart, and E. Malic
2D Mater. 6, 015015 (2019)

My contributions to the papers
I.-VIII.: As first-author, I developed the theoretical model, performed the numerical evaluation, analyzed the results and wrote the papers with the help of my main supervisor.
X.-XII.: As co-author, I contributed by performing calculations and helped analyzing the results.
XIII. : As second-author, I contributed by performing calculations, analyzing the results and writing parts of the paper.

Contents

1

Introduction

A material consisting of atoms arranged in a hexagonal lattice and only one atom thick was long considered a purely theoretical construction. Hence the first experimental evidence of graphene, a single layer of carbon atoms, in 2004 by A. Geim and K. Novoselov was a breakthrough, which was rewarded with the Nobel Prize in physics in 2010 [1].

Besides demonstrating incredible strength, thermal and electrical conductance and transparency, graphene paved the way for a new class of materials, the so called 2D materials. Consisting of only a few layers of atoms, these materials show unique properties compared to their 3D counterparts, which brought them into the focus of research. Depending on the involved atoms, a variety of different materials is just waiting to be discovered.

Transition metal dichalcogenides (TMDs) are a promising example, in which a layer of a transition metal (W, Mo, Te) is sandwiched between two layers of chalcogenides (S, Se), see Figure 1.1(a,b). These materials exhibit, in contrast to graphene, a rich band structure with direct and indirect band gaps, and a strong optical response. Moreover, due to their low dimensionality, 2D materials exhibit interesting phenomena such as strongly bound electron-hole pairs, so called excitons, caused by Coulomb interaction [4–9] and sensitivity to their environment due to their optimal surface-to-volume ratio [10–14]. It has been shown that the optical response in TMDs is dominated by excitons [15–17], and hence it is crucial to understand their formation, relaxation and interaction on a microscopic level.

Besides bright (optically accessible) excitons, TMDs also exhibit a variety of dark (optically forbidden) excitons [5, 10, 18–28], which are either spin- or momentum - forbidden, and localized excitons [29–31] due to trapping potentials, see Figure 1.1(c). Moreover, in presence of a second semiconducting layer,

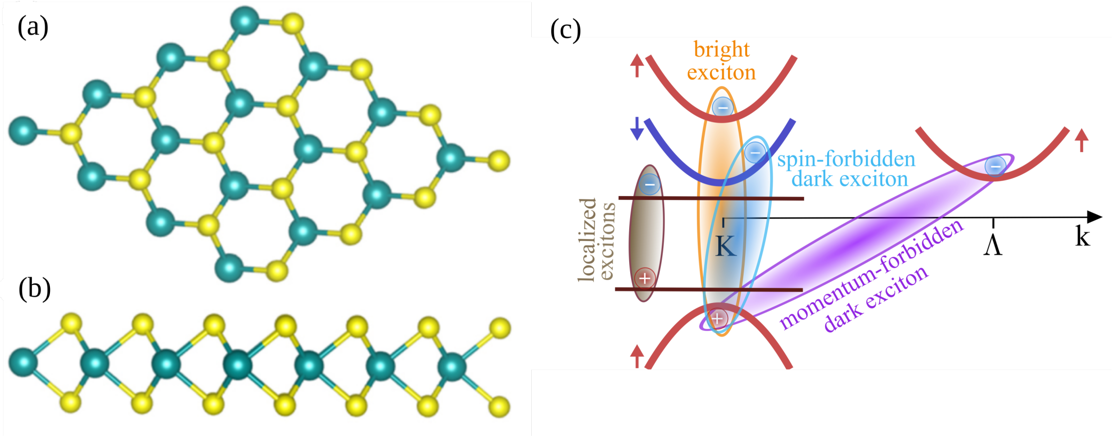

Figure 1.1: **Schematic view of a TMD monolayer and the variety of exccitons.** (a) Top and (b) side view of a transition metal dichalcogenide monolayer, with blue representing M=(Mo,W) atoms and yellow representing X=(S,Se) atoms. Both M and X layers exhibit a honeycomb-like structure, similar to graphene. Figure taken from [2]. (c) Electronic dispersion around the high symmetry K/Λ points in the Brillouin zone. Beside bright excitons (yellow), where both electron and hole have the same spin and momentum, there also exist dark (not optically active) excitons. Dark states can be either spin (blue) or momentum (purple) forbidden. Besides, due to local changes in the band structure, states can appear within the band gap which give rise to the formation of localized excitons (brown). Figure taken from [3].

TMDs can exhibit spatially separated interlayer excitons. Hence, the optical response of TMDs is crucially influenced by the landscape of excitons.

The aim of this thesis is to investigate the interplay of bright, dark, localized and interlayer excitons in TMDs by developing a microscopic framework. Moreover, we show that due to their low dimensionality, TMDs are extremely sensitive to their environment, such as attached molecules, strain and impurities. Within our framework we are able to calculate optical absorption and photoluminescence spectra and the changes associated with it.

The obtained insights shed light on processes on a microscopic level and might inspire future experiments towards technical applications, such as molecule and strain sensing through activation of dark states, single photon emission from localized states, or photosensitive devices based on TMD-organic heterostructures.

1.1 Outline

The aim of this thesis is to investigate the role of excitons on the optical response of TMDs on a microscopic footing by exploiting the intriguing exciton landscape with bright, momentum-dark, spin-dark, localized and even spatially separated interlayer excitons. We introduce the theoretical framework describing TMDs on a microscopic level in Chapter 2 and the excitonic picture with bright and dark excitons in Chapter 3. While bright excitons are easily accessible in experiments, dark excitons are more challenging to access due to their indirect nature.

We propose different mechanisms which can enable the brightening of dark excitonic states in Chapter 4, in particular high-dipole molecules, phonons and magnetic fields. Moreover, in Chapter 5 we discuss strain as an external parameter which allows the tuning of the energetic positions of excitons, and also offers a opportunity to prove indirectly the existence of dark excitons via linewidth changes.

In Chapter 6, we then investigate how bright and dark states behave under a local impurity potential which might stem from local molecules or strain. We apply different trapping potentials and investigate the behaviour of localized excitons and their optical response.

Finally, we explore the interaction of TMDs with a layer of organic molecules in Chapter 7, giving rise to spatially-separated interlayer excitons. We find the appearance of both bright and dark interlayer excitons in the optical response of these heterostructures and look into possibilities to control them by temperature.

1.2 Key Outcomes

PAPER I - III
In these papers, we modelled the interaction between TMDs and molecules with large dipole moments on a microscopic level. We found that the molecules provide an additional center of mass momentum which enables the brightening of dark states. While PAPER I focused on interactions within the K valley and presented a detailed study on molecular characteristics, PAPER II focussed on brightening of the Λ valley. We found an activation of dark states by molecules, which leads to an additional, lower lying peak in optical absorption spectra and opens up the possibility for TMDs as molecular sensors. To account for incoherent processes, we changed from absorption to photoluminescence spectra in PAPER III and found an increased visibility of the dark exciton peak at room temperature. The theoretical approach and central results are summarized in Chapter 4.1.

Motivated by our findings of molecule-activated dark states, we explored the possibility to further tune the relative positions of dark states by external parameters. Strain has been shown to be an effective experimental method to tune the optical signal of TMDs. However, it is not clear to what extend the shift in the optical spectra stems from electronic and excitonic effects. Therefore, we included strain in our theoretical model to see the impact on both excitonic structure and optical response.

PAPER IV-V
In PAPER IV, we found a rather small impact of strain on the excitonic energies and wavefunctions, and hence we can say that the main effect of optical shifts stems from the electronic band gap changes. Motivated by this, we included the valley-dependent electronic band gap shifts, and found that dark and bright valleys respond differently to strain. While bright excitons shift towards higher energies when compressive strain is applied, dark excitons shift to lower energies and thus the absolute difference increases. This opens up great potential for strain sensors as discussed in detail in PAPER V. Our theoretical approach is summarized in Chapter 5.

PAPER VI
In this paper, we looked at the impact of a local impurity potential which can have its origin in local strain or deposited molecules. We find that both bright and dark excitons can be trapped in local potentials leading to a further quantization of the center-of-mass momentum. Moreover, we shed light on the relaxation and trapping dynamics as an interplay of phonon scattering and capture processes. The results are summarized in Chapter 6.

PAPER VII
In this paper, we included spin-dark excitons (electron and hole with different spins) and show that they can be brightened by external magnetic fields. We find that while spin-dark states are dominant in tungsten-based materials, spin- and momentum-dark states (electron and hole with different spin and momentum) are dominant in MoS_2. Our findings explained recent experiments and contribute to a better understanding of the exciton landscape in TMDs. The main results and the theoretical approach are summarized in Chapter 4.3.

PAPER VIII
In our final project, we investigated the possibility of TMD/tetracene as an organic/inorganic heterostructure. Similar to TMD/TMD interactions, we find the appearance of spatially separated interlayer excitons where the electron remains in the TMD and the hole is transferred to the molecular layer. Depending on the location of the electron, we find traces in the optical spectra of both bright and dark interlayer excitons. Our work can contribute to the understanding of organic/inorganic heterostructures and their possible use as photo active devices. We summarize our approach in Chapter 7.

2

Theoretical Framework

The aim of this thesis is to understand the optical properties of TMDs on a microscopic level, in particular the response of the system to an optical excitation. To reach this goal, we use the density matrix formalism to account for the many-particle interactions [6, 32, 33] within the framework of the second quantization. By exploiting the Heisenberg equation of motion we get access to equations of motion for microscopic polarizations and occupations which describe the dynamics of our system.

In the Hamilton operator we include free-particle interactions, Coulomb contributions, interaction with phonons and interaction with external parameters, such as molecules, strain, disorder or magnetic fields [5, 26, 34].

By exploiting the cluster expansion and tight-binding approach we find the TMD Bloch equations which describe the carrier dynamics of the TMD and give access to the optical response. To be able to solve Heisenberg's equation of motion, i.e. $i\hbar\dot{O} = [O, H]$, we need to know the Hamiltonian H of the system and the microscopic quantity of interest O. We will start by introducing the different parts of the Hamiltonian, include TMDs on a microscopic level and then introduce the microscopic quantities of interest.

2.1 Hamilton Operator

Our system can be described by the many-particle Hamiltonian operator $H = H_0 + H_{c-l} + H_{c-c} + H_{c-phon} + H_{c-ext}$ which includes:
(i) the non-interacting carrier contribution

$$H_0 = \sum_{\mathbf{l}} \epsilon_{\mathbf{l}} a_{\mathbf{l}}^{\dagger} a_{\mathbf{l}} + \sum_{\mathbf{q}\sigma} \hbar\omega_{\mathbf{q}} c_{\mathbf{q}}^{\sigma\dagger} c_{\mathbf{q}}^{\sigma} + \sum_{\mathbf{q}\alpha} \hbar\Omega_{\alpha\mathbf{q}} b_{\alpha\mathbf{q}}^{\dagger} b_{\alpha\mathbf{q}} \tag{2.1}$$

with the electronic band structure $\epsilon_{\mathbf{l}}$ [35, 36], electron annihilation (creation) operator $a_{\mathbf{l}}^{(\dagger)}$ with momentum $\mathbf{k}_l$, band λ_l and spin s_l; photon annihilation (creation) operator $c_{\mathbf{q}}^{(\dagger)}$ with mode σ; and phonon annihilation (creation operators) $b_{\alpha\mathbf{q}}^{(\dagger)}$ with phonon energy $\Omega_{\alpha\mathbf{q}}$ and phonon mode α;
(ii) the carrier-light interaction

$$\begin{aligned} H_{c-l} &= \frac{i\hbar e_0}{m_0}\sum_{\mathbf{l}_1\mathbf{l}_2}\mathbf{M}_{\mathbf{l}_1\mathbf{l}_2}\mathbf{A}(t)a_{\mathbf{l}_1}^{\dagger}a_{\mathbf{l}_2} && (2.2)\\ &= \frac{i\hbar e_0}{m_0}\sum_{\mathbf{l}_1\mathbf{l}_2\mathbf{q}\sigma}\left(M_{\mathbf{q}}^{\sigma}a_{\mathbf{l}_1}^{\dagger}a_{\mathbf{l}_2}c_{\mathbf{q}}^{\sigma}+\text{h.c.}\right) && (2.3)\end{aligned}$$

with the electron mass m_0, elementary charge e_0 and the optical matrix element $\mathbf{M}_{\mathbf{l}_1\mathbf{l}_2}$. Note that the first line is in the coherent limit where we use $\mathbf{A}(\mathbf{r},t) \approx \mathbf{A}(t)$ (semi-classical approach) and is used to calculate absorption spectra. The second line includes carrier-photon interaction and therefore represents the full quantum mechanical expression for the interaction with light. The full quantum mechanical expression is needed to calculate the photoluminescence spectra. We used $M_{\mathbf{q}}^{\sigma} = \sqrt{\frac{\hbar}{2\epsilon_0 L^3\omega_q}}\mathbf{e}_{\sigma\mathbf{q}}\mathbf{M}_{\mathbf{l}_1\mathbf{l}_2}$. For details on the optical matrix elements see [5] or the theory part in PAPER III or PAPER IV; .
(iii) the carrier-carrier interaction

$$H_{c-c} = \frac{1}{2}\sum_{\mathbf{l}_1\mathbf{l}_2\mathbf{l}_3\mathbf{l}_4} V_{\mathbf{l}_3\mathbf{l}_4}^{\mathbf{l}_1\mathbf{l}_2}a_{\mathbf{l}_1}^{\dagger}a_{\mathbf{l}_2}^{\dagger}a_{\mathbf{l}_4}a_{\mathbf{l}_3} \tag{2.4}$$

with Coulomb matrix element $V_{\mathbf{l}_3\mathbf{l}_4}^{\mathbf{l}_1\mathbf{l}_2}$ which we treat with a TMD specific screening function to account for the low dimensionality of the TMD [5, 37]. We will further discuss it in section 3.1;
(iv) the carrier-phonon interaction

$$H_{c-phon} = \sum_{\alpha\mathbf{l}_1\mathbf{l}_2} G_{\mathbf{l}_1\mathbf{l}_2\mathbf{q}}^{\alpha}a_{\mathbf{l}_1}^{\dagger}a_{\mathbf{l}_2}(b_{\mathbf{q}}^{\alpha}+b_{-\mathbf{q}}^{\alpha\dagger}) \tag{2.5}$$

which describes the interaction of carriers and phonons with electron-phonon coupling element $G_{\mathbf{l}_1\mathbf{l}_2\mathbf{q}}^{\alpha}$. It will be discussed in detail in section 4.2.1; and
(v) the carrier-external impurity interaction

$$H_{c-ext} = \sum_{\mathbf{l}_1\mathbf{l}_2} D_{\mathbf{l}_1\mathbf{l}_2}a_{\mathbf{l}_1}^{\dagger}a_{\mathbf{l}_2} \tag{2.6}$$

with impurity coupling element $D_{\mathbf{l}_1\mathbf{l}_2}$ where the exact form of the coupling element depends on the form of impurities, and can be due to molecules (sec. 4.1.1), magnetic fields (sec. 4.3.1) or trapping potentials (sec. 6.1). Note that the impurity coupling element is written here in a very general form and can include both momentum and spin transfer, i.e. $k_1 \neq k_2$ and $s_1 \neq s_2$.

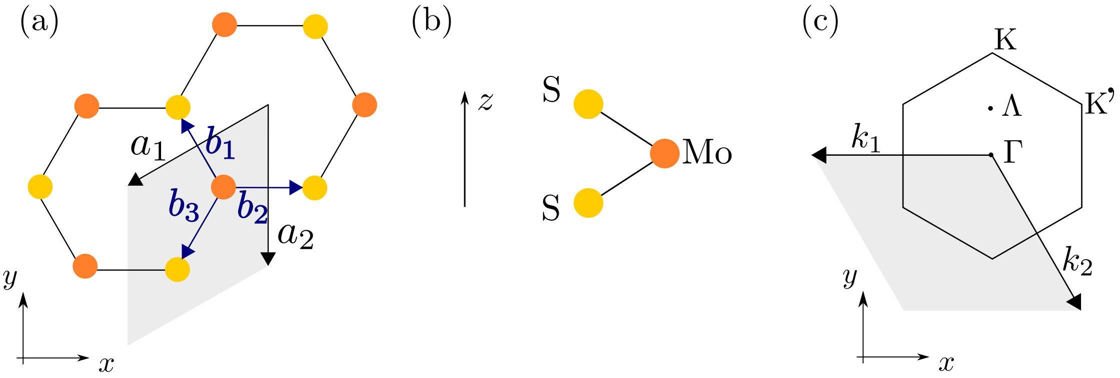

Figure 2.1: **Schematic view to the MoS$_2$ layer.** In (a) we see the honeycomb-like structure in real space in the xy plane with Molybdenum atoms in orange and sulfide atoms in yellow. Furthermore one can see the primitive cell in gray which is a rhombus as typically for hexagonal lattice structure and primitive vectors $\mathbf{a_1}$ and $\mathbf{a_2}$. Moreover we see the fundamental vectors $\mathbf{b_j}$ connecting Mo-and S-atoms. The structure is quasi 2D meaning that the height in z direction, cf. (b), is negligibly small compared to the bulk, here ≈ 0.3 nm. In (c) one can see the momentum space representation with reciprocal lattice and lattice vectors k_1 and k_2 and the high symmetry points K, K′, Γ and Λ.

All coupling elements, i.e. the optical coupling element $\mathbf{M}_{\mathbf{l_1 l_2}} = \langle \psi_{\boldsymbol{l_1}}(\boldsymbol{r})|\mathbf{p}|\psi_{\boldsymbol{l_2}}(\boldsymbol{r})\rangle$, the Coulomb coupling element $V^{\mathbf{l_1 l_2}}_{\mathbf{l_3 l_4}} = \langle \psi_{l_1}(\boldsymbol{r})\psi_{l_2}(\boldsymbol{r'})|V(\boldsymbol{r'} - \boldsymbol{r'})|\psi_{l_3}(\boldsymbol{r'})\psi_{l_4}(\boldsymbol{r})\rangle$, the phonon coupling element $G^{\alpha}_{\mathbf{l_1 l_2 q}} = \langle \psi_{l_1}(\boldsymbol{r})|\phi^{\alpha}_{pho}(\mathbf{r})|\psi_{l_2}(\boldsymbol{r})\rangle$ and the impurity coupling element $D_{\mathbf{l_1 l_2}} = \langle \psi_{l_1}(\boldsymbol{r})|\phi_{ext}(\mathbf{r})|\psi_{l_2}(\boldsymbol{r})\rangle$ are calculated by exploiting the nearest-neighbor tight binding approach [6, 32, 38] which we will discuss in the next section and classical potential, which we will discuss in detail in chapter 3 and 4. Now, we want to briefly introduce the TMDs lattice structure and the used tight-binding approach.

2.2 TMD Band Structure

Transition metal dichalcogenides (TMDs) consist of a layer of transition metal atoms (Mo, W) sandwiched between two layers of dichalcogenides (S, Se, T). Even though they have some dimension in z-direction (around 0.3 nm) and are not truly one-layer thick, they are quasi two-dimensional and widely referred to as 2D materials. The investigated TMDs are all semiconductors with band gaps in the range of 1.5 - 2.5 eV [17, 39, 40].

In comparison to graphene, TMD monolayer consist of two sub-lattices, cf. Fig. 2.1(a), one from the transition metal and one from the dichalcogenide. They both exhibit a hexagonal lattice and hence the S-lattice can be described simply by a translation of the Mo-lattice. The lattice in real space is described by primitive vectors $\mathbf{a}_1 = -\frac{a_0}{2}\begin{pmatrix}\sqrt{3}\\1\end{pmatrix}$ and $\mathbf{a}_2 = -a_0\begin{pmatrix}0\\1\end{pmatrix}$. with lattice constant a_0. For the primitive vectors in the momentum representation, cf. Fig. 2.1(c), one finds

$$\mathbf{k}_1 = -\frac{\pi}{a_0}\begin{pmatrix}\frac{4}{\sqrt{3}}\\0\end{pmatrix}, \qquad \mathbf{k}_2 = \frac{\pi}{a_0}\begin{pmatrix}\frac{2}{\sqrt{3}}\\-2\end{pmatrix}. \tag{2.7}$$

Moreover, Fig.2.1(c) shows the most important symmetry points, namely K, K′, Γ and Λ. Due to the two sub-lattices, the inversion symmetry is broken and a direct band gap appears at the high symmetry K point. The electronic dispersion around the high symmetry points can be approximated by a parabolic band.

Electronic dispersion

To obtain the parabolic dispersion of the TMD structure one needs to solve Schrödinger's equation

$$H\Psi_{\mathbf{l}} = \epsilon_{\mathbf{l}}\Psi_{\mathbf{l}} \tag{2.8}$$

for the 2N particle system. We can make use of the tight-binding approach [5] which reads in the nearest-neighbor approximation:

$$\Psi_{\mathbf{l}}(\mathbf{k},\mathbf{r}) = \frac{1}{\sqrt{N}}\sum_{j=\text{Mo,S}} C^{\mathbf{l}}_j \sum_{\mathbf{R_j}} e^{i\mathbf{k}\cdot\mathbf{R}_j}\phi^{\mathbf{l}}_j(\mathbf{r}-\mathbf{R}_j) \tag{2.9}$$

with N number of atoms, $C^{\mathbf{l}}_j$ the so called tight-binding coefficients, atomic orbitals $\phi^{\mathbf{l}}_j(\mathbf{r}-\mathbf{R}_j)$ and vector $\mathbf{R}_j$ denoting the position of the atom within the sublattice j. Remember that we have a broken symmetry for K/K′ points which means we have to solve Eq. (2.8) separately for both points, including also the two sub-lattices for Mo and S this leads us to four linear equations one has to solve. Close to the high-symmetry points one finds within a Taylor approximation for the electronic dispersion

$$\epsilon^{\mathbf{l}}_{\nu} \approx \pm\left(\frac{\Delta E^{\lambda s}_{\nu}}{2} + \frac{3|\nu t^{\lambda s}|^2}{4E^{\lambda s}_{\nu}}\mathbf{k}^2\right) \tag{2.10}$$

with valley index ν, bandgap energy $E^{\lambda s}_{\nu} = E_{gap} + \nu E^{\lambda s}_{soc}$ where E^{ν}_{gap} is the bandgap energy and $E^{\lambda s\nu}_{soc}$ the spin depending band splitting. The $+$ corresponds to the K and $-$ to the K′ point, respectively. The hopping integrals

$$t^{\lambda s\nu} = \langle\phi^{\lambda s\nu}_j(\mathbf{r}-\mathbf{R}_j)|H|\phi^{\lambda s\nu}_i(\mathbf{r}-\mathbf{R}_i)\rangle \tag{2.11}$$

which stem from the tight-binding approach determine the curvature of the corresponding band. The hopping integral will be important in Section 5.1 where we investigate the changes of this parameter due to strain. We cannot solve those integrals within our theory but we can fix their values to the effective masses (taken from DFT/experiment [41]) such that

$$\frac{3|t^{\lambda s\nu}|^2}{4\Delta E_{\nu}^{\lambda s}} = \frac{\hbar^2}{2m_{\text{eff}}^{\nu}}. \tag{2.12}$$

with effective mass m_{eff}^{ν}. Note that the effective masses are different for the valence and conduction bands in the different valleys and are taken consistently from Ref. [41]. Moreover, the spin-orbit splitting and energy differences between the valleys are taken from this reference.

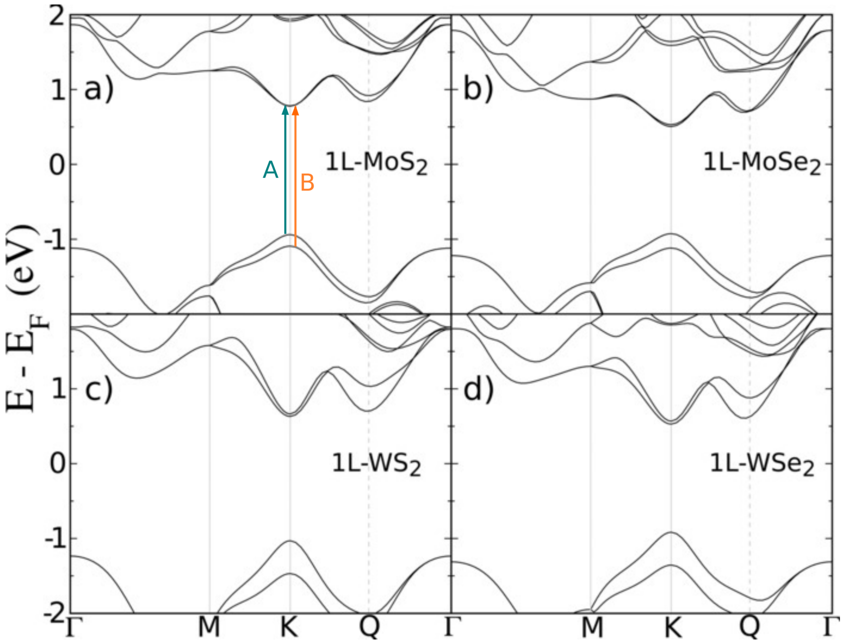

Figure 2.2: **Electronic band structure of TMDs.** The electronic band structure for the most prominent TMDs (a) MoS_2, (b) $MoSe_2$, (c) WS_2 and (d) WSe_2 showing the lowest conduction and highest valence band, including the spin-orbit splitting. Shown are the most prominent A transition (spin-up transition, turquoise) and B transition (spin-down transition, orange). Taken and adapted from Ref. [42].

Figure 2.2 shows a typical band structure from DFT where we can see the direct band gap at the K point. The spin-up transition is usually referred to as A transition in reference and the spin-down transition as B. Note that the energy difference of the two transitions is given by the spin-orbit splitting in both conduction and valence band. We can also see the other high-symmetry Λ and Γ points here which can be approximated within an effective mass approach.

2.3 TMD Bloch Equations

Once we have determined the full Hamiltonian we can now exploit Heisenberg's equation of motion $i\hbar\dot{O} = [O, H]$ where O are our microscopic quantities of interest. Depending on the problem we want to investigate, in particular interesting are:

1. Electron/photon/phonon occupation
   $f_{\mathbf{k}}^{\lambda s} = \langle a_{\mathbf{k}}^{\lambda s\dagger} a_{\mathbf{k}}^{\lambda s}\rangle \quad n_{\mathbf{q}}^{\sigma} = \langle c_{\mathbf{q}}^{\sigma\dagger} c_{\mathbf{q}}^{\sigma}\rangle \quad n_{\mathbf{q}}^{\alpha} = \langle b_{\mathbf{q}}^{\alpha\dagger} b_{\mathbf{q}}^{\alpha}\rangle$
2. Polarization $p_{\mathbf{k_1 k_2}}^{\lambda_1 s_1 \lambda_2 s_2} = \langle a_{\mathbf{k_1}}^{\lambda_1 s_1\dagger} a_{\mathbf{k_2}}^{\lambda_2 s_2}\rangle$
3. Photon-assisted polarization $S_{\mathbf{k_1 k_2 q}}^{\lambda_1 s_1 \lambda_2 s_2 \sigma} = \langle c_{\mathbf{q}}^{\sigma\dagger} a_{\mathbf{k_1}}^{\lambda_1 s_1\dagger} a_{\mathbf{k_2}}^{\lambda_2 s_2}\rangle$
4. Exciton occupation $N_{\mathbf{k_1 k_2 k_3 k_4}}^{\lambda_1 s_1 \lambda_2 s_2 \lambda_3 s_3 \lambda_4 s_4} = \langle a_{\mathbf{k_1}}^{\lambda_1 s_1\dagger} a_{\mathbf{k_2}}^{\lambda_2 s_2} a_{\mathbf{k_3}}^{\lambda_3 s_3\dagger} a_{\mathbf{k_4}}^{\lambda_4 s_4}\rangle$

Depending on the complexity of the system, we can look at different limits.

Coherent Limit

In the coherent limit, we want to get access to the absorption spectra. The absorption coefficient $\alpha(\omega)$ is proportional to the optical susceptibility $\chi(\omega)$ as the linear response to an optical perturbation induced by an external vector potential $A(\omega)$, and hence $\alpha(\omega) \propto \omega \mathrm{Im}\left[\chi(\omega)\right] \propto \mathrm{Im}\left[\frac{j(\omega)}{\omega A(\omega)}\right]$ which can be calculated with the macroscopic current density $j(\omega)$. We further quantize the field, i.e. express the current density within the second quantization [32], and use the dipole approximation, i.e. $\mathbf{A}(\mathbf{r},t) \approx \mathbf{A}(t)$. With this, we find for the absorption coefficient

$$\alpha(\omega) \propto \mathrm{Im}\left[\frac{\sum_{\mathbf{l_1 l_2}} M_{\mathbf{l_1 l_2}}^{*} p_{\mathbf{l_1 l_2}}(\omega) + c.c.}{\omega A(\omega)}\right] \tag{2.13}$$

with the Fourier transformed microscopic polarization $p_{\mathbf{l_1 l_2}}(\omega) = \langle a_{\mathbf{l_1}}^{\dagger} a_{\mathbf{l_2}}\rangle$ and the carrier-light matrix element $M_{\mathbf{l_1 l_2}} = \langle \Psi_{\mathbf{l_1}} | \mathbf{p} | \Psi_{\mathbf{l_2}}\rangle$. Here, the compound index l includes momentum $\mathbf{k_l}$, band λ_l and spin s_l.
We now have access to the absorption spectra on a microscopic level via the temporal evolution of $p_{\mathbf{ij}}$ which is obtained by the Heisenberg equation of motion $i\hbar\dot{p}_{\mathbf{ij}}(t) = [p_{\mathbf{ij}}, H]$ [32, 43].

As we consider the driving field to be small in the coherent limit, it is sufficient to take the coherent part of our quantities, i.e. we consider the photon density to be constant and the electron and exciton density changes to be negligible.

Moreover, we treat the Coulomb interaction on the Hartree-Fock level. With this, our key quantity for absorption is the microscopic polarization $p^{\lambda_1 s_1 \lambda_2 s_2}_{\mathbf{k_1 k_2}}$ which is a measure for optical transitions from states in the valence band with momentum $\mathbf{k_1}$ to the conduction band with momentum $\mathbf{k_2}$. Taking into account only spin allowed terms, i.e. $s_1 = s_2 = \uparrow$, we find for the dynamical evolution

$$
\begin{aligned}
i\hbar \frac{d}{dt} p^{v\uparrow c\uparrow}_{\mathbf{k_1 k_2}} &= \left[\epsilon^{c\uparrow}_{\mathbf{k_2}} - \epsilon^{v\uparrow}_{\mathbf{k_1}} + \sum_{\mathbf{k'}} V^{ren}_{\mathbf{k_1},\mathbf{k_2},\mathbf{k'}} - i\gamma \right] p^{v\uparrow c\uparrow}_{\mathbf{k_1 k_2}} && (2.14) \\
&- \sum_{\mathbf{k'}} V^{exc}_{\mathbf{k'},\mathbf{k_1},\mathbf{k_2}} p^{v\uparrow c\uparrow}_{\mathbf{k_1}-\mathbf{k'},\mathbf{k_2}-\mathbf{k'}} && (2.15) \\
&+ \frac{i.e._0\hbar}{m} \mathbf{M}^{\mathbf{c}\uparrow\mathbf{v}\uparrow}_{\mathbf{k_1 k_2}} \cdot \mathbf{A}(\mathbf{t}) \delta_{\mathbf{k_1 k_2}} && (2.16) \\
&+ \sum_{\mathbf{k}} D^{cc}_{\mathbf{k_2 k}} p^{v\uparrow c\uparrow}_{\mathbf{k_1 k}} - D^{vv}_{\mathbf{k k_1}} p^{v\uparrow c\uparrow}_{\mathbf{k k_2}} && (2.17)
\end{aligned}
$$

where Eq. (2.14) is the electronic dispersion and Coulomb induced renormalization due to attractive electron-hole interaction, Eq. (2.15) the excitonic contribution stemming from the repulsive part of electron-hole interaction and leading to bound electron-hole pairs, Eq. (2.16) the light-matter interaction and Eq. (2.17) the interaction via disorder (molecules, phonons,impurities). Interestingly, due to the disorder a momentum transfer between different polarizations is possible. The dephasing γ includes both exciton-phonon interaction and radiative decay.

Note that we include the electron-phonon interaction on this level only indirectly via dephasing processes, for a detailed study on linewidth and scattering processes in TMDs see [25, 34].

This coupled set of equation is now solved numerically via a Runge - Kutta method and finally gives us access to $p(t)$ which can be transformed by simple Fourier transformation to $p(\omega)$ and then, by exploiting the Elliott formula Eq. (2.13), we have access to the absorption spectra.

However, most experiments actually investigate the photoluminescence spectra of these materials. In order to theoretically calculate that, we have to go one step further and take into account the incoherent limit as well in our theory.

Incoherent Limit

If the system is excited with a stronger field, such as a laser pulse, the electron-photon interaction is not negligible and we have to treat it within second quantization, i.e. Eq. (2.3). Hence, the photon density $n^{\sigma}_{\mathbf{q}}$ is now our key quantity as it determines the steady-state photoluminescence by the rate of emitted photons via

$$\mathrm{PL}(\omega_{\mathbf{q}}) \propto \omega_{\mathbf{q}} \frac{\partial}{\partial t} \langle c^{\dagger}_{\mathbf{q}} c_{\mathbf{q}} \rangle \propto \mathrm{Im} \left[\sum_{\mathbf{k_1 k_2} \mu} M_{\mathbf{q k_1 k_2}} S^{vc_{\mu}}_{\mathbf{k_1 k_2}}(\omega_{\mathbf{q}}) \right] \tag{2.18}$$

The photon-assisted polarization $S^{vc_{\mu}}_{\mathbf{k_1 k_2}}(\omega_{\mathbf{q}})$ [44] is a measure of emitted photons with energy $\hbar\omega_{\mathbf{q}}$ due to relaxation from the state $(c_{\mu}, \mathbf{k_2})$ in the conduction band of valley μ with the electronic momentum $\mathbf{k_2}$ to the state $(v, \mathbf{k_1})$ in the valence band with the momentum $\mathbf{k_1}$. To get access to the $S^{vc_{\mu}}_{\mathbf{k_1 k_2}}(\omega_{\mathbf{q}})$ we exploit Heisenberg's equation of motion and now take into account Coulomb interaction beyond the Hartree-Fock level which gives rise to correlated quantities of the form $N^{\lambda_1 s_1 \lambda_2 s_2 \lambda_3 s_3 \lambda_4 s_4}_{\mathbf{k_1 k_2 k_3 k_4}} = \langle a^{\lambda_1 s_1 \dagger}_{\mathbf{k_1}} a^{\lambda_2 s_2}_{\mathbf{k_2}} a^{\lambda_3 s_3 \dagger}_{\mathbf{k_3}} a^{\lambda_4 s_4}_{\mathbf{k_4}} \rangle$. With this, we find

$$\begin{aligned}
i\hbar \frac{d}{dt} S^{vc_{\mu}}_{\mathbf{k_1 k_2 q}} &= \left[\epsilon^{c\uparrow}_{\mathbf{k_2}} - \epsilon^{v\uparrow}_{\mathbf{k_1}} - \hbar\omega_{\mathbf{q}} + \sum_{\mathbf{k}} V^{ren}_{\mathbf{k_1, k_2, k}} - i\gamma \right] S^{vc_{\mu}}_{\mathbf{k_1 k_2 q}} \qquad (2.19) \\
&- \sum_{\mathbf{k}} V^{exc}_{\mathbf{k, k_1, k_2}} S^{vc_{\mu}}_{\mathbf{k_1 - k, k_2 - k, q}} \qquad (2.20) \\
&+ \frac{i.e._0 \hbar}{m} \sum_{\mathbf{k}} M^{\mu}_{\mathbf{qk}} \left(p^{cv}_{\mathbf{k+q, k}} p^{vc}_{\mathbf{k_1 k_2}} + N_{\mathbf{k+q, k, k_1, k_2}} \right) \qquad (2.21) \\
&+ \sum_{\mathbf{k}} D^{cc}_{\mathbf{k_2 k}} S^{vc_{\mu}}_{\mathbf{k_1 k q}} - D^{vv}_{\mathbf{k k_1}} S^{vc_{\mu}}_{\mathbf{k k_2 q}} \qquad (2.22)
\end{aligned}$$

which looks similar to the coherent limit, i.e. Eq. (2.14)-Eq. (2.17) but has an additional terms accounting for the formation of incoherent excitons densities $N_{\mathbf{k+q, k, k_1, k_2}}$.

In fact, we see that the photon-assisted polarization is driven both by coherent excitons $\propto |p^2|$ and incoherent exciton occupations $\propto N$.

In theory, we now have all ingredients to calculate the PL by solving the set of equations numerically and plugging it into (2.18). However, since excitons play a crucial role in the optical response of TMDs [7, 15, 45] we can change from the electron-hole picture to an excitonic picture, i.e. $p^{v\uparrow c\uparrow}_{\mathbf{k_1 k_2}} \rightarrow p^{\mu}_{\mathbf{qQ}}$ (and all other quantities) by coordinate-transformation. This will enable us to get a better understanding of excitons and direct access to the excitonic optical response both for absorption and photoluminescence.

3

Excitons

Due to the strong Coulomb interaction in TMDs, excitons play a crucial role in the optical response of these materials [7, 15, 45]. Therefore it is convenient to change from the electron-hole picture to an excitonic picture. We will see that we can decouple the relative and center of mass motion of the excitons and find a simple expression for the excitonic optical response.
Moreover, TMDs show a unique band structure with direct and indirect band gaps. We will introduce here the excitonic landscape, including spin- and momentum - forbidden (dark) excitons and also impurity trapped (localized) excitons, see also Figure 1.1.

3.1 Excitonic Basis

Our goal is to project the microscopic polarization into an excitonic basis, i.e. $p^{v\uparrow c\uparrow}_{\mathbf{k_1 k_2}} \to p^{\mu}_{\mathbf{qQ}}$. For this purpose, we first transform our electron and hole coordinates $\mathbf{k_1}$,$\mathbf{k_2}$ into center of mass $\mathbf{Q}$ and relative $\mathbf{q}$ coordinates. These new quantities are defined as

$$\mathbf{Q} = \mathbf{k_2} - \mathbf{k_1} \quad \text{and} \quad \mathbf{q} = \alpha \mathbf{k_1} + \beta \mathbf{k_2} \tag{3.1}$$

with masses $\alpha^\mu = \frac{m_h^\mu}{m_h^\mu + m_e^\mu}$, $\beta^\mu = \frac{m_e^\mu}{m_h^\mu + m_e^\mu}$ where m_e^μ is the electron and m_h^μ the hole mass. Note that electron and hole can stem from different valleys and μ is an exciton index, including electron and hole valleys. For the re-transformation we find $\mathbf{k_1} = \mathbf{q} - \beta^\mu \mathbf{Q}$ and $\mathbf{k_2} = \mathbf{q} + \alpha^\mu \mathbf{Q}$ and for the dispersion one can show that $\frac{\mathbf{k_1}^2}{2m_h^\mu} + \frac{\mathbf{k_2}^2}{2m_e^\mu} = \frac{\mathbf{q}^2}{2m^\mu} + \frac{\mathbf{Q}^2}{2M^\mu}$ with reduced mass $m^\mu = \frac{1}{m_e^\mu} + \frac{1}{m_h^\mu}$ and total mass $M^\mu = m_e^\mu + m_h^\mu$. We now project the microscopic polarization into the excitonic basis which enables us to decouple relative and center of mass motion

$$p^{v\uparrow c\uparrow}_{\mathbf{k_1 k_2}} \rightarrow p^{v\uparrow c\uparrow}_{\mathbf{qQ}} = \sum_{\mu} \varphi^{\mu}_{\mathbf{q}} p^{\mu}_{\mathbf{Q}}. \tag{3.2}$$

where μ indicates the excitonic state, e.g. bright KK, dark KΛ states or other spin- and/or momentum forbidden states. The relative motion is quantized according to the Wannier equation [6, 32]

$$\frac{\hbar^2 q^2}{2m^{\mu}} \varphi^{\mu}_{\mathbf{q}} - \sum_{\mathbf{k}} V(\mathbf{k}-\mathbf{q}) \varphi^{\mu}_{\mathbf{k}} = \epsilon_{\mu} \varphi^{\mu}_{\mathbf{q}} \tag{3.3}$$

that yields the eigenenergies ϵ_{μ} and eigenfunctions $\varphi^{\mu}_{\mathbf{q}}$. Note that we are focusing here on the low excitation/low density limit where we can neglect electron and hole densities. For higher densities, these terms have to be included and more details can be found in Ref. [46].

The Coulomb potential is given by $V(\mathbf{k}) = \frac{e_0^2}{2\epsilon_0 A |\mathbf{k}| \epsilon_s(|\mathbf{k}|)}$ with the screening function $\epsilon_s(k')$ accounting for dielectric properties of the thin TMD layer and the effect of the surrounding media. The potential can be approximated by the Rytova-Keldysh potential for small momenta [47, 48]. With this, we can now write for the excitonic dispersion

$$E^{\mu}(Q) = \epsilon_{\mu} + \frac{\hbar^2 Q^2}{2M^{\mu}} \quad , \tag{3.4}$$

which enables us to put all the information of the exciton into the quantum number μ.
We find binding energies in the range of hundreds of meV and depending on the Coulomb coupling strength, and more specifically the surrounding substrate, the eigenenergies can be tuned.

Depending on the band structure of the material, the excitonic landscape differs. We will discuss this in detail in the next section.

3.2 Excitonic Energy Landscape

Due to the complex electronic band structure of TMDs, a variety of excitons can be found which depend on the spin and momentum of the involved electrons and holes.

We mainly focus on

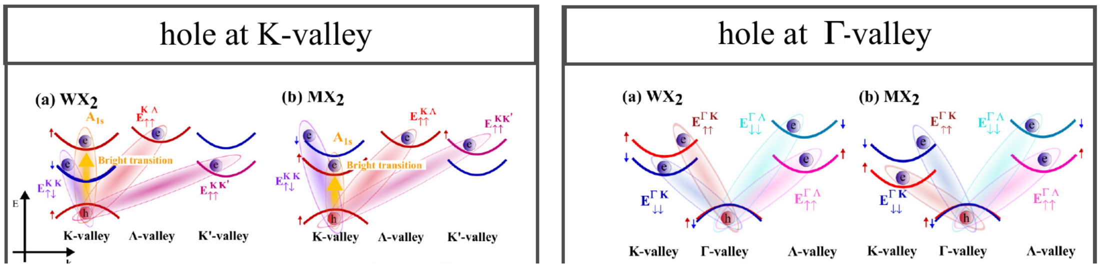

Figure 3.1: **Exciton landscape.** Illustration of spin or momentum forbidden excitons. Since we consider only one photon excitation processes, we assume the electron to be mobile and the hole to stay located either in the K-valley (left panel) or the Γ valley (right panel). Depending on the TMD material, the energetic order of dark and bright excitons varies. Figure taken from [23].

- BRIGHT EXCITONS: electron and hole with same spin and momentum, i.e. both electron and hole are located around the K-point in the Brillouin zone and we will call them $KK^{\uparrow\uparrow}$ excitons. These excitons are called bright because they can be directly accessed with light.

- DARK EXCITONS: electron and hole with different spins and/or momenta, i.e. the electron and hole are located in different valleys and/or have different spins. We take into account here the high symmetry points K, K', Λ, Γ. For example, if the hole is located at the K and the electron at the Λ point with the same spin we will call it $K\Lambda^{\uparrow\uparrow}$. These excitons are called dark since they are not directly accessible by light but need an additional momentum and/or spin to become bright. By *become bright* or *brightening* we mean become visible in optical spectra either by coupling to the excited excitons or by decaying via photon emission.

Depending on the involved valleys, each exciton has a different effective mass and hence a different binding energy and wave function, see Eq. (3.3).

The energetic landscape of excitons is discusses in detail in PAPER XI with an analysis of the variety of dark and bright excitons, see also Figure 3.1. Especially interesting are dark states which lie energetically close to the bright state or even below. Even if they are intrinsically not accessible by light, they offer scattering channels for the decay of coherent excitons and hence crucially influence the dynamics, in particular the lifetime, of the bright state which traces back to the linewidth in the optical spectra. A detailed analysis of scattering channels and linewidths of TMDs can be found in [25, 27, 34, 49, 50].

Interestingly, the energetic order of dark states is TMD specific, see Figure 3.1. We find that the nature of the exciton depends on the location of the hole (K- or Γ valley) as well as on the particular TMD. If the hole is in the K-valley, we find that for tungsten (W) based materials both spin-and momentum-dark states are energetically below the bright ones. If, however, the hole is in the Γ-valley, we find that only for MoS_2 spin-and momentum-dark states lie below the bright ones.

These different behaviors stem from the electronic structure where effective masses, spin-orbit splittings and energetic distances vary between the materials due to different composition of atomic orbitals which form the bands [51, 52]. The electronic structure values are taken from density functional theory calculations (DFT) [41] as input parameters for our theory.

Dark excitons play an indirect but crucial role in the optical response of these materials since they provide scattering channels that significantly contribute to the linewidth of the bright exciton [20, 21, 34, 53]. Their exact energies are still unclear and under debate in literature, and hence strategies to activate those dark states are needed to fully understand them. Thus a *direct* observation of the dark states in the optical spectra in form of additional peaks would be an even clearer indication of their existence and provide access to their energetic position.

On the one hand, for spin forbidden excitons, recent experiments and theory have shown their activation via a magnetic field which provides the required spin-flip [10, 20, 54]. On the other hand, for momentum forbidden excitons a mechanism is needed providing momentum to the system. Such mechanisms can be for example high-dipole molecules, disorder or phonons [18, 26, 27, 55–57] as we will discuss later.
With this, we can calculate the excitonic spectrum by exploiting the equations of motion in excitonic basis.

3.3 Excitonic Spectrum

We can now project the equation of motion, see Eq. (2.14) -Eq. (2.17), from the electron-hole picture to the exciton picture by exploiting an separation ansatz and projection into excitonic wave functions, cf. Eq. (3.2), and obtain the TMD Bloch equation in excitonic basis

$$\begin{aligned} i\hbar\frac{d}{dt}p^{\mu}_{\mathbf{Q}} &= \left[\varepsilon_{\mu} + \frac{\hbar^2 Q^2}{2M^{\mu}} - i\gamma^{\mu}\right] p^{\mu}_{\mathbf{Q}}(t) + \Omega(t)\delta_{\mathbf{Q},\mathbf{0}} \\ &+ \sum_{\nu\mathbf{k}} G^{\nu\mu}_{\mathbf{Qk}} p^{\mu}_{\mathbf{Q-k}}(t) \end{aligned} \tag{3.5}$$

where the excitonic wave functions are included in the coupling elements. Here, the Rabi frequency $\Omega(t) = \frac{ie_0\hbar}{m}\sum_{\mathbf{q}} \varphi^{\mu *}_{\mathbf{q}} \mathbf{M}^{c\uparrow v\uparrow}_{\mathbf{q}} \cdot \mathbf{A}(\mathbf{t})$ originates from the external

electromagnetic field $\mathbf{A}(\mathbf{t})$ and drives polarizations $p_{\mathbf{0}}^{\mu}$ which correspond to excitons with no center of mass momentum. Moreover, we introduced a dephasing constant γ^{μ}, describing dephasing due to phonons. This quantity determines the linewidth of the peaks in the excitonic spectra.
The coupling to a disorder is given by

$$\begin{aligned} G_{\mathbf{Qk}}^{\nu\mu} \;=\; & \sum_{\mathbf{q}} \Big[\varphi_{\mathbf{q}}^{\mu *} g_{\mathbf{q}-\alpha^{\mu}\mathbf{Q},\mathbf{q}-\alpha^{\nu}\mathbf{Q}+\mathbf{k}}^{c^{\mu}c^{\nu}} \varphi_{\mathbf{q}+\beta^{\nu}\mathbf{k}}^{\nu} - \\ & \qquad \varphi_{\mathbf{q}}^{\mu *} g_{\mathbf{q}+\beta^{\nu}\mathbf{Q}-\mathbf{k},\mathbf{q}+\beta^{\mu}\mathbf{Q}}^{v^{\mu}v^{\nu}} \varphi_{\mathbf{q}-\alpha^{\nu}\mathbf{k}}^{\nu} \Big] , \end{aligned} \tag{3.6}$$

driving the indirect polarization $p_{\mathbf{Q}}^{\mu}$ and therefore enabling a momentum transfer. Note that this is a rather general expression for the disorder coupling element. Depending on the disorder (molecules, phonons, impurities) the exact form of the matrix elements $g_{\mathbf{q},\mathbf{q}'}^{\lambda^{\mu}\lambda^{\nu}}$ changes and we will discuss this in the next chapters. These matrix elements describe scattering processes between conduction ($g_{\mathbf{q},\mathbf{q}'}^{c^{\mu}c^{\nu}}$) or valence ($g_{\mathbf{q},\mathbf{q}'}^{v^{\mu}v^{\nu}}$) bands with different momenta and/or valleys. The disorder-TMD coupling can be split into intravalley processes, i.e. $\nu = \mu$ which corresponds to momentum transfer within the same valley, and also intervalley processes, i.e. $\nu \neq \mu$ which corresponds to momentum transfer to other valleys. Depending on the wave function overlap of the corresponding valleys, those terms can become very strong.

Finally, by solving the TMD Bloch equation, Eq. (3.5), and plugging it into Eq. (2.13), we obtain the excitonic spectrum which exhibits a pronounced bright peak at the energy $\varepsilon_{\mathrm{KK}}$. If the coupling element $G_{\mathbf{Qk}}^{\nu\mu}$ is strong enough, dark excitons will brighten up and result in additional peaks in the spectra.

The next chapters will discuss the activation of dark states in detail and shed light to what extend the optical fingerprint of the material can be tuned by external characteristics.

4

Activation of Dark Excitons

In this chapter, we want to investigate different possibilities to brighten dark excitonic states. Dark states in TMDs have been literally *in the dark* for some years as they do not appear directly in the optical spectra. If they lie energetically below the bright states, they can offer additional scattering channels for excitons and hence crucially influence the dynamics of the system, reflected in decay times and linewidths of bright excitons. Moreover, if their occupation is strong enough, they can even appear in the optical spectra in form of new peaks. In the following, we will present different approaches to activate dark states. We will discuss the activation of momentum-forbidden states by high dipole molecules in 4.1 and phonons in 4.2, followed by a discussion of the activation of spin-forbidden states by external magnetic fields in 4.3.

4.1 Coupling to High-Dipole Molecules

The high sensitivity of 2D materials to their surroundings can be utilized to detect changes in the TMDs environment, such as the presence of molecules on the TMDs surface. These adsorbates can provide the required center of mass momentum to access dark states in a controlled way. While phonons could in principle be used for the activation processes as well, molecules offer the unique possibility to be externally controlled. In difference to phonons, molecules are not intrinsically in the TMD but could be added and removed and thereby give clear on/off signals of dark excitons which offers great potential for sensor applications.

In detail, we assume a non-covalent functionalization via molecules with a dipole moment, cf. Figure 4.1(a). Non-covalent means that the interaction between TMDs and molecules is based on weak interaction, not changing the electronic properties of the TMDs [58]. The molecules we investigate here are merocyanine/spiropyanine, which can be switched between a dipole moment of 13 Debye and 5.5 Debye. The choice is motivated by previous joint experiment-theory studies functionalizing carbon nanotubes and graphene with these molecules [11, 38, 59, 60]. Our studies are not limited to these molecules but can be used for any molecule with a permanent dipole moment and, to some extent, an ordered lattice. In the optimal case, the molecules build so called self-assembled monolayers (SAM) by themselves as this is their energetically most stable structure in a high packing case.

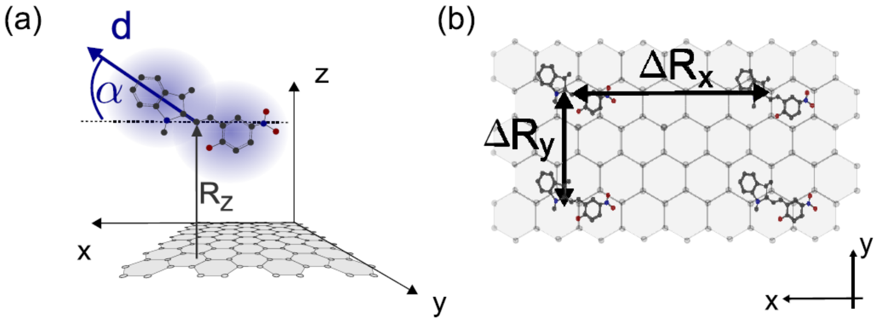

Figure 4.1: **Molecule configuration** (a) Randomly oriented molecule attached to the surface of the TMD in distance R_z ($\approx$ van der Waals radius). The molecules are characterized by a dipole vector **d** consisting of dipole moment d and orientation along z-axis α whereas the orientation within the xy plane is set to zero. (b) The molecules are ordered periodically with lattice constant ΔR_x and ΔR_y in x and y direction, respectively. Figure taken from PAPER I.

The molecules are characterized by a dipole vector $\boldsymbol{d}$ inducing interaction with excitons in the TMD material in a distance R_z. The dipole vector is represented by dipole moment d, orientation α_d with respect to xy plane of the TMD and orientation ϕ_d in xy direction, i.e. $\boldsymbol{d} = d(\cos(\phi_d)\cos(\alpha_d), \sin(\phi_d)\cos(\alpha_d), \sin(\alpha_d))$.

Interestingly, these molecules tend to self-assemble into a periodic lattice structure under certain circumstances [61]. Motivated by this, we treat the molecules periodically with the lattice constant ΔR_x in x direction and ΔR_y in y direction, see Figure 4.1(b), giving rise to a molecular density $n_{x(y)}$. As the molecules show a rectangular lattice, the density can be different in x and y direction. To be able to describe how molecules interact with 2D materials, we include a molecule-TMD interaction into our many-particle Hamiltonian.

4.1.1 Molecule-TMD Interaction

The interaction between the attached molecules and the TMD can be described in the second quantization via the carrier-molecule interaction

$$H_{c-m} = \sum_{\boldsymbol{l_1 l_2}} g_{\boldsymbol{l_1 l_2}} a^{\dagger}_{\boldsymbol{l_1}} a_{\boldsymbol{l_2}} \tag{4.1}$$

with molecule-TMD coupling (MTC) element $g_{\boldsymbol{l_1 l_2}} = \langle \psi_{l_1}(\boldsymbol{r}) | \sum_l \phi^d_l(\boldsymbol{r}) | \psi_{l_2}(\boldsymbol{r}) \rangle$ [59, 60] and compound indices $\mathbf{l}$ including momentum $\mathbf{k}$, band λ and spin s. Here, the static field induced by the molecular dipole $\mathbf{d}$ is $\phi^d_p(\boldsymbol{r}) = \frac{e_0}{4\pi\epsilon_0} \frac{\boldsymbol{d}\cdot(\boldsymbol{r}-\boldsymbol{R_p})}{|\boldsymbol{r}-\boldsymbol{R_p}|^3}$ where $\boldsymbol{R}_p$ denotes the position of molecule p with respect to the substrate [59]. Exploiting the tight-binding approach, focusing on the energetically lowest 1s transitions and allowing only interactions with the same spin, we find for the molecule- TMD coupling (MTC) element:

$$\begin{aligned} g^{\lambda_1\lambda_2}_{\boldsymbol{k_1 k_2}} = \frac{ie_0}{2\pi\epsilon_0} \sum_{NM} n_x n_y \delta_{|k_{1x}-k_{2x}|, \frac{2\pi N}{\Delta R_x}} \delta_{|k_{1y}-k_{2y}|, \frac{2\pi M}{\Delta R_y}} \times \\ \sum_j C^{\lambda_1 *}_j(\boldsymbol{k}_1) C^{\lambda_2}_j(\boldsymbol{k}_2) \delta_{\boldsymbol{k_1}-\boldsymbol{k_2},\boldsymbol{q}} \int d\boldsymbol{q} \frac{\boldsymbol{d}\cdot\boldsymbol{q}}{|\boldsymbol{q}|^2} e^{-R_z q_z} \qquad , \end{aligned} \tag{4.2}$$

including tight-binding coefficients $C^{\lambda_i}_j$ of the corresponding high-symmetry points in the Brillouin zone (K or Λ). Note that $\sum_{NM}$ includes the next, nearest next, ..., N-th molecules in x and y direction and hence N,M $\in \mathbb{N}$. The most important feature in Eq. (4.2) are the appearing Kronecker deltas: the periodic *molecular lattice* allows for well defined *momentum transfers* determined by the molecular lattice constant, e.g. $\Delta R_x(y)$. Hence the MTC element is discrete for periodic distributions. Note that, for randomly distributed molecules, MTC allows continuous momentum transfer which will be discussed later, see p. 30 and PAPER III.

We see from (4.2) that, depending on the molecular characteristics, the strength of the coupling varies. Before we discuss this in detail, we change to excitonic basis and define the exciton-TMD coupling as:

$$G^{\mu\nu}_{\mathbf{Qk}} = \sum_{\mathbf{q}} \left[\varphi^{\mu *}_{\mathbf{q}} g^{c^\mu c^\nu}_{\mathbf{q}-\alpha^\mu \mathbf{Q}, \mathbf{q}-\alpha^\nu \mathbf{Q}+\mathbf{k}} \varphi^{\nu}_{\mathbf{q}+\beta^\nu \mathbf{k}} - \varphi^{\mu *}_{\mathbf{q}} g^{v^\mu v^\nu}_{\mathbf{q}+\beta^\mu \mathbf{Q}-\mathbf{k}, \mathbf{q}+\beta^\nu \mathbf{Q}} \varphi^{\nu}_{\mathbf{q}-\alpha^\nu \mathbf{k}} \right] \tag{4.3}$$

with excitonic wave functions $\varphi^\mu_{\mathbf{q}}$ of the corresponding states.

To get a better understanding, we want to start with the coherent limit, i.e. the excitonic microscopic polarization $p^\mu_{\mathbf{Q}}$ is our key quantity, with the index μ =(KK, KΛ) denoting the bright KK and dark KΛ exciton, and hence we find for the corresponding Bloch equations:

$$\dot{p}^{\mathrm{KK}}_{\mathbf{Q}} = \Delta\varepsilon^{\mathrm{KK}}_{\mathbf{Q}} p^{\mathrm{KK}}_{\mathbf{Q}} + \Omega\,\delta_{\mathbf{Q},\mathbf{0}} + \sum_{\mu,\mathbf{k}} G^{\mathrm{KK}\mu}_{\mathbf{Qk}} p^{\mu}_{\mathbf{Q}-\mathbf{k}} \quad , \tag{4.4}$$

$$\dot{p}^{\mathrm{K\Lambda}}_{\mathbf{Q}} = \Delta\varepsilon^{\mathrm{K\Lambda}}_{\mathbf{Q}} p^{\mathrm{K\Lambda}}_{\mathbf{Q}} + \sum_{\mu,\mathbf{k}} G^{\mathrm{K\Lambda}\mu}_{\mathbf{Qk}} p^{\mu}_{\mathbf{Q}-\mathbf{k}} \quad , \tag{4.5}$$

with the abbreviation $\Delta\varepsilon^{\mu}_{\mathbf{Q}} = \frac{1}{i\hbar}(\varepsilon_{\mu} + \frac{\hbar^2 Q^2}{2M_{\mu}} - i\gamma_{\mu})$, including excitonic energy ε_{μ} and dephasing γ_{μ}. We see that the molecules enable a coupling between the two polarizations.

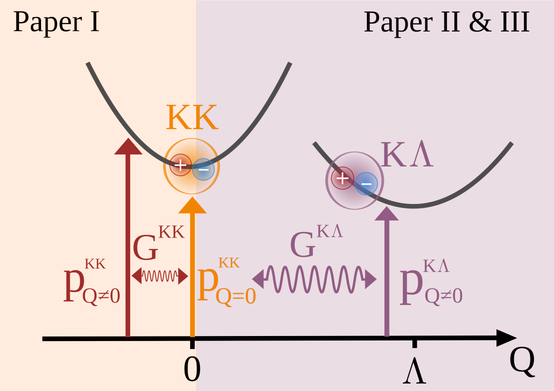

Figure 4.2: **Intravalley and Intervalley coupling.** Excitonic dispersion of K and Λ valley. The external electromagnetic field drives the excitonic resonances $p^{\mathrm{KK}}_{Q=0}$ which can couple via the molecules either with polarizations $p^{\mathrm{KK}}_{Q\neq0}$ within the same valley (orange) or with polarization $p^{\mathrm{K\Lambda}}_{Q\neq0}$ in the Λ (purple) valley, intra and intervalley coupling respectively.

This coupled set of equations is illustrated in Figure 4.2 and looks similar to a coupled oscillator system where the optically driven polarization $p^{\mathrm{KK}}_{\mathbf{Q}=\mathbf{0}}$ can now couple to $p^{\mathrm{K\Lambda}}_{\mathbf{Q}\neq\mathbf{0}}$ via the coupling element $G^{\mathrm{K\Lambda}}$.
We can differentiate intravalley and intervalley coupling processes:

1. the intravalley coupling, i.e. μ=KK, enables a coupling between polarizations in the same valley but with different center of mass momentum, see the orange and purple arrows in Figure 4.2. We find that this process is dominant for small molecular densities. As the states we can couple to are energetically higher, we expect new optical features on the higher energy side of the bright transition. → PAPER I

2. the intervalley coupling , i.e. $\mu = \mathrm{K\Lambda}$, couples polarization in different valleys, illustrated in magenta in Figure 4.2. This process dominates for large molecular densities. For some TMDs there exist energetically lower lying

valleys which result in new peaks below the bright exciton resonance.
→ PAPER II and PAPER III

Note that we focus here on intervalley processes to the Λ valley and do not include the K′ valley as it is too far away in momentum space to be reached by molecules. The possible momentum transfer is determined by the molecular density in real space which is made apparent by evaluating the Kronecker delta $\delta_{|\mathbf{k}|,\frac{2\pi m}{\Delta R}}$ appearing in the exciton-molecule coupling element. We see that for large distances between the molecules ΔR, and hence small densities, small momenta are transferred. The tighter the molecules are packed (smaller ΔR, larger n), the larger is the transferred momentum to the system. However, the molecules do have a certain size and hence the density is limited to some extent, see Figure 4.1(b). The size of the molecules is given by their geometry and can be estimated to be 1.5 nm on the long and 0.6 nm on the short axis. However, there might be additional van der Waals radii from the atoms involved in the molecule or other interactions which might enhance the occupied area of each molecule and therefore we limit our calculation to ≈ 1 molecule per nm^2 which seems realistic. To reach the Λ (K′) valley, a density of 1.1 (2.2) nm^{-2} is needed. We will focus in our study to the Λ valley as it seems more achievable in experiments. We now want to discuss the main outcomes of the intra- and intervalley coupling, or low and high-molecular density regime respectively.

Low molecular density : Intravalley processes

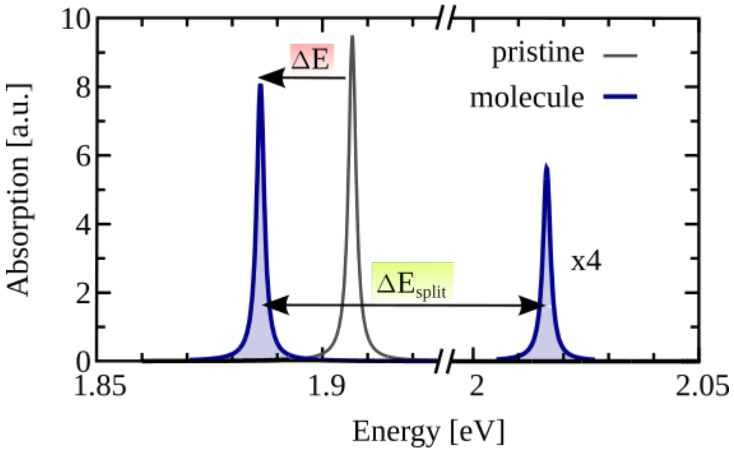

Figure 4.3: **Intravalley coupling.** Excitonic absorption spectrum of pristine (black) and functionalized (blue) MoS$_2$. In presence of the molecules, we observe a redshift of the bright peak ΔE^{red} and a new peak at the high energy side with distance ΔE from the bright resonance. Figure taken from PAPER I.

We begin with intravalley processes within the optical excited K valley. The

pristine spectrum (without molecules) shows one pronounced peak at the energy of the energetically lowest transition (1.91 eV for MoS_2), see the black line in Figure 4.3. To reach higher states within the dispersion, only a small center of mass momentum is needed which is now provided by the molecules. In their presence, the spectra shows significant changes, see the blue line in Figure 4.3. We observe an upcoming peak at higher energies corresponding to the activation of the dark states along the dispersion separated by ΔE from the bright resonance. At the same time, the bright peak shows a redshift ΔE^{red} due to back coupling from the dark to the bright state.
We can use a simple "coupled oscillator" approach to find an analytic formula for the peak position, yielding to

$$\varepsilon_{1,2} = \varepsilon_\mu + \frac{\hbar^2 Q_{xy}^2}{4M} \mp \sqrt{\left(\frac{\hbar^2 Q_{xy}^2}{4M}\right)^2 + \tilde{G}(\mathbf{Q}_{x(y)})} \tag{4.6}$$

Here, we have introduced the notation $\tilde{G}(\mathbf{Q}_{x(y)}) = G_{0,\frac{2\pi}{\Delta R_x}} G_{\frac{2\pi}{\Delta R_x},\frac{2\pi}{\Delta R_x}}$. Note that $Q_{xy} = \sqrt{Q_x^2 + Q_y^2}$ and using the Kronecker deltas from Eq. (4.2) we have defined $Q_{x(y)} = \frac{2\pi}{\Delta R_{x(y)}}$.
The solutions $\varepsilon_{1,2}$ correspond to the position of the main peak (ε_1) and the appearing side peak (ε_2) in the functionalized absorption spectra. Moreover, Eq. (4.6) reveals that the position of the resonances crucially depends on both the molecular characteristics, such as molecular coverage n, dipole moment d and dipole orientation α entering $\tilde{G}$, and on the electronic properties of the TMD entering through the total mass M.
It turns out that this formula works very well in a first approximation, for a direct comparison with the exact numerical our results in PAPER I.

We want to point out that the analytic formula gives us the opportunity to understand the optical fingerprint of our system, i.e. the redshift and the peak splitting, on a fundamental level and allows us to investigate the dependence on molecular parameters.
The redshift $E^{red} = \epsilon_1 - \epsilon_{bright}$ can be used for sensing applications as it depends on the molecular characteristics. The results are discussed in detail in PAPER I and we find as main outcomes:

1. **The strongest red shift is obtained for a molecular coverage of 0.1 nm^{-2}** which corresponds to a distance of molecules of 3 nm. This maximum can be understood by keeping in mind that the molecules transfer a center of mass momentum and hence control which excitons will couple to each other. We find for the coupling strength $G \propto n^2 \cdot e^{-2\sqrt{n}R_z}$ which explains the existence of a maximum. On the one hand, the larger momentum difference between the excitons, the smaller the overlap of the wave functions and hence the smaller the coupling, explaining the exponential tail

for higher densities. On the other hand, we find that for small densities the increase with n^2 is dominant. The exact position of the maxima (0.1 nm^{-2} for MoS_2) depends on the TMD material , which enters via the mass M in Eq. (4.6)

2. **The stronger the dipole moment the stronger the redshift**. Since we describe the interaction via a dipole interaction, this behavior is the same as for classical dipole fields which has as stronger impact the stronger the dipole induced field. For the exemplary mero/spiropyanine molecules we find a red shift of 10/5 meV respectively. However, chemists can synthesize molecules with even higher dipole moments in the lab, which might be used for functionalizing the TMDs with a stronger impact.

3. **Perpendicular orientation of the molecules shows the highest red shift**. This can be understood in analogy to classical dipole field where the impact is the strongest for this orientation as well.

Our studies show that the spectrum can be controlled easily by the configuration of the attached molecules.

So far, we have only taken into account the intravalley processes within the optically excited K valley. As we discussed earlier, TMDs exhibit other valleys in their band structure which are energetically close to the K valley but separated in momentum (indirect band gaps). In tungsten-based TMDs, momentum dark states lie energetically below the bright states which motivated us to include these states in our theory with the aim of activating them via the center of mass momentum provided by the molecules.

High molecular density : Intervalley processes

The valley we want to discuss now is the Λ valley which is located at $Q \approx 6\,\text{nm}^{-1}$. To reach this point, we assume now very densely packed molecules with inter-molecular distances of 1 nm which translates into a molecular density of 1 nm^{-2}. Interestingly, the mero/spiropyran molecules packed this dense tend to self-aligned in a very ordered structure perpendicular to the surface as was shown experimentally by Tsuboi et al [61].

So naturally we have the strong dipole moment molecules ordered in the highest-impact perpendicular directions and packed dense enough. The open question now was what happens to the overlap of the excitonic wave functions since they are located in different valleys? Hypothetically - in a perfect parabolic dispersion - being in the same valley with such a high center of mass momentum would lead to a vanishing coupling element due to vanishing overlap of wave functions and very off-resonant energetic states.

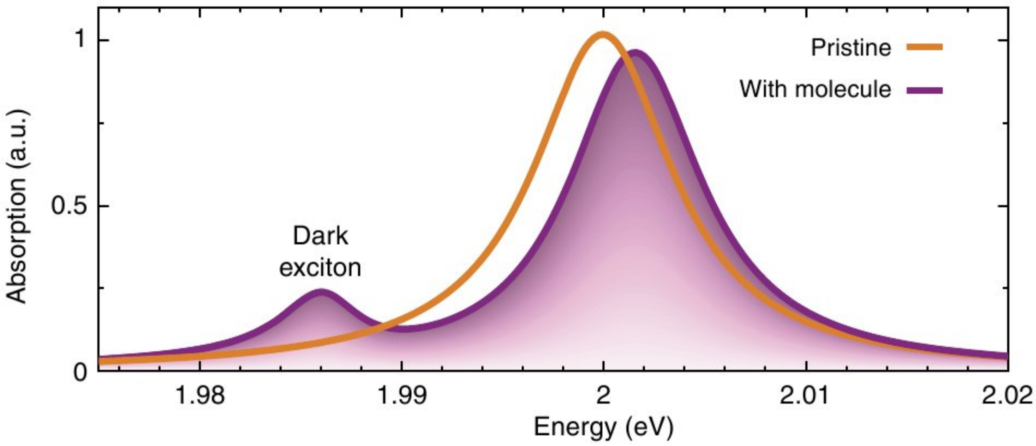

Figure 4.4: **Activation of dark excitons.** Excitonic absorption spectrum of pristine and molecule-functionalized WS_2 at 77K. Due to the efficient exciton-molecule coupling, an additional peak appears energetically below the bright exciton which can be ascribed to the dark KΛ exciton. Figure taken from PAPER II.

Since excitons in the Λ valley are much heavier due to lower curvatures of the band ($m_K^c = 0.36$ and $m_\Lambda^c = 0.64$ [41]) in tungsten-based TMDs, their wave functions are different and, more importantly, their energies lie energetically below the K valley.

Hence the Λ valley seems very promising and indeed we find that it can be reached with the molecules efficiently. The findings are discussed in detail in PAPER II. The most important outcome is that molecules can indeed activate this dark states leading to an additional peak on the *lower energy* side of the bright exciton resonance, see Figure 4.4.

This *dark peak* can be used as a clear on/off trace of the attached molecules and with this the activation of dark excitons presents a new mechanism of detecting molecules.

4.1.2 Molecule Sensing

Inspired by the activation of dark states via molecules, we started to study the sensitivity and dependency of the dark peak towards external parameters such as temperature and dielectric environment (determined by the substrate the TMD layer is deposited on).

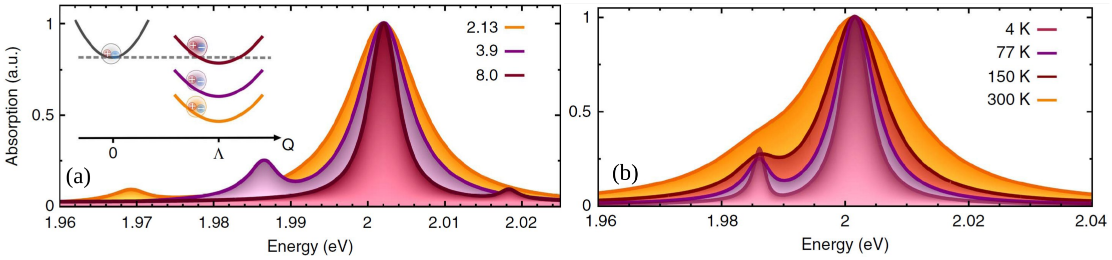

Figure 4.5: **Substrate and temperature dependence.** (a) Absorption spectra for different substrates including fused silica ($\epsilon = 2.13$), silicon dioxide ($\epsilon = 3.9$) and diamond ($\epsilon = 8.0$) at 77 K. For better comparison, the spectra are shifted to the main peak of silicon dioxide. The energetic position of the dark peak can be controlled by the choice of substrate since the substrate-induced screening has different impact on bright and dark excitons. (b) Absorption spectra for different temperatures. While at lower temperatures a clearly visible additional peak due to dark excitons can be observed in the absorption spectra, at room temperature only a shoulder can be seen due to increases exciton-phonon scattering and hence broader lines. Taken from PAPER II.

Dielectric Environment As it is challenging to work with a freestanding monolayer of TMDs, the material is mostly deposited on a substrate. Common substrate are silicon dioxide, diamond, sapphire or hBN. The dielectric constant enters the Wannier equation, cf. Eq. (3.3), via the Rytova-Keldysh potential [47, 48]. We see that the dielectric constant of the surrounding material influences the excitonic binding energy and hence the position in the spectra. Moreover, the effect on dark and bright exciton is different due to their different excitonic masses. This means that we can tune the position of the dark and bright exciton relative to each other via the substrate, see Figure 4.5(a). The purple line corresponds to our standard substrate $\epsilon = 3.9$. If the screening of the substrate is weaker (yellow line), the dark peak shifts towards lower energy and decreases in intensity, whereas for higher screening (red curve) the peak shifts towards higher energies and can even shift to the energetic higher side of the bright resonance.

We also took into account changes in the broadening of the peaks due to the changed relative positions of the excitons. As the linewidth is inversely proportional to the lifetime, it is a measure of how effective the scattering of excitons towards other valleys takes place. Therefore, when the dark exciton is shifted towards lower energies due to weak screening, scattering from the bright to the dark states becomes more efficient, the lifetime shorter and the linewidth broader. For higher screening, the dark states shifts towards higher energies, which means that the bright state looses scattering efficiency and the peak gets narrower. For details on scattering mechanisms and decay rates in TMDs see Selig et al. [25, 34] Since high-dielectric materials tend to narrow the peaks [62–64] they might be favorable for experimental setups.

Temperature Dependence The temperature behavior of the bright peak is first determined by the radiative part and then increases super-linear [34]. For the dark peak, the linewidth is narrower as it has less scattering channels then the bright one. We find a pronounced dark peak up to 150 K, see orange line in Figure 4.5(b). For room temperature (yellow curve) the dark peak is only visible as an low energy shoulder since the lines, both dark and bright, are too broad. With this, we propose the best working condition for measuring the dark peak at 77 K.

Perfect vs Realistic Conditions We have shown that by adding a layer of dipole molecules to the TMD surface we can activate both inter- and intravalley dark states. Especially the intervalley states with the Λ valley are of fundamental interest as they could be used for a novel sensing mechanism for molecules. Our calculation reveal the best conditions for sensing for:

1. dipole moments d >10 Debye
2. dipole orientation perpendicular to the TMD surface
3. high molecular density $n \approx 1$ nm^{-2} (set by the distance between K and Λ valley in k-space)
4. temperature of 150 K or below (set by phonon-induced line broadening)

As these conditions restrict the application, we were looking for ideas to achieve more realistic conditions. The studies so far investigate the optical *absorption* spectra, i.e. the coherent limit. The idea is now to go one step beyond and also take into account the incoherent limit, i.e. include exciton occupation of dark and bright states to calculate *photoluminescence* spectra as we have discussed in section 2.3.

4.1.3 Photoluminescence Spectra

Since the dark peak is energetically lower then the bright one, the idea of going to the incoherent limit and including exciton densities is that the dark state is strongly occupied by excitons. Due to its lower position in energy, we expect the dark state to be favorable for the excitons to occupy.

The efficient transfer from polarizations to populations via phonons leads to the formation of incoherent excitons on a sub-picosecond time scale [65]. The following exciton thermalization driven by emission and absorption of acoustic

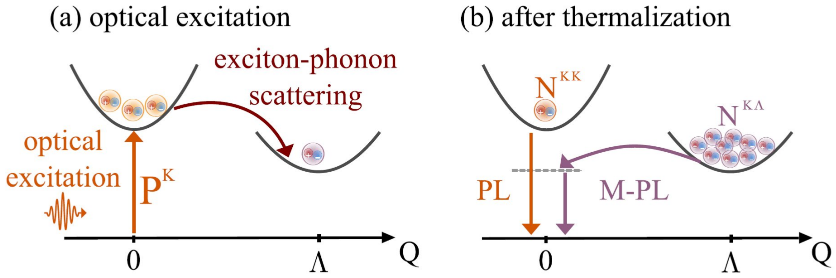

Figure 4.6: **Molecule induced photoluminescence.** (a) Optical excitation induces a microscopic polarization P^K in the K valley. Due to exciton phonon interaction the polarization can decay either within K or Λ valley. Incoherent excitons N^{KK} and $N^{\mathrm{K}\Lambda}$ are formed and thermalize until a Bose distribution is reached. (b) Whereas bright excitons N^{KK} decay radiatively by emitting a photon (PL) the dark excitons at the Λ valley require a center of mass momentum to decay back to the light cone and emit light. Molecules can provide this momentum and induce a photoluminescence signal from the dark Λ valley. Figure taken from PAPER III.

and optical phonons results in a thermalized exciton distribution. Recent studies on exciton dynamics have shown that after thermalization the lower lying Λ state is indeed the one with the highest occupation [25].

This can now be exploited by the molecules which enable a molecule-induced photoluminescence (M-PL) from the dark state, see Figure 4.6. To implement the occupation of states in our theory, in a first step we assume Bose distributed excitons with

$$N_Q^{\mu} = \left[\exp\left(\frac{E_Q^{\mu} - \mu_{\mathrm{chem}}}{k_{\mathrm{B}}T}\right) - 1\right]^{-1} \tag{4.7}$$

with $E_Q^{\mu} = \varepsilon^{\mu} + \frac{\hbar^2 Q^2}{2M^{\mu}}$, the Boltzmann constant k_{B} and the chemical potential [32] $\mu_{\mathrm{chem}} = k_{\mathrm{B}}T \ln\left[1 - \exp(-\frac{n_{\mathrm{ex}}\hbar^2 2\pi}{k_{\mathrm{B}}T3M^{\mu}})\right]$, where n_{ex} is the excitation density. Previous studies have shown that this is a good approximation in steady-state PL [34].

We find that the dark state is much more pronounced in photoluminescence then in absorption spectra, which was the main motivation for PAPER III, see also Figure 4.7. Moreover, the intensity of the dark state can be further controlled by the excitation density, the stronger it is the stronger is the signal from the dark state. For the molecule characteristics (dipole moment, orientation, density) we find the same behavior as in absorption. With this, we can exploit the TMD-Bloch equations in the incoherent limit, cf. Eq. (2.14)-Eq. (2.17), and calculate the PL response.

As the main goal of PAPER III was to get closer to realistic applications, we carried out calculation on randomized molecular distributions as well. We find that the peaks get broader but are still clearly visible. Moreover our studies

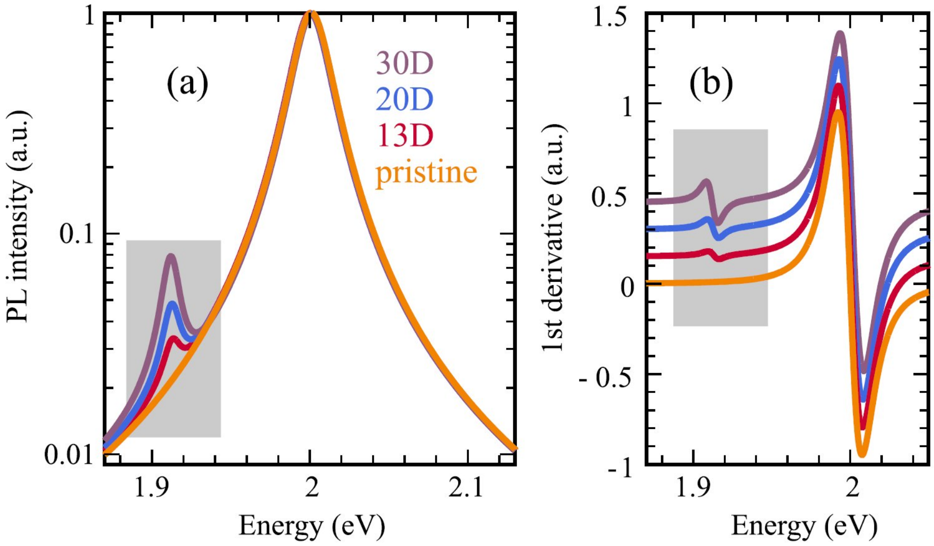

Figure 4.7: **Room-temperature conditions.** (a) Room-temperature PL in logarithmic plot and (b) first derivative of the PL in functionalized and pristine WS_2 for different dipole moments. The PL is normalized to the bright peak. We find that the visibility of the dark peak is in the range of 3-9 % compared to the bright peak. The main limiting factor is the broad excitonic linewidth at room temperature. Hence, we also show the derivative of the PL which shows clear traces of the dark exciton at room temperature even for 13 D. Note that the spectra are shifted along the y axes for better visibility. Figure taken from PAPER III.

suggest that densities in range from 0.25-1 nm^{-2} could activate the dark state. The biggest accomplishment of the photoluminescence study was, however, the much more pronounced signal of the dark peak even at higher temperatures. With this, room temperature measurement seem more realistic, as can be seen in Figure 4.7. Further optimization could be reached by achieving narrower linewidths with cleaner samples and encapsulation with hBN.

Outlook: Functionalizing Nanomaterials Inspired by their low dimensionality and sensitivity to their environment, we studied to what extent the optical response of TMDs changes when adding external molecules to the surface. The review article PAPER X summarizes approaches of functionalizing carbon nanotubes, graphene and TMDs with dipole molecules. They all show peak shifts of the main resonances due to the coupling with molecules. However, TMDs are unique in a sense of dark excitons which offer an additional peak activated by molecules.

There are still many open questions and ideas to explore in order to bring TMDs towards sensing of environmentally relevant molecules. In order to be more selective to these molecules, anchor molecules for molecules of interest could be used. Another possibility is to further investigate other molecule-TMD coupling mechanisms in combination with DFT calculations.

However, using molecules to activate dark states is a two-sided medal. On the one side, it offers a great opportunity to externally tune the TMD and the dark peak response. On the other side, however, the interaction with molecules might be more difficult to achieve in experiments. Molecules might be coupled covalently, change band structures, induce charge transfer or doping which all would lead to additional peaks/shifts in the spectra and hence makes it difficult to clearly trace back the origin of a new peak to the molecule activated dark states.

Phonons offer a unique way of investigating dark peaks without adding any extra external unknown, as they are intrinsic to TMDs. Depending on the electron-phonon coupling strengths, they might offer another possibility to activate dark states which we will discuss in the next section.

4.2 Phonon-Assisted Relaxation

The elementary electron-phonon coupling gives rise to scattering within and between the valleys, dephasing processes and thereby it determines the linewidths of peaks in the optical response. Depending on the excitonic landscape, TMDs can exhibit different valley configurations and different scattering channels, which will be reflected in the linewidth and hence it can be seen as an indirect proof of dark states [34, 65].
In addition, if the electron-phonon coupling element between the different valleys is strong enough, it can lead to higher order optical recombination processes, where an exciton decays into photon under simultaneous emission/ absorption of a phonon, and hence leads to phonon-assisted signals in the PL spectra, see Fig. 4.8(b). This processes are especially pronounced at low temperatures and for the energetically low dark states as excitons tend to occupy these after thermalization. Previous studies [57] have shown that phonon assisted low energy PL peaks of dark states appear at low temperatures, and hence phonons offer an intrinsic way of activating dark states.
Due to their unique appearance, phonon assisted peaks, also known as phonon sidebands, offer a possibility to distinguish them from other exciton/trion resonances, and especially at low temperatures it is important to include them in our theory. We follow the approach developed by Brem et al. [57] to include the phonon interaction and get access to phonon assisted PL.

4.2.1 Phonon-TMD Interaction

To include the interactions with phonons, we extend the Hamiltonian with the carrier-phonon interaction

$$H_{c-phon} = \sum_{\alpha \boldsymbol{k_1} \boldsymbol{k_2} \lambda_1 \lambda_2 s_1 s_2} g^{\alpha \lambda_1 \lambda_2 s_1 s_2}_{\boldsymbol{k_1} \boldsymbol{k_2}} a^{\lambda_1 s_1 \dagger}_{\boldsymbol{k_1}} a^{\lambda_2 s_2}_{\boldsymbol{k_2}} \left(b^{\alpha}_{\boldsymbol{k_1}-\boldsymbol{k_2}} + b^{\alpha \dagger}_{\boldsymbol{k_2}-\boldsymbol{k_1}} \right) \tag{4.8}$$

which has a very similar form to the molecule coupling from Eq. (4.1), but additionally includes phonon operators b^{α}. The phonon mode α includes both transverse and longitudinal optical and acoustic phonons (TO,LO,TA,LA). For the phonon dispersion in the free Hamiltonian, cf. Eq. (2.1), we include Γ,M, K and Λ phonons and approximate their dispersion by a zeroth/first order Taylor expansion around those high symmetry points. We follow the Debye model for acoustic modes (first order) around the Γ point and the Einstein approximation (zeroth order) for all other points and modes.
For the carrier-phonon coupling elements $g^{\alpha}_{\boldsymbol{k}}$, we use a deformation potential approximation, suggested in Ref. [66] which reads

$$g^{\alpha}_{\boldsymbol{k}} \approx \sqrt{\frac{\hbar}{2\rho A \Omega_{\alpha k}}} \begin{cases} D^{\lambda(1)}_{\alpha} \boldsymbol{k} & \text{if } \alpha = \Gamma_{TA}, \Gamma_{LA} \\ D^{\lambda(0)}_{\alpha} & \text{else} \end{cases} \tag{4.9}$$

with ρ surface mass density of the TMD and $D^{\lambda(i)}_{\alpha}$ the zeroth or first order deformation potential taken from DFT calculations [66] as well as phonon dispersions. Now we can include this part in the total Hamiltonian and find both scattering and dephasing processes. Due to scattering of the excitons within the valley and between the valley, exciton lifetimes and linewidths change, for a detailed study see Selig et al [34] and Brem et al. [65]. However, if we include the phonon interaction on a higher correlated level, we can even activate momentum dark excitons via phonons.

4.2.2 Phonon-Assisted Photoluminescence

To get access to phonon-assisted PL, we included the carrier-phonon and the free phonon Hamilton, and rewrite the equations of motions. While our key quantity so far was the photon-assisted polarization $\langle c^{\dagger} a^{\dagger} a \rangle$, now we have to also include the phonon-assisted polarization, i.e. $\langle c^{\dagger} b^{(\dagger)} a^{\dagger} a \rangle$.

So our new microscopic quantities are:

1. phonon-assisted polarization $U^{\lambda_1 s_1 \lambda_2 s_2 \sigma \alpha}_{\mathbf{k_1} \mathbf{k_2} \mathbf{q} \mathbf{k}} = \langle c^{\sigma \dagger}_{\mathbf{q}} b^{\alpha}_{\mathbf{k}} a^{\lambda_1 s_1 \dagger}_{\mathbf{k_1}} a^{\lambda_2 s_2}_{\mathbf{k_2}} \rangle$

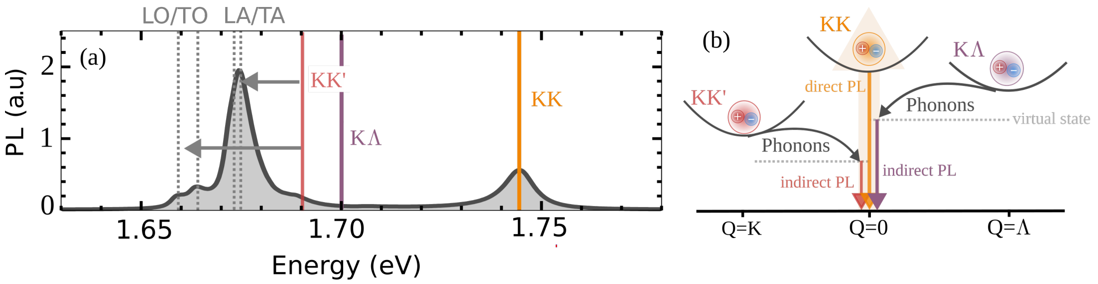

Figure 4.8: **Phonon-assisted Photoluminescence.** (a) Low temperature PL spectra of WSe$_2$ with phonon-assisted PL peaks at energies between 1.65 and 1.70 eV. We can trace back these peaks to phonon - assisted processes from the dark KK exciton (red vertical line) while the KΛ state (vertical purple line) has only small impact on the PL. (b) Illustration of the exciton dispersion, phonon scattering processes and the corresponding indirect PL.

2. exciton-phonon correlation $C^{\lambda_1 s_1 \lambda_2 s_2 \lambda_3 s_3 \lambda_4 s_4 \alpha}_{\mathbf{k_1 k_2 k_3 k_4 q}} = \langle a^{\lambda_1 s_1 \dagger}_{\mathbf{k_1}} a^{\lambda_2 s_2}_{\mathbf{k_2}} a^{\lambda_3 s_3 \dagger}_{\mathbf{k_3}} a^{\lambda_4 s_4}_{\mathbf{k_4}} b^{\alpha}_{\mathbf{q}} \rangle$

The equations of motions for these quantities can be factorized within the cluster expansion, however it is important here to include the higher order terms. For details on the derivation, see the supplementary material in [57].
Finally, we can write for the phonon-assisted photoluminescence [57] for perpendicular emission

$$I_{\mathrm{PL}}(\omega) \propto \sum_{\mu} \frac{|M^{\mu}|^2}{(\varepsilon_0^{\mu} - \omega)^2 + (\gamma_0^{\mu} + \Gamma_0^{\mu})^2} \left(\gamma_0^{\mu} N_0^{\mu} + \sum_{\nu \mathbf{Q} \alpha \pm} \frac{|D^{\mu\nu}_{\mathbf{Q}\alpha}|^2 \Gamma^{\nu}_{\mathbf{Q}} N^{\nu}_{\mathbf{Q}} \eta^{\pm}_{\alpha}}{(\varepsilon^{\nu}_{\mathbf{Q}} \pm \Omega^{\alpha}_{\mathbf{Q}} - \omega)^2 + (\Gamma^{\nu}_{\mathbf{Q}})^2} \right). \tag{4.10}$$

The first part corresponds to bright excitons μ =KK and resembles the well-known Elliott formula [67] with peak position ε_{μ} and width given by radiative (γ^{μ}) and non-radiative dephasing (Γ^{μ}) due to phonons. The oscillator strength is determined by the optical matrix element, which reads $|M^{\mu}|^2 = \sum_{\mathbf{q}} |\varphi^{\mu}_{\mathbf{q}}|^2 M_{\mathbf{q}}$ with exciton wave functions $\varphi^{\mu}_{\mathbf{q}}$, and the original momentum-dependent optical matrix element $M_{\mathbf{q}}$ [5].
The second part of (4.10) reflects the phonon-assisted activation of dark states. The position of excitonic resonances in the PL spectrum is now determined by the energy of the exciton $\varepsilon^{\nu}_{\mathbf{Q}}$ *and* the energy of the involved phonon $\pm\Omega^{\alpha}_{Q}$, see also Fig. 4.8(b). The sign corresponds to absorption (+) or emission (-) of phonons. Since dark states can not decay radiatively, the peak width is only determined by non-radiative dephasing processes Γ^{ν}. The oscillator strength of phonon-assisted peaks scales with the exciton-phonon scattering element $D^{\mu\nu}_{\mathbf{Q}\alpha} = \sum_{\mathbf{q}\lambda} \varphi^{\mu *}_{\mathbf{q}} g^{\lambda}_{\mathbf{qQ}} \varphi^{\nu}_{\mathbf{q}+\alpha_{\lambda}\mathbf{Q}}$, for more details on the phonon-coupling elements see previous work by Selig and Brem [25, 57].

Figure 4.8 shows the PL spectra of WSe$_2$ at 35 K and in (b) illustrates the phonon-induced PL from the dark KK'(red) and KΛ (purple) states. We find that beside the bright KK excitons direct PL signal at 1.743 eV, there are low energy emissions which do not correspond to the location of KK' and KΛ excitons (vertical red and purple line). The energetic position of these peaks instead corresponds to the excitonic energy ± phonon energies of TA/LA and TO/LO modes, cf. the peaks between 1.65 and 1.70 eV in the spectra.

A detailed derivation of phonon-assisted PL in our framework, discussion on different TMDs, temperature behavior and experimental results can be found in Ref. [57].

Phonons hence offer another possibility to activate dark states, however the visibility is limited to low temperatures (< 100 K). Their understanding on a microscopic footing is crucial as the low temperature PL usually shows a variety of peaks and this approach offers explanations to some of this peaks, and can thereby bring some *light into the darkness*.

4.3 External Magnetic Fields

So far, we have only discussed momentum forbidden dark excitons. However, spin-forbidden dark states lie energetically close or below the bright states in some TMDs and can be tuned externally by magnetic fields. Our goal for the next chapter is therefore to investigate the impact of an in-plane magnetic field as another *external knob* to tune the exciton landscape.

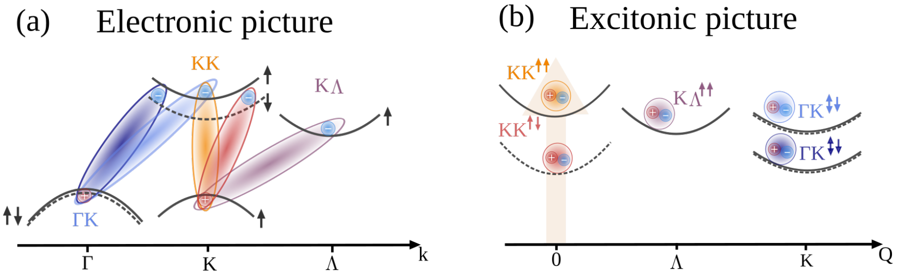

Figure 4.9: **Exciton dispersion and influence of a magnetic field.** (a) Electronic band structure around the high-symmetry K,Λ,Γ points including spin-orbit coupling (solid/dashed lines represent spin-up/down configurations). (b) Corresponding exciton picture with bright $\mathrm{KK}^{\uparrow\uparrow}$, spin-dark $\mathrm{KK}^{\uparrow\downarrow}$ and momentum-dark $\mathrm{K\Lambda}^{\uparrow\uparrow}$, $\Gamma\mathrm{K}^{\uparrow\uparrow}$ as well as spin- and momentum-dark $\Gamma\mathrm{K}^{\uparrow\downarrow}$ excitons. Note that this is a schematic figure and the exact position of the corresponding valleys depend on the TMD material. Taken from PAPER VII.

The spin–orbit coupling in TMDs gives rise to pronounced spin-splitting in both conduction and valence bands which leads to spin-allowed (same spin for valence and conduction band) and spin-dark (different spin) states. So far, we

have only looked at spin-allowed excitons, where we considered both momentum bright and dark. Now, we want to also include the spin-dark state and discuss activation of those states via external magnetic fields.
Our studies are motivated by recent experiments [20], where signatures of spin-dark excitons have been observed. For tungsten-based TMDs, a lower lying peak arises in the presence of the magnetic field which can be well understood by brightening of spin-forbidden KK$^{\uparrow\downarrow}$, see Fig. 4.9. In MoS$_2$, experiments show an uprising, lower energy band in the presence of the magnetic field which is not well understood yet. As the KK$^{\uparrow\downarrow}$ in this material lies energetically very close to the bright exciton, it can not be a possible candidate. We show that spin-and momentum forbidden ΓK excitons might be the origin of these low energy bands.
Our work sheds light on the interaction of the TMD with external magnetic fields and shows brightening mechanisms for spin-forbidden and spin-and momentum forbidden states.

4.3.1 Magnetic Field - TMD Interaction

To include a magnetic field in our approach, we have to extend the Hamilton with the carrier-magnetic field interaction

$$H_{c-magn} = \sum_{s_1,s_2,\lambda_1,\lambda_2,\boldsymbol{k}} \frac{g^\lambda}{2}\mu_B B a_{\boldsymbol{k}}^{\lambda_1 s_1 \dagger} a_{\boldsymbol{k}}^{\lambda_2 s_2} \tag{4.11}$$

with in-plane magnetic field B, Bohr magneton $\mu_B = \frac{e\hbar}{2m}$ and g factors g^λ. Since we are interested in activation of dark states, we focus on an in-plane magnetic field in one direction, i.e. $\boldsymbol{B} = (B,0,0)$. The impact of out-of-plane magnetic fields has been discussed in literature [68–70], and the main effect is the well-known Zeeman effect which leads to a splitting of the bands and hence energy shifts in the spectra. Here we want to focus on in-plane magnetic fields as they enable brightening of dark states by spin-mixing processes. Transforming the Hamiltonian into the excitonic basis, it reads $H_{\text{x-magn}} = \sum_{\mathbf{Q},i,j} G^{ij} \frac{\mu_B}{2} B X_{\mathbf{Q}}^{\dagger i} X_{\mathbf{Q}}^{j}$, with exciton operators $X_{\mathbf{Q}}^{j}$ and matrix element G^{ij}.
The matrix element $G^{ij} = \left(g_{ij}^{c} \delta_{s_i^h, s_j^h} - g_{ji}^{v} \delta_{s_i^e, s_j^e} \right) \sum_q \varphi_{\mathbf{q}}^{i} \varphi_{\mathbf{q}}^{j*}$ includes electrons (holes) keeping their spins, while mixing of spins in the valence (conduction) band of one valley takes place, i.e. $g_{ij}^{c(v)} = g_{\eta_i}^{c(v)} \delta_{\eta_i,\eta_j} (1 - \delta_{s_i^{e(h)}, s_j^{e(h)}})$.

4.3.2 Photoluminescence in Presence of a Magnetic Field

Including the carrier-magnetic field part in the Hamiltonian enables us to find the equation of motions for the photon-assisted polarization $\langle c_q^\dagger X_q^b \rangle$ which gives access to the PL. Note that we have introduced exciton operators X_q, see [71] for more details. We can further simplify by performing a unitary transformation to include the magnetic field into H_0 and subsequently apply a cluster expansion approach to account for phonon-assisted radiative recombinations, for details see PAPER VII.

For a better understanding of the influence of the magnetic field, we disregard first the impact of momentum-dark excitons and consider only the bright state $\eta = \mathrm{KK}, i = \uparrow\uparrow$ and the spin-dark state $\eta = \mathrm{KK}, i = \uparrow\downarrow$ (denoted by D). Furthermore, we consider the situation $\mu_B B \ll \Delta^\eta$, where the energy difference between spin-allowed and spin-dark states, Δ^η, is large compared to the Zeeman splitting.
With this, we can find an intuitive expression for the PL:

$$I \propto \hbar\omega \mathrm{Im}\left[\frac{\mathrm{M^2N_B}}{\epsilon_\mathrm{B} - \hbar\omega - \mathrm{i}\gamma_\mathrm{B}} + \frac{\mathrm{M}^2\left(\frac{\mathrm{g}\mu_\mathrm{B}\mathrm{B}}{2\Delta^\mathrm{KK}}\right)^2 \mathrm{N_D}}{\epsilon_\mathrm{D} - \hbar\omega - \mathrm{i}\gamma_\mathrm{D}}\right] \tag{4.12}$$

The first term describes the direct PL contribution stemming from the bright $\mathrm{KK}^{\uparrow\uparrow}$ exciton and resulting in a resonance at the energy ϵ_B. In addition, the magnetic field appearing in the second term gives rise to a new resonance at the position ϵ_D due to the activation of spin-dark excitons. Assuming that excitons quickly thermalize, exciton densities can be approximated by equilibrium Boltzmann distributions [25, 57].

We find a quadratic B-field dependence for the PL intensity ratio between the dark and the bright state - in good agreement with experimental observations [20, 72]. This reflects the prefactor $(\frac{g\mu_B B}{2\Delta})^2$ in (4.12). Here, TMD specific parameters, such as the energetic difference between the dark and bright state Δ and the g factor, play an important role and can explain differences between the TMDs.

So far, we have shown that in-plane magnetic fields can indeed activate spin-forbidden dark states which agrees very well with experiments in tungsten-based materials. Note that we focus on the energetically lowest 1s states and neglect any orbital effects a magnetic field could have. Since magnetic brightening occurs mainly at very low temperatures and therefore it is crucial to include phonons as well. Moreover, we want to investigate whether spin-and momentum forbidden ΓK excitons might be the origin of the observed peaks in $\mathrm{MoS_2}$.

4.3.3 Appearance of Spin- and Momentum-Forbidden Excitons

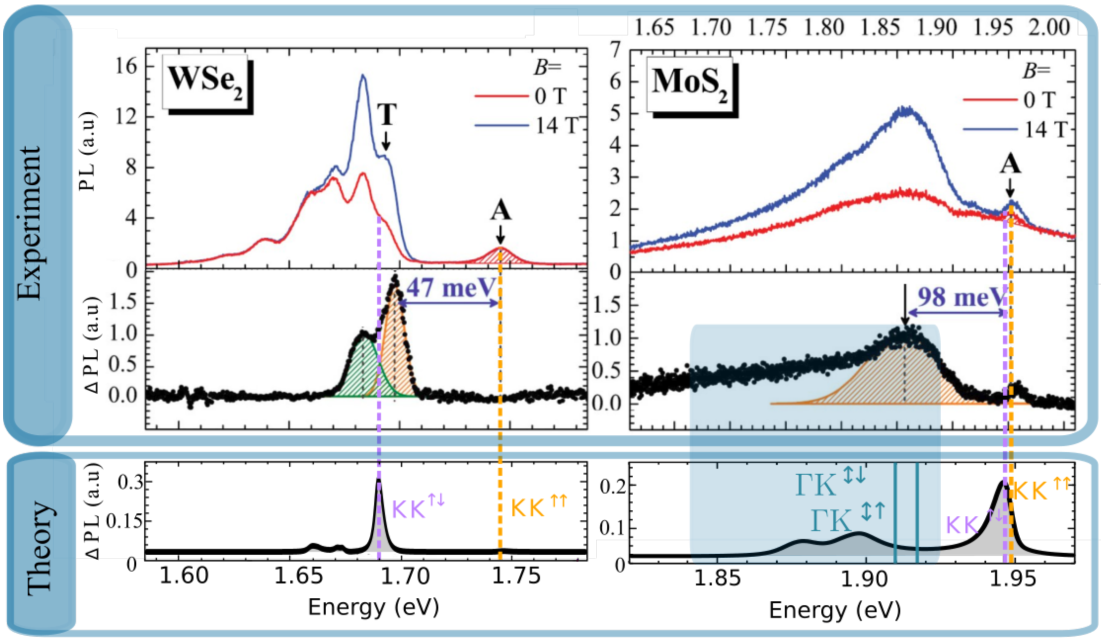

Figure 4.10: **Influence of a magnetic field on the PL spectra.** Low temperature PL spectra from experiment (upper, taken from Ref. [20]) and from our theoretical calculations (lower panel, taken from PAPER VII). For better comparison, we show the difference PL spectra ΔPL, as in the lower panel from the experiment. We find good agreement and clear differences between the two materials which can be traced back to activation of different spin-forbidden states.

We combine now our findings from section 4.2 with the magnetic field, by including both the magnetic field and phonons in the Hamiltonian. The transformation into the magnetic field basis enables us to exploit the TMD Bloch equations for phonon-assisted photoluminescence derived in Ref. [57] with the modified optical matrix element $\tilde{M}_i^\eta \to \tilde{M}^\mu$ and exciton energies $\tilde{\epsilon}_i^\eta + \frac{\hbar^2 Q^2}{2m^{\eta i}} \to \tilde{\epsilon}_{\mathbf{Q}}^\mu$ with the compound index $\mu = \eta, i$. We obtain a new expression for the photoluminescence

$$I(\omega) \propto \sum_\mu \frac{|\tilde{M}^\mu|^2}{(\tilde{\epsilon}_{\mathbf{0}}^\mu - \omega)^2 + (\gamma_{\mathbf{0}}^\mu + \Gamma_{\mathbf{0}}^\mu)^2} \left[\gamma_{\mathbf{0}}^\mu N_{\mathbf{0}}^\mu + \sum_{\nu \mathbf{Q}, \zeta \pm} \frac{|\tilde{D}_{\zeta \mathbf{Q}}^{\mu\nu}|^2 N_{\mathbf{Q}}^\nu \eta_{\zeta \mathbf{Q}}^\pm \Gamma_{\mathbf{Q}}^\nu}{(\tilde{\epsilon}_{\mathbf{Q}}^\nu \pm \Omega_{\mathbf{Q}}^\zeta - \omega)^2 + (\Gamma_{\mathbf{Q}}^\nu)^2} \right] \tag{4.13}$$

which is analogue to Eq. (4.10).

The position of the new phonon-induced signatures in the PL is determined by the energy of the exciton $\tilde{\epsilon}_{\mathbf{Q}}^\nu$ and the energy of the involved phonon $\pm\Omega_{\mathbf{Q}}^\zeta$. The exciton-phonon matrix element in the magnetic field basis reads $D_{\mathbf{Q}'}^{\eta_1 l \eta_2 j \zeta} =$

$\sum_{\mathbf{k},\lambda,n,i} U^{\eta_1}_{nl} \left(\varphi^{\eta_1 *}_{\mathbf{k}} g^{\lambda}_{\mathbf{Q}'\zeta} \varphi^{\eta_2}_{\mathbf{k}+\xi^{\lambda}\mathbf{Q}'}\right) U^{\eta_2 *}_{ij}$ with transformation matrices $U^{\eta_1(\eta_2)*}_{nl(ij)}$, see PAPER VII for the definition.

Figure 4.10 shows the PL spectra from experiments [20] in the upper panel and our theoretically calculated in the lower panel. We show the difference spectra ΔPL to get better access to the impact of the magnetic field. For WSe_2, we find a new peak at the location of the $KK^{\uparrow\downarrow}$ exciton, which is in good agreement with experiments. The peak splitting observed in the experiment might stem from exchange interaction [73] which we did not include in our study.
For MoS_2 on the other side, we find (i) a peak at the location of the $KK^{\uparrow\downarrow}$ which is energetically very close to the spin-allowed $KK^{\uparrow\uparrow}$ exciton, and (ii) broad peaks 50-100 meV the bright exciton which we can trace back to phonon-assisted PL from ΓK excitons. Note that, since they are phonon-assisted, they do not appear at the location of the ΓK excitons (vertical turquoise lines) but shifted by phonon energies. Our results can explain the experiment well and shed light on brightening mechanisms of spin-dark excitons. Moreover, we find activation of spin-momentum dark excitons in MoS_2 and offer thereby an explanation for the experimentally observed broad, low energy tails in this material.

Summary In this chapter, we have introduced several mechanisms to activate dark states: (i) while momentum forbidden excitons can be activated by molecules or phonons, (ii) spin-forbidden excitons can be activated by external magnetic fields. In the PL, new peaks arise energetically below the bright excitons. While the spectra are clear and the new peaks easy traceable in theory, in experiments it might be more difficult to clearly identify new peaks as dark excitons. The low temperature low energy range might show traces of other peaks such as trions, biexcitons, impurities, or localized excitons. Therefore, in the next chapter, we will investigate strain as a possibility to further tune the position of dark states, with the goal of unambiguously track them in PL.

5

Excitons under Strain

The previous chapter of this thesis was focused on the activation of dark states via molecules/phonons/magnetic fields as a *direct* proof of dark states in the optical spectra in form of new peaks. However, dark states leave also *indirect* signatures in the optical spectra by influencing the lifetime of the bright excitons by providing additional scattering channels.
If we could tune the relative position of dark states, the scattering processes would change leading to changes in the lifetime. Recent experiments have shown that strain can be used as such a tool, i.e. TMDs show significant changes in the linewidth and shifts of the optical resonance under strain [74]. In this part of the thesis, we try to shed light on the underlying microscopic processes when straining the TMD, i.e. we try to answer the following questions:

1. What is the origin of the shift in the optical spectra?
2. Why is the linewidth changing differently for different TMDs?
3. Do all valleys shift in the same way?

To answer these questions, we start with an analytic approach to strain deformations in the lattice structure and identify which parts excitons play in the strained case. After, we will include also DFT calculations to get access to quantitative band gap changes in the whole Brillouin zone and study the influence on the optical response in form of linewidth changes and spectral shifts.

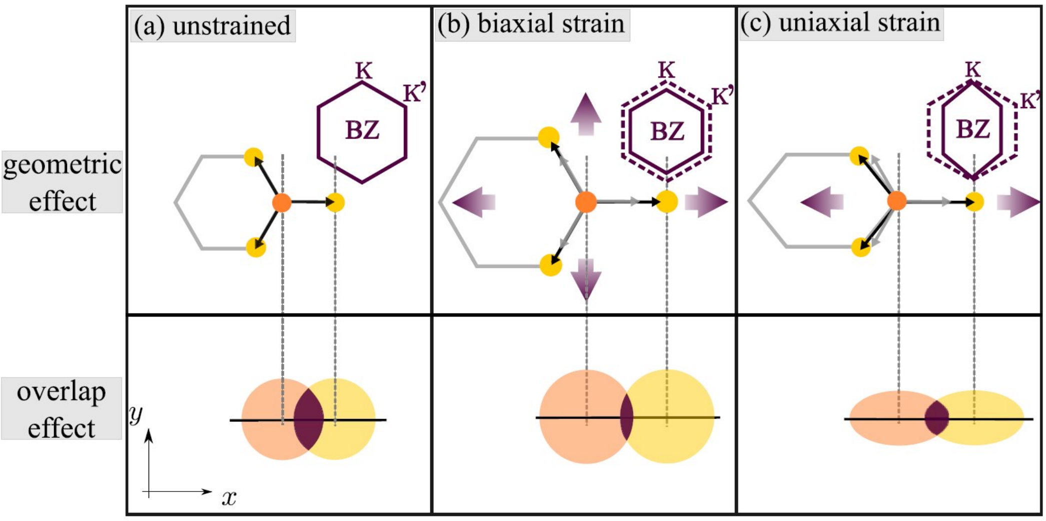

Figure 5.1: **Effects of strain.** Upper panel: geometric changes in real space lattice and lower panel: changes in the orbital functions. (a) The upper panel shows the hexagonal lattice in real space and the corresponding Brillouin zone in momentum space in the unstrained case. The lower represents corresponding orbital functions and their overlap. (b) In the presence of tensile bi-axial strain, atoms are uniformly moved apart. Hence, the hexagonal lattice structure remains symmetric. In momentum space, the BZ decreases. Due to larger distances between the atoms, the orbital overlap is reduced.(c) Tensile uni-axial strain, i.e. strain only along one direction (here x), and hence the hexagonal structure becomes anti-symmetric both in real and momentum space. Besides the reduced orbital overlap, the orbital functions become elliptic. Figure taken from PAPER IV.

5.1 Influence of Strain on Electronic and Excitonic Properties

To understand the effect of strain on the optical response, we start from an intuitive point of view: when stretching the system, the atoms will move further away from each other. This can happen either in a uniformly way (same in x and y directions), which is known as bi-axial strain, see also middle panel in Figure 5.1, or the strain can be applied only in one directions, i.e. uni-axial strain corresponding to the right panel in Figure 5.1. Besides this pure geometric effect, i.e. a change in the lattice constant

$$a_{\text{strain}} = a_0 \cdot (1 \pm \frac{\text{strain}[\%]}{100\%}) \tag{5.1}$$

where + is for tensile and - compressive strain, the orbitals of the atoms and their overlap change. This implies changes in the hopping integrals which influence the band gap and effective mass, see Eq. (2.11).

The electronic band gap $E_{\text{gap}} = \frac{1}{2}\sum_\lambda \left(H^\lambda_{ii} - H^\lambda_{jj}\right)$ is determined by the on-site energies H^{λ}_{ii}. Furthermore, the nearest-neighbor hopping integral reads $H^{\lambda}_{ij} = t^{\lambda}e(\mathbf{k}) = t^{\lambda}\sum_{\alpha} e^{-i\mathbf{k}\mathbf{b}_{\alpha}}$ with $t^{\lambda} = \langle \phi^{\lambda}_{i}(\mathbf{r}-\mathbf{R_i})|H|\phi^{\lambda}_{j}(\mathbf{r}-\mathbf{R_j})\rangle$ and the nearest-neighbor connecting vectors $\mathbf{b}_{\alpha}$. To obtain this expression, we have exploited the symmetry of the lattice and neglected the overlap of orbital functions of neighboring sites, i.e. $S_{ij} = \langle \phi^{\lambda}_{i}|\phi^{\lambda}_{j}\rangle = \delta_{ij}$. To take changes due to strain into account, we model the orbitals with hydrogen like atomic orbitals $\phi_j(r) \propto N_j \exp^{-\frac{r-SR_j}{\sigma_j}}$ with width σ_j. Since we are not interested in the exact form of the orbitals but rather the changes due to strain, this approach is a good first approximation. We allow the width to change with strain and find a self-consistent solution by benchmarking the theory to experimentally observed strain-induced shifts in optical spectra. Note that the reported shifts ΔE include both electronic (E_{gap}) and excitonic (E^{b}_{exc}) effects, and our framework can now be used to differentiate those two effects. Therefore, we have self-consistently calculated both electronic and excitonic effects, and have used the reported values above as a boundary condition for the total shift.

We find that the shift in the optical spectra is mainly determined by electronic changes, see Figure 5.2. Taking only the electronic changes into account, we see that the pristine peak (black solid line) is shifted towards lower energies (gray dashed line). If we now include the excitonic effects as well, the peak shifts a little towards higher energies (orange curve). However, the back shift of the excitons is rather small which can be explained by the small changes in the effective masses due to strain.

PAPER IV discusses in detail the changes of excitonic binding energies and wave functions due to strain. It is worth noting that we found a softening of optical selection rules in case of uni-axial strain since the symmetry is broken when straining only in one direction. The main message to take home from this paper is that the excitonic binding energies are rather stable under strain and change only by 5-10 meV per percent of strain which is, compared to the shift of 100 meV of the electronic structure, comparatively small.

So far, we only included the bright K valley for our investigations. However, having in mind the dark excitons and their importance for the lifetime, we include now the effect of strain on dark excitons.

5.2 Dark and Bright States under Strain

The approach we used so far to describe the electronic structure, namely assuming hydrogen-like orbitals, is insufficient when including the dark states. The reason for that is that K and Λ valley are formed by different orbital functions and DFT studies have revealed different behavior for different valleys when

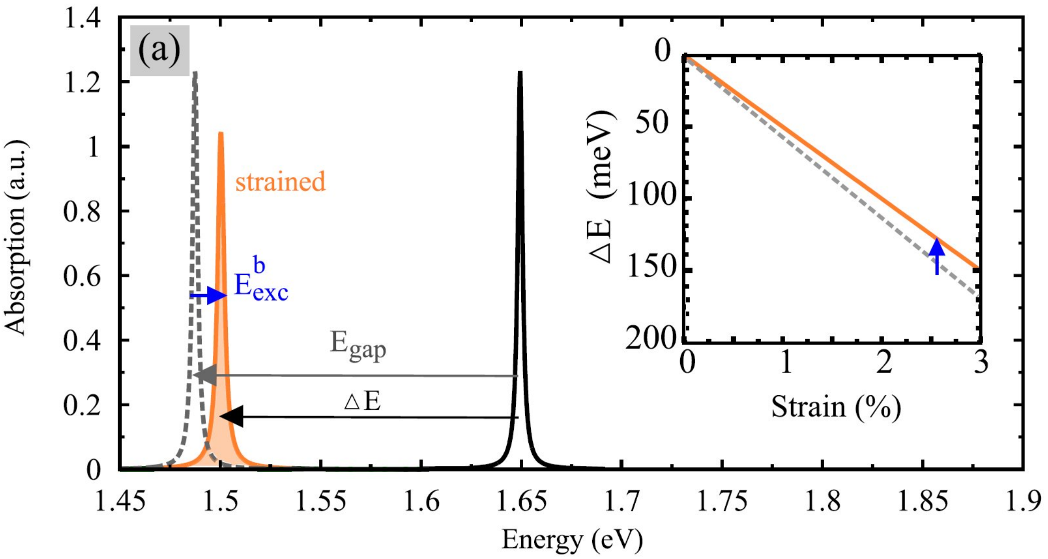

Figure 5.2: **Effects of strain on optical and electronic properties.** (a) Excitonic absorption spectra of unstrained (black) and uni-axially strained tungsten diselenide (WSe_2) as exemplary TMD material at 3 % strain. The observed red-shift stems from (i) a decrease in the orbital overlap giving rise to a reduced band gap (E_{gap}) and hence a red-shift (dashed gray line) and (ii) the geometric effect leading to a decrease in the effective masses, which results in weaker bound excitons (E^b_{exc}) and hence a blue-shift of the unstrained peak. The inset shows the resulting energy shift ΔE as a function of strain both with (orange) and without (gray dashed) taking into account excitonic effects. Figure taken from PAPER IV.

strained [52, 62]. This is why we worked with DFT to include strain in the full band structure. The results are discussed in detail in PAPER XIII, especially with regard to linewidth changes. Surprisingly, we find that the K and Λ valley shift in opposite directions when applying strain, see Figure 5.3. We find changes in the relative dark-bright separation of 150-200 meV per percent of applied strain.

This crucially influences the linewidth of the TMD due to changes in possible scattering channels. In Figure 5.3 we see that in WSe_2 the linewidth decreases by 20 meV when applying 1% of tensile strain. Since the linewidth in WSe_2 is predominantly defined by scattering to the energetically lower KΛ valley, when applying tensile strain this dark states shifts up in energy and the KK excitons loose a scattering partner, resulting in longer lifetimes and narrower lines.

The calculation are in good agreement with recent experimental data [74] which investigated the linewidth changes in different TMD materials. Depending on the relative positions of the valleys, the linewidth can increase (MoS_2), decrease (WSe_2, $MoSe_2$) or stay constant (WS_2) when applying tensile strain. The details are discussed in PAPER XIII.

The agreement with the experiment regarding both the trends and the order

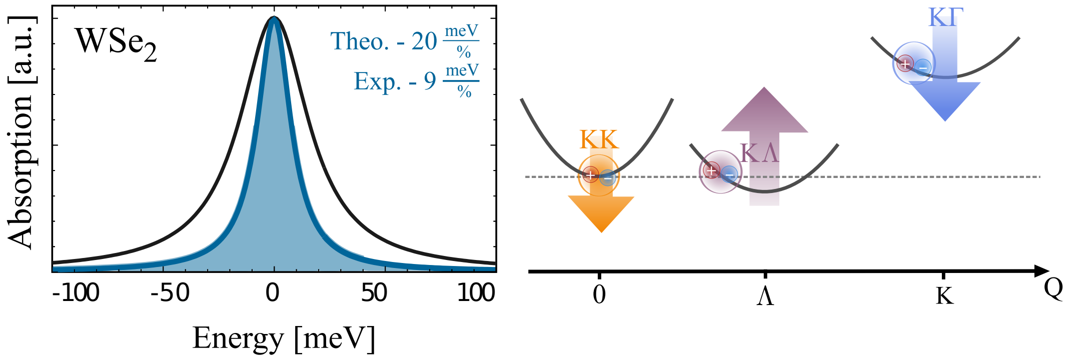

Figure 5.3: **Linewidth behavior with strain.** Excitonic absorption spectra with 1 % strain (blue) and without strain (black). The position of the peaks in the absorption spectrum is fixed to 0 meV. The values shown correspond to experimental and theoretical linewidth broadening. The broadening can be understood by looking at the excitonic dispersion, right panel. When tensile strain is applied, the dark Λ valley shifts up in energy and hence the bright exciton loses scattering channels, hence its lifetime gets longer and the lines narrower.

of magnitude seems to underline the validity of both the DFT results and our microscopic approach.

5.3 Exploiting Dark Excitons for Strain Sensing

This motivated us to combine the activation of dark states (here due to molecules, cf. Chapter 4.1 of this thesis) with strain. We calculated the optical response of WS$_2$ with an activated dark state, see gray line in Figure 5.4 . Note that the activation does not necessarily rely on molecules but can also be due to phonons or disorder or in general any mechanism providing a center of mass momentum to the system.

Once the dark peak is activated, it appears in the spectrum on the lower energy side. If we now apply strain to the system, we observe a shift and a change in intensity. The amount of strain implying this changes is only 0.05% which suggests TMDs a good candidates for strain sensing devices. Our calculation reveal a change of the dark-bright splitting by ±190 meV per percent of applied strain. Moreover, in the investigated range of small strain, our calculation reveal that the shifts are linear with strain.

PAPER V presents studies on the visibility of dark and bright peak with strain and we defined an optical gauge factor as measurement for the sensitivity of the sensor. This quantity gives the changes in the optical response, i.e. ratio between dark and bright peak, due to the mechanical deformation. We find optical gauge factors in the range of 1000 which is huge compared to reported

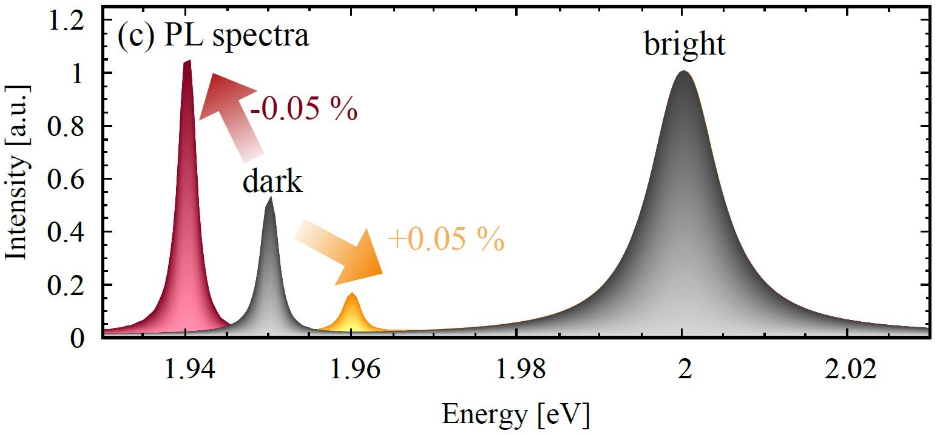

Figure 5.4: **Dark excitons for strain sensing.** PL spectra for WS_2 including bright resonance at 2.0 eV and activated dark resonance at 1.95 eV in the unstrained case (gray line). Applying 0.05 % tensile (compressive) strain leads to blue (red) shift and strong decrease (increase) in PL intensity of the dark peak. Figure taken from PAPER V.

values for TMDs in literature so far [75, 76].

Towards Real Devices

However, there are still challenges if one is aiming towards possible real-life applications. Beside a possible usage in lab setups to measure small amounts of strain due to pressure changes, TMDs might be used as parts of health monitoring devices in form of wrist bands or similar since they are transparent and very flexible [75]. In order to use the dark exciton in this devices, the TMDs might be put to a substrate which transfers only a certain amount of mechanical strain to the TMD. In this way, the response sensitivity of the TMD could be tuned with the idea to get only a clear on/off signal from the dark peak as a response to strain. Moreover, compressive strain might be challenging to achieve in experiments without buckling the TMD.

The biggest limitation for optical devices is however given by the broadening of the lines. Since TMDs are atomically thin, they are very sensitive to impurities or disorder which naturally appear within the production process. Most kinds of disorder offer additionally scattering channels and hence lead to a broadening of the lines.

6

Exciton Localization

As we have shown in this thesis so far, the TMDs sensitivity to the environment can be exploited by functionalizing them with molecules or by applying strain leading to huge changes in their optical response.
However, unintended impurities such as foreign atoms or disorder can also have a negative effect on the optical spectra, reflected in line broadening and emergence of “random” peaks in the optical spectrum. This is why typically a lot of effort is taken to make the samples as clean and perfect as possible. One common way of achieving this is to encapsulate the TMD layer by hBN which minimizes the disorder and results in very narrow lines, see Figure 6.1. Interestingly, at low temperatures (Figure 6.1(b)) there seems to appear peaks with very narrow lines and high intensity in the tungsten-based materials (blue and orange lines). Their linewidth is in the range of µeV which means that they possess an enormously long lifetime [77]. Moreover, recent experiments reported single photon emission from these states [30, 78–81].

Our goal is to understand the origin of the localized states in order to tailor the optical properties. This could be done either by chemical or physical adsorption of defect atoms, or by building a nano-structured substrate inducing trapping potentials to the TMD, in order to investigate the potential for novel nanoscale device applications, e.g. single-photon emitters and quantum opto-nanomechanics devices.

Presently, there are only speculations on the underlying many-particle mechanisms and the localized states appear more or less uncontrolled in the experimental setup. Hence, the goal of this project is to gain insights into the formation and dynamics of these localized states in order to control and tailor the optical properties.

A localized state means that the movement of the carriers is not free anymore.

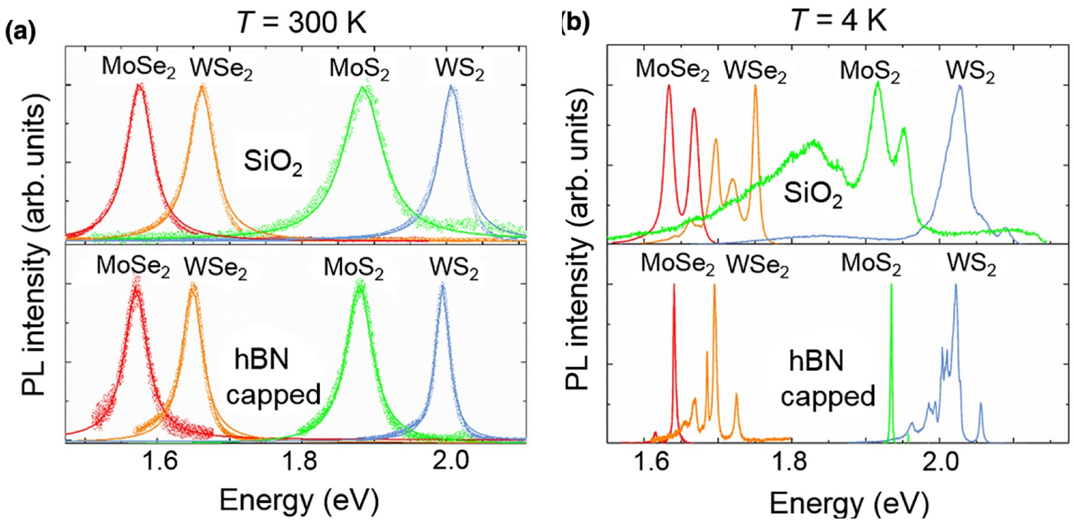

Figure 6.1: **Effect of encapsulation.** Photoluminescence spectra of different TMDs for (a) 300K and (b) 4K. Whereas at room temperature the encapsulation with hBN leads only to a line broadening in the spectra, at low temperatures encapsulation allows characterization of new, very narrow lines in the tungsten based materials described to as localized states. Figure taken from [77].

The localization of carriers can appear in different ways, Figure 6.2, where either the electron, the hole or the correlated electron-hole pair is trapped by a potential. In the electronic picture, this can be understood as additional states within the free-particle bandgap, which is also supported by different DFT studies on TMDs with defects [82–84].

The appearance of the different localized states strongly depends on the experimental setup and the induced trapping potential. Trapping can, for example appear due to local strain, due to impurities in the TMDs or at the edges of the TMD sample.

Different Approaches

In order to include localized excitons in our microscopic theory, we propose two different approaches:

1. Localization due to quantization of the center of mass movement
2. Localization due to an impurity potential, i.e. potential well

The first one is more empirical by starting in the excitonic picture and assuming

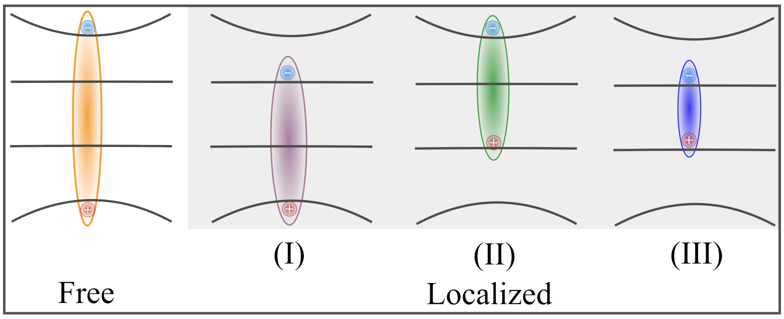

Figure 6.2: **Formation of localized states.** While free carriers show a parabolic energy dispersion, localized states are represented by mid gap states without a dispersion. The localization of carriers can appear in different ways where either (I) the electron, (II) the hole or (III) the correlated electron-hole pair is trapped by a potential.

a restriction for the center of mass momentum, whereas the second approach is more fundamental, by starting in the electron-hole picture and enabling a deeper understanding of the formation of these localized states.
Both approaches can shed light on interesting properties, while the first one gives direct access to PL and energies, the second one is useful for calculating scattering rates.
One can find impurity dependent scattering rates which enables us to calculate capture rates and dynamics. In particular, this will shed light on the formation of localized excitons which are in this picture described by a combination of free/impurity-trapped carriers. However, the second approach requires DFT input for overlapping wave functions. Therefore we decided to follow the first approach as we are mainly interested in understanding the optical response.

We will first introduce the approach of quantizing the center of mass motion in more detail which gives us access to eigenenergies and wavefunctions. With this, we can transform the photoluminescene equation to the localized exciton basis and investigate temperature and disorder-dependent PL signatures of both bright and dark localized excitons.

6.1 Quantization of Center of Mass Motion

As we discussed in chapter 3, an exciton is a correlated electron-hole pair and can be described by a center of mass momentum Q and relative momentum q. The relative momentum q can be projected in the excitonic eigenenergies and wavefunctions by solving the Wannier equation, a Schrödinger-like eigenvalue problem. Hence the movement of the free electron is now fully determined by its center of mass momentum Q, eigenfunction φ^{μ}, and its kinetic energy,

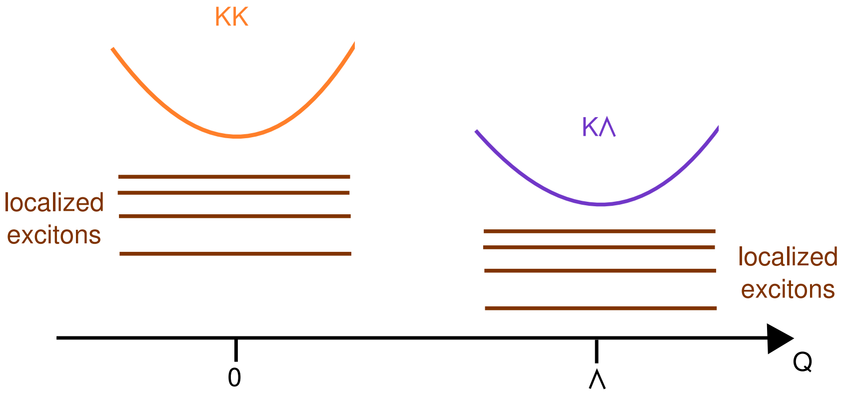

Figure 6.3: **Excitonic dispersion with localized states.** Illustration of excitonic dispersion, including free excitons with a parabolic dispersion as well as quantized localized excitons. Both KK and KΛ can be trapped, resulting in different energies of the corresponding localized states.

described simply by a parabolic Q dependency, with the curvature given by the exciton mass

$$E^{\mu}(Q) = \epsilon_{\mu} + \frac{\hbar^2 Q^2}{2M_{\mu}} \quad . \tag{6.1}$$

Here, the index μ can include both bright KK and dark KΛ and KK' excitons. Those free excitons can now be trapped by local potentials which we model using an additional trapping Hamiltonian, based on a Gaussian disorder potential. This potential leads to a quantization of the center of mass momentum [64] and we find a Schrödinger-like eigenvalue problem

$$\left(\epsilon_{\mu} + \frac{\hbar^2 Q^2}{2M_{\mu}}\right) \chi^{\mu n}_{\mathbf{Q}} - \sum_{\mathbf{Q}'} V^{\mu}_{\mathbf{Q}-\mathbf{Q}'} \chi^{\mu n}_{\mathbf{Q}'} = \varepsilon_{\mu n} \chi^{\mu x n}_{\mathbf{Q}} \tag{6.2}$$

with the Fourier transformed disorder potential

$$V^{\mu}_{\mathbf{Q}-\mathbf{Q}'} = V_0 \frac{\sigma^2}{4\ln 2} \exp\left(\frac{-(\mathbf{Q}-\mathbf{Q}')^2\, \sigma^2}{16 \ln 2}\right) \varphi^{\mu *}_{Q} \varphi^{\mu}_{Q-Q'} \quad , \tag{6.3}$$

including the form factor $\varphi^{\mu *}_{Q} \varphi^{\mu}_{Q-Q'}$ stemming from the change into free exciton basis. Note that σ corresponds to the full width of the potential in real space, which we haven chosen for better comparison to experimental results. This results in a series of localized states which lie energetically below the free excitons. Depending on the depth and width of the trapping potential, the series of localized states changes. Figure 6.4 shows binding energies and wave functions for a fixed depth, $V_0 = 40$ meV, and varying disorder width. We find that the broader the disorder potential the deeper the states and the narrower the wave functions. Note that the potential needs a certain width σ larger then the exciton radius, otherwise the potential is too narrow to trap the excitons, see the yellow curves in Fig. 6.4 which resembles free, not trapped, states.

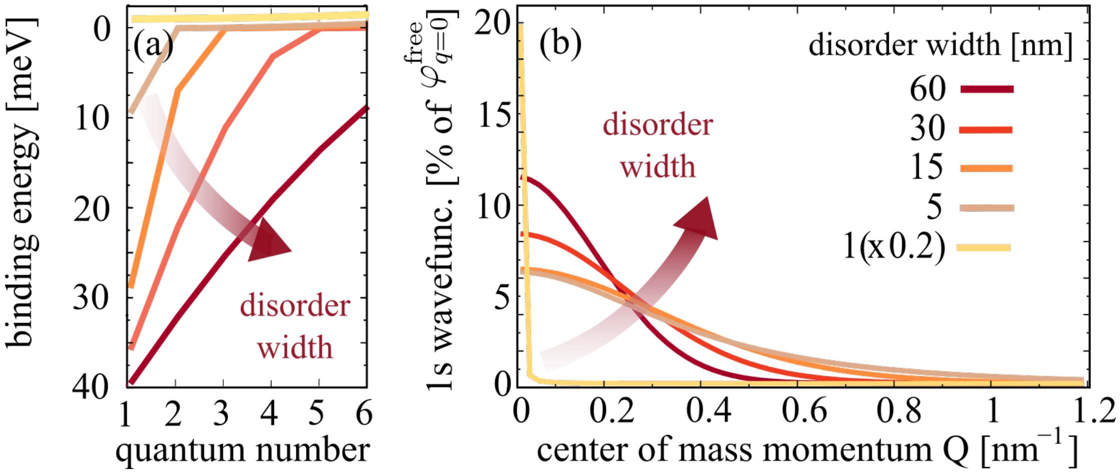

Figure 6.4: **Characteristics of localized excitons.** Disorder-width dependent (a) binding energies and (b) 1s wavefunctions of localized excitons. The broader the disorder potential, the more localized states exist and the stronger is their binding energies. Taken from Paper VI

As we now have access to both free and localized eigenenergies and wave functions, in the next step the optical response can be calculated. Moreover, this enables the calculation of exciton dynamics and relaxation, including bright, dark and localized states.

6.2 Photoluminescence of Localized Excitons

By transforming the disorder potential into momentum space, we found that it leads to a quantization of the exciton center-of-mass momentum, i.e. excitons cannot move freely anymore. Now, we project the phonon-assisted polarization into a localized excitonic basis with $S^{\mu}_{\mathbf{Q}}(t) = \sum_n \chi^{\mu n}_{\mathbf{Q}} S^{\mu n}(t)$, with $\chi^{\mu n}_{\mathbf{Q}}$ as the localized excitonic wavefunctions. Note that all types of free excitons including bright KK or momentum-dark intervalley KΛ and KK' excitons [28] can be localized in a disorder potential, each with the localization quantum number n = 1s, 2s, ... The center-of-mass localization approach leading to new states below the free excitons is consistent with the observed mid-bandgap states in the electron-hole picture in density functional theory studies on defects [82–84]. With this, we can exploit the TMD Bloch equations for phonon-assisted photoluminescence derived in the previous chapters, transfer the PL equation to the localized exciton basis and obtain the PL intensity $I^b_{\mathbf{PL}}$ for localized states belonging to the bright exciton X:

$$I^b_{\mathrm{PL}}(\omega) \propto \sum_n \frac{|M^{\mathrm{b}n}|^2 \gamma^{\mathrm{b}n} N^{\mathrm{b}n}}{(\varepsilon_{\mathrm{b}n} - \omega)^2 + (\gamma^{\mathrm{b}n} + \Gamma^{\mathrm{b}n})^2}. \tag{6.4}$$

Here, we use the index b for the bright KK excitons within the light cone and n for the quantum number of the localized state. In a similar manner, we find for the dark states: [57]:

$$I^d_{\text{PL}}(\omega) \propto \sum_{\substack{\nu n \\ \mu m \\ Q,\alpha\pm}} \Omega^{\nu n}(\omega) \frac{|D^{\nu n \mu m}_{Q\alpha}|^2 \Gamma^{\mu m} N^{\mu m} \eta^{\pm}_{\alpha}}{(\varepsilon^{\mu m} \pm \Omega^{\alpha}_{Q} - \omega)^2 + (\Gamma^{\mu m})^2}. \tag{6.5}$$

Eq. (6.4) resembles the well-known Elliott formula [67] with peak position ε_{bn} and width given by radiative (γ^{bn}) and non-radiative dephasing ($\Gamma^{b,n}$) due to phonons. The oscillator strength is determined by the optical matrix element, which reads in the new basis $|M^{\text{bn}}|^2 = |\chi^n_{Q=0}|^2 \sum_q |\varphi_q|^2 M_q$ with localized and free exciton wave functions χ and φ, respectively, as well as the original momentum dependent optical matrix element M_q [5]. The condition $Q = 0$ assures that only bright excitons within the light cone with $Q = 0$ are visible. In the limit of no localized excitons, we find $|\chi^n_{Q=0}|^2 = 1$, which results in the free-exciton photoluminescence formula [57]. Eq. (6.5) reflects the dark localized states, and we have introduced the abbreviation $\Omega^{\nu n}(\omega) = \frac{|M^{\nu n}|^2}{(\varepsilon_{\nu n}-\omega)^2+(\gamma^{\nu n}+\Gamma^{\nu n})^2}$. The position of excitonic resonances in the PL spectrum is now determined by the energy of the exciton $\varepsilon^{\mu m}$ and the energy of the involved phonon $\pm\Omega^{\alpha}_{Q}$. The sign corresponds to absorption (+) or emission (-) of phonons. Since dark states can not decay radiatively, the peak width is only determined by non-radiative dephasing processes $\Gamma^{\mu n}$. The oscillator strength of phonon-assisted peaks scales with the exciton-phonon scattering element $|D^{\nu n \mu m}_{Q\alpha}|^2 = \sum_{Q'} \chi^{\nu n *}_{Q'+Q} g^{\nu\mu}_{Q} \chi^{\mu m}_{Q'}$, where $g^{\nu\mu}_{Q}$ is the exciton-phonon coupling element including free exciton wavefunctions [25, 57].

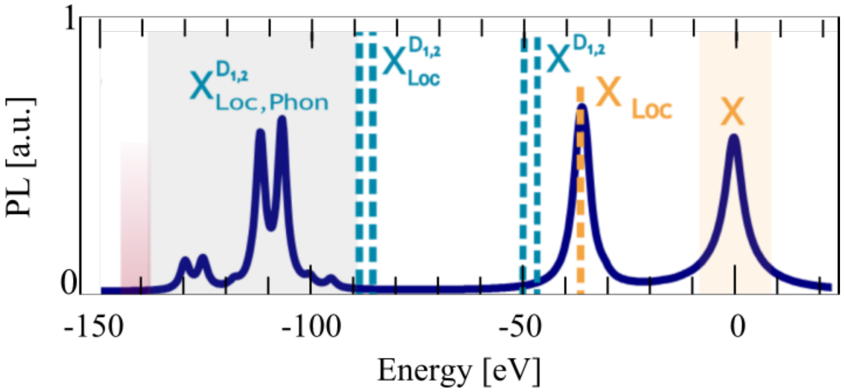

Figure 6.5: **Low temperature PL of Localized Excitons.** PL at 4K for a fixed disorder potential with $\sigma = 30$ nm and $V_0 = 40$ meV. Note that the spectra are shifted in energy so that the bright X exciton is located at 0 meV. We observe a variety of new disorder-induced peaks below the bright exciton including X_{Loc} and phonon-side bands of the momentum-dark localized excitons X^{D}_{Loc}. Taken from PAPER VI

Figure 6.5 shows the PL at 4K for a fixed disorder, and we observe a variety of peaks at low temperatures, which we can microscopically ascribe to: (i) the bright KK exciton X, (ii) the localized KK exciton X_{Loc} (located about 40 meV below the X resonance), (iii) a series of peaks around 100-130 meV below the X resonance reflecting phonon-assisted PL from dark localized states $X_{\mathrm{Loc}}^{D_{1,2}}$ ($D_{1,2} = \mathrm{K}\Lambda, \mathrm{KK}'$). In particular, we predict pronounced phonon side bands from the energetically lowest KK′ exciton involving TO/LO phonons (around 130 meV) and TA/LA phonons (around 115 meV). Our findings support the hypothesis of recent experimental findings, predicting photoluminescence resonances stemming from dark localized excitons [85, 86].

For the linewidths of the localized peaks, the radiative part is determined by the wavefunction overlap and we find $\gamma_0 \approx 0.5 - 1.0$ meV, which is in good agreement with the experimental obtained value of 0.9 meV [86].

A strength of our approach is now to use it as a *toy model* to see to what extend the spectra will change by externally accessible knobs, such as temperature and disorder dimensions. The crucial quantity here to the PL intensity of the different peaks is the exciton occupation.

The occupation $N^{\mu m}$ is determined by the capture rate of excitons into the considered disorder potential. The capture process has been treated microscopically, taking into account exciton-phonon scattering processes between free and localized excitonic states within the second-order Born-Markov approximation [87] and applying the basis of orthogonal plane waves for localized states [88, 89]. More details can be found in the supplementary material from PAPER VI.

6.3 Disorder Induced Control of Photoluminescence

Figure 6.6 illustrates the different relaxation and capture processes which will crucially influence the dynamics and hence photoluminescenes of the localized excitons and which we will investigate in the next section. The question we are trying to answer is whether free KK excitons are trapped first in the potential and get transformed into bright localized excitons? Or do they scatter first into one of the dark valleys and get trapped from there to dark localized excitons?

Depending on the timescale of phonon-relaxation within the free exciton states compared to the capture processes, the PL spectra might look very different.

We find that the capture of excitons is most likely to happen in the energetically closest localized state. Capture in energetically lower lying states appears on

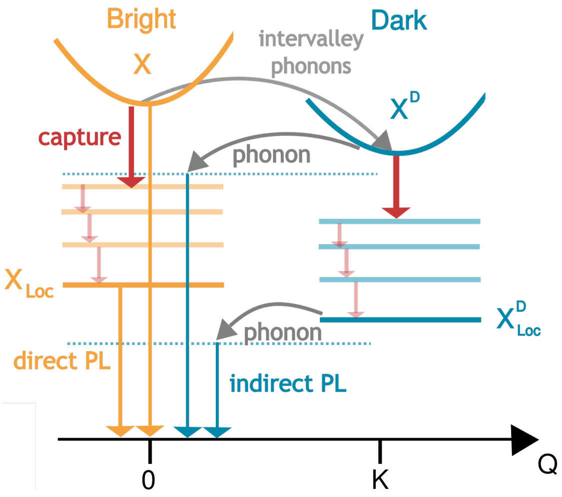

Figure 6.6: **Relaxation and capture processes.** Phonon-driven relaxation and capture processes involving both bright X and momentum-dark X^D excitons as well as their localized states X_{Loc} and X^D_{Loc}, respectively. We include phonon-assisted intervalley scattering, capture and relaxation of excitons as well as direct and phonon-assisted photoluminescence. Taken from PAPER VI

a much slower timescale and is hence negligible. Furthermore, the relaxation dynamics within the localized states happen on a much faster timescale than capture processes, i.e. excitons decay almost immediately from any ns state to the lowest 1s state. Hence, it is critical that we take into account the localized 1s states for the calculation of the optical response.

A detailed analysis of temperature and disorder control of the PL can be found in PAPER VI, here we want to give a short summary of the main findings on:

Temperature dependence. Since both capture- and intervalley processes involve phonons, we observe an interplay between those two processes. We find that below 20 K, excitons are more likely to get captured then to scatter to other valleys, while above 20 K they prefer to scatter first to other valleys and then get captured. For the PL, this means that the bright X_{Loc} peak will decrease with temperature as it becomes unlikely to be occupied. The dark localized states are more stable with temperature as they are the energetically lowest and in steady state excitons will always end up there, but they show the usual linewidth increase with temperature due to increasing phonon-scattering and hence the peaks smear out above 100 K, in agreement with experimental findings [86, 90].

Disorder dependence. As we have seen in Figure 6.4, the binding energies and wave functions of localized excitons change with disorder width. Keeping this in mind, we find that the PL peaks of both bright and dark X_{Loc} shift towards lower energies with increasing disorder width. While the dark peaks show no big changes in oscillator strength, the bright peaks increase due to more efficient capture processes. The width can hence be used to tune the appearance, position and relative intensity of bright and dark interlayer states.

Summary. In this chapter, we have developed a microscopic approach to describe trapping processes of excitons in atomically thin 2D materials. After calculating wavefunctions and energies of localized excitons, which depend on the characteristics of the disorder potential, we were able to determine the optical response. We find a variety of peaks below the bright exciton, stemming from both bright and dark localized states. The predicted signatures are strongly sensitive to temperature and disorder potential. Our findings might help to design tailored trapping potentials, for example in form of arrays, pillars, local strain potentials or local molecular potentials, to locally induce changes in the band structure and hence navigate excitons to certain areas.

7

Interlayer excitons

So far, we have investigated only monolayers of TMD and to what extend excitons can be tuned via strain, molecules, magnetic fields, phonons, or local potentials. Now, we want to extend our approach to heterostructures, in particular a TMD/molecule heterostructure to answer whether or not interlayer excitons can appear, and how we can control them.

In the last years, the vertical stacking of different two-dimensional materials to obtain novel van der Waals heterostructures with tailored properties has become a realizable achievement. Especially combining different TMDs has been very promising as their large surface-to-volume ratio makes them perfect candidates for vertical stacking with other 2D materials [91–93]. As we have discussed in Chapter II, the strong Coulomb interaction [15, 16, 94] leads to a variety of bright and dark excitons in these materials [3, 23, 95, 96]. In addition, the stacking of different kinds of TMD materials as both homo- and hetero bilayers has revealed strong interlayer coupling and signatures of interlayer excitons in the optical response [97–101]. Carriers can transfer between the two layers and form both intra- and interlayer excitons, i.e. either both carrier in the same layer or in different layers. The formation of interlayer excitons is especially interesting in these materials as they can lie energetically below the intralayer excitons due to the type II band alignment. However, the interlayer signatures in TMD/TMD systems are only visible at very low temperatures which makes it challenging to use them for technological relevant applications.

Recent experiments on TMD/organic molecule heterostructures have revealed room temperature PL from interlayer excitons, see Fig. 7.1. Motivated by these findings, the goal is to model the interaction between a monolayer of TMD and a second layer of a molecular film, forming a van der Waals heterostructure.

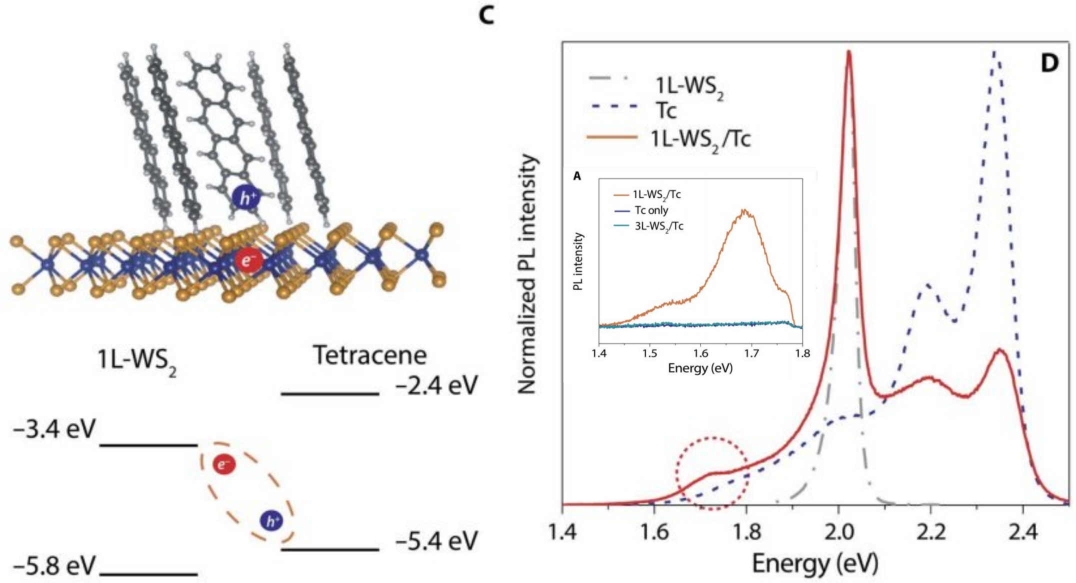

Figure 7.1: **Experimentally observed Interlayer Excitons at Room temperature** A new peak arises at around 1.7 eV due to interlayer charge transfer between TMD and molecule layers. Figure taken from Ref. [102].

7.1 Organic/Inorganic Heterostructures

To overcome the low temperature limitation of interlayer PL in conventional TMD heterostructures, organic/inorganic heterostructures could be a solution, i.e. stacking a thin layer of organic molecules on a layer of TMDs [102–104]. Especially tetra- and pentacene molecules have come into focus due to a similar band gap as the TMD materials [105] and potential for solar cells or photodetectors due to their light-emitting and harvesting properties [106–108]. Similar to TMD/TMD heterostructures, excitons play an important role: after optical excitation of an electron in the TMD layer, efficient charge transfer enables the remaining hole to tunnel from the TMD to the tetracene layer while still being attracted to the electron in the TMD. This spatially separated electron-hole pair is what we will call a *bright interlayer exciton* (also known as charge transfer or hybrid exciton in literature). If the electron further relaxes in one of the lower laying dark states within the TMD, this leads to the formation of *dark interlayer excitons*. Figure 7.2 shows the electronic and excitonic structure, respectively. For the TMD, we assume as in the previous chapters the momentum direct KK excitons and momentum indirect KΛ and KK′ excitons. We do not consider any spin-dark excitons here as we do not assume any spin transfer processes due to the molecules. For the molecule, we assume only two states, h and l, corresponding to highest occupied and lowest unoccupied states. As we showed in the previous chapters for monolayer TMD, dark excitons in monolayers can be

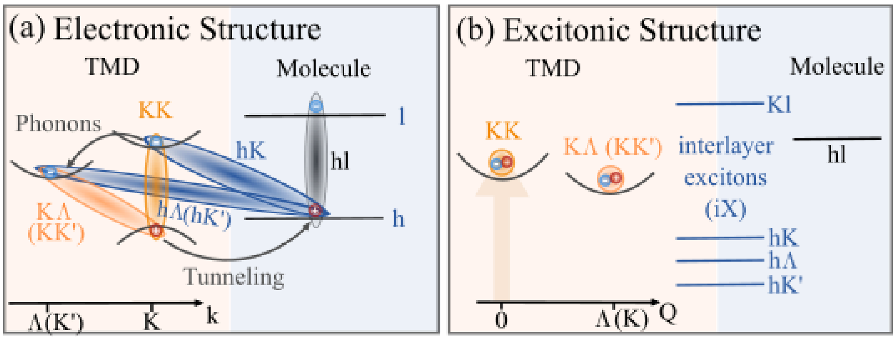

Figure 7.2: **Excitonic dispersion and appearance of interlayer excitons.** (a) Electronic dispersion of TMDs around the high symmetry K and Λ (K′) points and of molecules, consisting of HOMO (h) and LUMO (l) states. (b) Excitonic dispersion with intra- and interlayer states. We assume an optical pulse exciting bright KK excitons in the TMD layer. Figure adopted from PAPER VIII.

activated via high-dipole molecules (PAPER I - PAPER III) or phonons [57, 109–112]. However, *dark interlayer excitons* have not been discussed in literature yet and our goal is hence to describe these states on a microscopic footing.

7.2 Origin of Bright and Dark Interlayer Excitons

To describe the TMD/Tetracene (Tc) heterostructure on a microscopic level, we need to include the molecule layer into our approach. In particular, we need to include it in the free part of the Hamiltonian to calculate the energies and wave functions of the interlayer excitons. The dispersion of tetracene molecules as a thin crystalline film shows, similar to TMDs, a parabolic structure around symmetry points in both the valence and conduction band. Note that the conduction band is better known in literature as the lowest unoccupied state (LUMO) and the valence band as the highest occupied state (HOMO). The effective mass of both bands is, however, large compared to the TMDs effective mass [103, 113, 114], and we will assume the molecular states to have a quasi-flat dispersion, see Figure 7.2. We will call the conduction state l and the valence state h. Following Zhu et al. [102], we take for the energetic position of the molecule $E^l = -2.4$ eV and $E^h = -5.4$ eV. For the TMD we use $E^{c,K} = -3.4$ eV and $E^{v,K} = -5.8$ eV which results in a type II heterostructure, see also Fig. 7.2.
To calculate the excitonic binding energy, we have to solve the Wannier equation, i.e. Eq. (3.3), in the interlayer case, reading:

$$\frac{\hbar^2 q^2}{2m_\mu}\varphi^\mu_{\mathbf{q}} - \sum_{\mathbf{q}'} V^\mu_{\mathbf{q}-\mathbf{q}'}\varphi^\mu_{\mathbf{q}'} = \varepsilon_\mu \varphi^\mu_{\mathbf{q}} \quad . \tag{7.1}$$

Note that the index μ can include both intralayer μ=(KK,KΛ,KK′,hl) and interlayer states μ=(hK,hΛ,hK′,Kl) where we use the notation (hole,electron). The state hK for example corresponds to the hole located in the h state of the molecule and the electron in the K valley of the TMD, see also Figure 7.2.
We use an effective 2D Coulomb potential $V_k^{\mu} = \frac{e_0^2}{k\epsilon_0\epsilon^{\mu}(k)}$ with dielectric function $\epsilon^{\mu}(k)$, depending on the screening of the two layers, the screening of the surrounding and thickness of and between the layers [115].

Table 7.1: **Energy Landscape and screening parameters.** Electronic band gap energies E^g_μ (in eV, from [41, 102]), calculated exciton binding energies E^b_μ (meV) and spectral position E_μ (eV) for intra- and interlayer excitons. Screening parameters for dielectric environment ϵ (from [116–118]) and thickness d (in nm, from [104, 116]) and electronic masses (in m_0, from [41, 119])

			energies for state μ			
	KK	hK	hK′	hΛ	Kl	hl
E^g_μ	2.4	2.0	1.97	2.03	3.4	3.0
E^b_μ	173	150	158	173	156	450
E_μ	2.0	1.63	1.59	1.60	2.99	2.3
			screening parameters			
ϵ^{TMD}	ϵ^{Tc}	ϵ^{sur}	d^{TMD}	d^{Tc}	$d^{\text{TMD-Tc}}$	
13.61	3.69	2.45	0.61	1.1	0.3	
			electronic masses			
m^c_K	m^c_Λ	$m^c_{K'}$	m^v_K	m^h	m^l	
0.27	0.64	0.36	0.36	3.0	6.7	

The screening for the TMD ϵ^{TMD} and the tetracene ϵ^{Tc}, the thickness of the TMD d^{TMD} and tetracene d^{Tc} and the distance between TMD and tetracene $d^{\text{TMD-Tc}}$ are taken from DFT and are summarized in table 7.1.
Figure 7.3 shows the binding energies and wave functions of bright interlayer excitons for different dielectric substrates. The overall bindings energies are in a similar range then monolayer TMD and TMD/TMD hetero structures and show a similar screening behaviour [99, 115, 120], which reflects the excitonic behaviour of the organic/inorganic heterostructure. We find binding energies in the range of 150 (173, 158, 156) meV for interlayer hK (hΛ, hK′, Kl) excitons in tetracene-WS$_2$ heterostructures on a Si/SiO$_2$ substrate. The binding energies are slightly lower then the intralayer excitons in WS$_2$ ($\epsilon^{\text{KK}} = 173, \epsilon^{K\Lambda} = 206$,$\epsilon^{\text{KK}'} = 186$ meV) due to the different screening in the heterostructure. In particular, when calculating the interlayer binding energies, we observe two counteracting effects, namely the huge effective masses of the molecules leading to a reduction of energies, and on the other side a decreased screening in the molecule (ϵ^{Tc} = 3.69 vs ϵ^{TMD} = 13.6) leads to increased energies.
For the wave functions, we find also a similar behaviour as for the intralayer states, namely a narrowing in momentum space for higher dielectric constant.

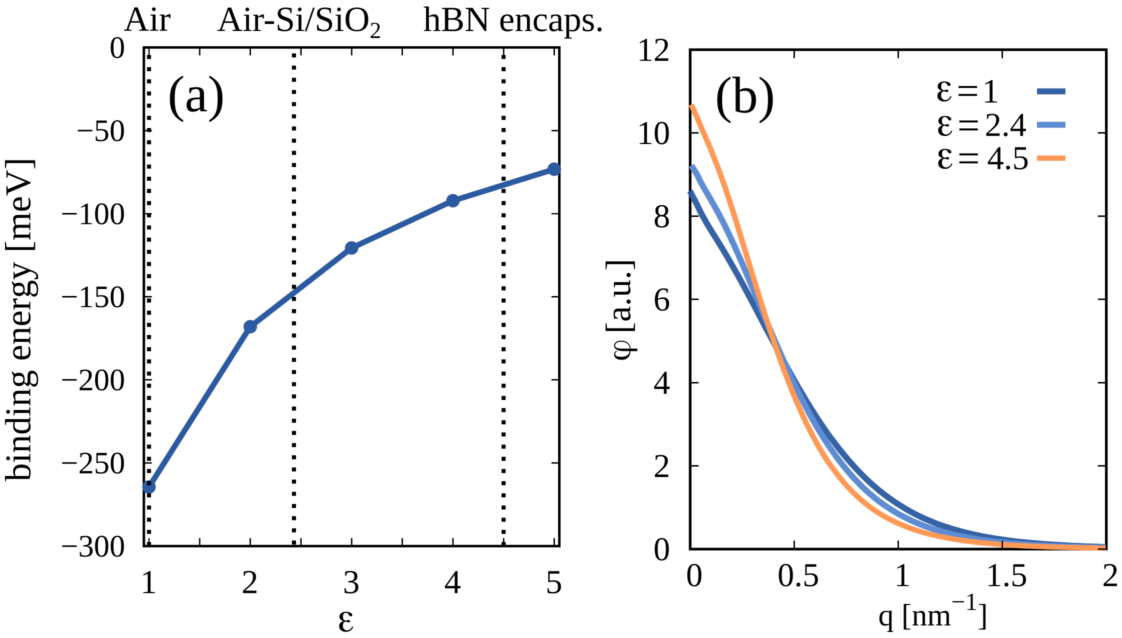

Figure 7.3: **Excitonic eigenvalues and eigenfunctions of interlayer excitons for different dielectric screening.** (a) The eigenvalues (= excitonic binding energies) of interlayer excitons show a decreasing behaviour with higher dielectric background ϵ due to stronger screening. (b) The eigenfunctions (=excitonic wave functions) become narrower in momentum space with higher screening and hence less localized in real space. Figure adopted from PAPER VIII.

In real space, this means a broadening of the wave functions and hence less localized.

Note that the energies discussed so far, i.e. ε_μ, are pure binding energies of the excitons. For their actually energetic position, we also have to take into account the band gaps, i.e. $E^c_\mu - E^v_\mu$ and hence we can write for the energetic position $E_\mu = E^c_\mu - E^v_\mu - \varepsilon_\mu$. The band gaps are taken from DFT calculations and experiments [102, 121] for a Si-SiO$_2$ substrate. We find that the interlayer hK' is the energetically lowest with $E_{\mathrm{hK}'} = 1.590$ eV, followed by $E_{\mathrm{h}\Lambda} = 1.603$ eV and $E_{\mathrm{hK}} = 1.631$ eV while the bright intralayer exciton is located around 2.0 eV for a Si-SiO$_2$ substrate, see table 7.1. Note that we have shifted the spectra to match the bright KK exciton resonance from experiment [102].
The interlayer KL exciton is located 0.9 eV above the bright KK exciton and hence we will neglect it from now on as it will not have any influence on the PL, cf. Figure 7.2 (a,b). Moreover, we will neglect the intralayer molecule state hl (located around 2.3 eV) as we will focus on optical excitation of the TMD and hence this state will not be optically active.

Note that we do not include the effect of screening on the band gap and hence can not make any predictions for the PL behaviour with different screenings. While previous studies have shown that the band gap in TMDs decreases with higher screening, little is known about screening dependent HOMO/LUMO gaps in the molecular layer. Moreover, the molecular structure might change depending on the substrate. Therefore, we would need further DFT input to predict the screening dependent gaps. We will consider a fixed substrate of Si-SiO$_2$ as is widely used in experiments. Now, we want to understand the impact of interlayer excitons on the optical response and therefore we need to find the PL equations for the interlayer system.

7.3 Photoluminescence of Heterostructures

As discussed in section 2.3 , the optical response is determined by the number of emitted photons $\mathrm{PL}(\omega_q) \propto \frac{\partial}{\partial t} n_q \propto S^{\mu}_{\mathbf{Q}}$ with the phonon assisted polarization $S^{\mu}_{\mathbf{Q}}$ as the key quantity.
The Hamiltonian of the system is similar as the monolayer case, see sec.2.1, but with an additional part $H_{\text{x-tunn}}$ which describes the tunneling of carriers between the layers. We will use this tunneling approach to account for charge transfer between the layers. It reads

$$H_{\text{tunn}} = \sum_{\mathbf{Q}\mathbf{Q}',ij} T^{ij}_{\mathbf{Q}\mathbf{Q}'} X^{\dagger i}_{\mathbf{Q}} X^{j}_{\mathbf{Q}-\mathbf{Q}'} \text{ with } T^{ij}_{\mathbf{Q}\mathbf{Q}'} = \sum_{q} \varphi^{i}_{\mathbf{q}+\alpha\mathbf{Q}} t^{ij}_{\mathbf{Q}\mathbf{Q}'} \varphi^{j}_{\mathbf{q}-\beta\mathbf{Q}'} \tag{7.2}$$

as the excitonic tunneling matrix element $T^{ij}_{\mathbf{Q}\mathbf{Q}'}$. The appearing tunneling matrix element is given by the overlap of Bloch waves Ψ_i with a tunneling potential V_{tun}, i.e. $t^{ij} = \langle \Psi_i | V_{\text{tun}} | \Psi_j \rangle$. Similar to Ovesen et al. [115], we can separate the potential into an in-plane disorder part and out-of-plane part, which is only non-zero between the layers. With this, we can write $t^{ij} = V_{in}(|k_j - k_i|) V_{out} \langle u^i | u^j \rangle_{uc}$ with u^i the lattice periodic parts of the Bloch waves integrated over a unit cell. This integral determines the tunneling strength, and we fix it to 0.01 eV in this work, assuming a similar strength as in DFT calculations on TMD/TMD heterostructures [115]. The remaining in-plane disorder potential can be described as $V_{in}(|k_j - k_i|) = \sqrt{\pi} L_c (1 + \frac{|k_j - k_i|^2 L_c^2}{2})^{-\frac{3}{4}}$ via a disorder potential with correlation length L_c in the order of the exciton Bohr radius [115].
Our theory describes both electron and hole tunneling. Since hole tunneling is more efficient in these materials [102, 104], and the expected electron tunneling interlayer exciton is off-resonant, we will neglect electron tunneling from now on. Moreover, we will neglect any twist-angle dependency [120, 122–124] since we do not expect a big impact due to the lattice mismatch between the TMD and tetracene.

In a last step, we project into a new basis where the tunneling part of the Hamiltonian is included in an effective single-particle Hamiltonian, i.e. $H_0 + H_{\text{x-tun}} = \sum_{\mathbf{Q},i} \epsilon^{i}_{\mathbf{Q}} X^{\dagger i}_{\mathbf{Q}} X^{i}_{\mathbf{Q}} + \sum_{\mathbf{Q}\mathbf{Q}',ij} T^{ij}_{\mathbf{Q}\mathbf{Q}'} X^{\dagger i}_{\mathbf{Q}} X^{j}_{\mathbf{Q}-\mathbf{Q}'} = \sum_{\mu\mathbf{Q}} \mathcal{E}_{\mu\mathbf{Q}} \tilde{X}^{\dagger}_{\mu\mathbf{Q}} \tilde{X}_{\mu\mathbf{Q}}$. Note that for the applied transformation $\hat{U}_\mu$, we exploited $\tilde{X}^\dagger_{\mu\mathbf{Q}} = \hat{U}_\mu X^{i\dagger}_{\mu\mathbf{Q}} = \sum_j U^j_{\mu\mathbf{Q}} X^{j\dagger}_{\mathbf{Q}}$ and $\hat{U}^\dagger_\mu \hat{U}_\mu = \mathcal{I}$, i.e. a uniform transformation. As intra- and interlayer states are off-resonant and we do not include hybridization effects, eigen energies are not affected by this transformation. Now, we exploit the equation of motion for the photon-assisted polarization to obtain the PL intensity I^b_{PL} for intra- and interlayer excitons resulting in the previously discussed Elliott formula (Eq. (4.10)), [57]

$$I_{\mathrm{PL}}(\omega) \propto \sum_{\mu=\,\mathrm{KK,hK}} \frac{|M_\mu|^2 \gamma_\mu N_\mu}{(E_\mu - \omega)^2 + (\gamma_\mu + \Gamma_\mu)^2}, \tag{7.3}$$

where the position of the resonances is given by the energy E_μ, the resonance width by the radiative (γ_μ) and the non-radiative phonon-assisted (Γ_μ) dephasing, and finally the oscillator strength by the exciton-photon matrix element $M_\mu = \delta_{Q,0} \sum_{\mathbf{q}} \varphi^\mu_{\mathbf{q}} M^\mu_{\mathbf{q}} \hat{U}_\mu$. The latter is determined by the exciton wave function $\varphi^\mu_{\mathbf{q}}$, the momentum-dependent optical matrix element [5] $M^\mu_{\mathbf{q}}$ and the transformation matrix $\hat{U}_\mu$ which includes the tunneling. The Kronecker delta assures that only bright excitons within the light cone with $Q = 0$ are optically active [57]. Finally, for the occupation N^μ we assume Boltzmann like exciton distributions both for intra- and interlayer states which has been shown to be good approximation in the limit of steady state PL [25, 57].

As we have discussed in the previous chapters, dark states are important in TMDs as they can lie energetically below the bright ones. We will include them here via phonon-scattering, and hence the bright PL formula is extended by phonon-assisted PL [57]

$$I^d_{\mathrm{PL}}(\omega) \propto \sum_{\substack{\nu\mu \\ \mathbf{Q},\alpha\pm}} \frac{\Theta^\nu(\omega) |D^{\nu\mu}_{\mathbf{Q}\alpha}|^2 \Gamma^\mu N^\mu \eta^\pm_\alpha}{(E_\mu \pm \Omega^\alpha_{\mathbf{Q}} - \omega)^2 + (\Gamma^\mu)^2} \tag{7.4}$$

such that the full PL signal reads $I_{\mathrm{PL}} = I^b_{\mathrm{PL}} + I^d_{\mathrm{PL}}$ which includes now all phonon-assisted intra- and interlayer states. Here, we have introduced the notation $\Theta^\nu(\omega) = \frac{|M^\nu|^2}{(E_\nu - \omega)^2 + (\gamma^\nu + \Gamma^\nu)^2}$ and we assume only phonon interactions within the TMD layer and not within the molecular layer.

Similar to Eq. (4.10), the position of the excitonic resonances in the PL spectrum is determined by the energy of the exciton E_μ and additionally the energy of the involved phonon $\pm\Omega^\alpha_{\mathbf{Q}}$ with mode α. We will focus on processes involving the bright KK excitons as initial states, stemming from optical excitation of the bright band gap in the TMD.

With this, we now have all ingredients to investigate the optical signatures of the bright intra - and interlayer peaks in the WS$_2$/tetracene heterostructure. We will now discuss the PL spectra from Fig. 7.4(a) for different regimes:

(i) **Intralayer regime.** At temperatures around room temperature, the PL spectra is dominated by the bright intralayer exciton (around 0 eV, spec-

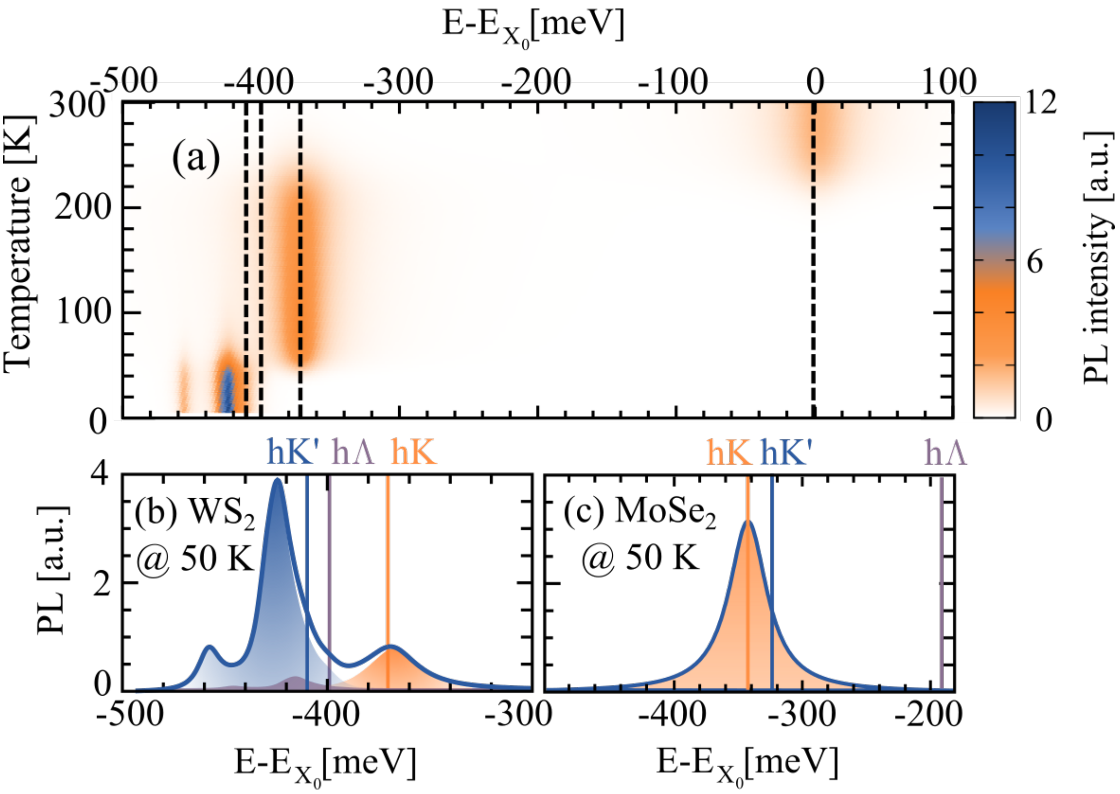

Figure 7.4: **Dark interlayer excitons.** (a) Temperature-dependent PL of WS$_2$/Tc- heterostructure exhibiting signature from intra- and interlayer excitons. Note that the origin of the energy axis has been shifted to the position of the bright KK exciton (E_{X_0}). (b) Contributions of the phonon-assisted PL from different states. (c) Low temperature PL for MoSe$_2$ which shows no phonon-assisted PL.

tra shifted to the position of the bright intralayer exciton) and the bright hK interlayer exciton is traceable around 370 meV below but with a weak oscillator strength of about 5 % of the bright intralayer one.

(ii) **Bright interlayer regime.** Going to lower temperatures, now the hK interlayer excitons becomes more and more pronounced and dominates the spectra from 250 down to around 60K.

(iii) **Dark interlayer regime.** For very low temperatures T< 60 K the spectra is dominated by dark interlayer peaks between -410 and -460 meV.

Before we focus more on the interlayer regimes, we want to compare our results with room temperature PL from experiments. With our results, we confirm a recent experimental observation that interlayer excitons in WS$_2$/Tc heterostructures are visible even at room temperature [102]. Our results are in a very good agreement with these experimental findings, both for the energetic position (320 meV below) and intensity ratio (4 % of the bright exciton PL).

Motivated by these findings, we predict even more interesting low temperature PL which has not been done in experiments. While the increase in oscillator strength of the bright interlayer exciton is something one would expect due to higher occupation of those states with lower temperatures, dark interlayer excitons have yet not been discussed in literature, which makes them especially interesting.

Therefore, Fig. 7.4(b) shows the low temperature PL (50 K) of WS_2 with contributions from different excitons. We find that the main contribution stems from the hK′ exciton (blue shaded curve) while the hΛ exciton has only little contributions (purple shaded area). Note that the position of the peaks does not correspond to the dark excitons energies (vertical lines) but is shifted by 10-30 meV which contributes to the phonon energies involved in this process. We trace back the peak around 425 meV to acoustic K phonons and the peak at 460 meV to optical K phonons. The observed low temperature PL behaviour is due to the unique band structure of tungsten based materials with the dark excitons laying energetically below the bright ones. Therefore we expect a similar behaviour for WSe_2/Tc heterostructures. For molybdenum based heterostructures, we do not expect dark interlayer excitons to appear but only the bright hK exciton, see Fig. 7.4(c) for $MoSe_2$ exemplary. Here, the interlayer peak appears 340 meV below the intralayer exciton and can clearly be traced back to bright interlayer hK excitons, cf. orange vertical line. The dark interlayer excitons hK′ and hΛ lie 20 and 150 meV higher, blue and purple lines respectively. Moreover, we find for the room temperature PL of molybdenum based heterostructures no signatures of interlayer excitons as their occupation is lower compared to tungsten based interlayer excitons.
Our findings might motivate future experiments and help to understand the dark interlayer landscape in organic/inorganic heterostructures.

8

Conclusion and Outlook

In this thesis, we investigated the potential to control the optical fingerprint of transition metal dichalcogenides via external parameters, such as strain, molecules, magnetic fields, and impurities.

Motivated by the optimal surface-to-volume ratio in TMDs, their strong light-matter interaction and strongly bound excitons, we studied which effect molecules have on the optical response of the nanomaterial. We propose the activation of dark excitonic states due to a dipole interaction with the molecules, leading to additional peaks in the optical spectra. The position and intensity of the dark peak crucially depends on the molecular characteristics and has potential for sensor applications. In addition, we found that the dark peak is much more pronounced in the photoluminescence signal due to occupation of lower lying dark states. Besides molecules, also phonons and magnetic fields can activate momentum and spin-dark states, respectively.

Beside the direct activation of dark states, we also studied the indirect proof of their existence via the linewidth of the bright exciton resonance. Here, we focused on changes due to strain, and first investigated the strain effect on excitonic binding energies and wave functions which turned out to be rather small. With help of DFT calculations, we were able to calculate strain dependent shifts of dark and bright states that influence the linewidth. Moreover, we were able to explain the TMD material-specific behavior very well, in good agreement with an experimental photoluminescence study.

We find that dark-bright splitting is a crucial quantity for the activation of dark states and for molecule sensing. Our findings suggest that the dark peak is much more sensitive to strain than the bright one. This sensitivity results in clear changes in the optical fingerprint when smallest amounts of strain are applied to the system. Consequently, strain offers a unique opportunity to tune the dark-bright splitting and opens up a possible mechanism for strain sensing. Furthermore, we shed light on the phenomena of localized excitons by using trapping potentials, either induced by local strain gradients or by molecules which locally induce a change in the band structure creating a potential for excitons. Recent experiments have shown that, under certain conditions, spots of the TMD exhibit ultra strong photoluminescence spectra from these so-called localized excitons. We revealed capture dynamics of localized excitons and found, in agreement with experiments, narrow linewidths and low-energy peaks stemming from both bright and dark localized excitons. In the last part, we further looked at a TMD/Tetracene heterostructure and showed the impact of spatially separated interlayer excitons in the optical spectra. While at room temperarure bright interlayer excitons are dominant, dark interlayer excitons become dominant at low temperatures.

This thesis contributes by giving a fundamental understanding of the tunability of the exciton landscape by external parameters, and by showing the TMDs potential for novel technological concepts such as molecular sensors, strain sensors, single photon emitters or organic/inorganic semiconductors for light harvesting applications. Especially when it comes to technical applications, there are still some open questions for the future. For example, it would be interesting to get a deeper understanding of the substrate influence on the exciton landscape - besides the dielectric screening, there might also be lattice strain involved which might crucially influence the band structure of the TMD and hence its performance. Moreover, heterostructures under strain have only very recently become focus of research, and it would be interesting to understand the effect of both internal and external strain on the properties of these structures as well. When it comes to functionalizing the TMD, it would be interesting to study a broader class of molecules. While high-dipole molecules have been a good first attempt, they are rather unique in the chemistry world. Interesting molecules could include environmental relevant molecules, such as carbon dioxide, methane or ozone, or molecules which are related to diseases and where TMDs could be used a sensor. Finally, the trend towards vertical stacking of 2D layers offers a whole new playground both from the experimental and theoretical side, since they offer moire physics and twist-angle dependent optical response. Here, it would be interesting to see the effect of strain, magnetic fields, and molecules on these structures.

Acknowledgements

First of all, I would like to thank my supervisor, Ermin Malic, for the support the last four years. Thanks to your excellent guidance, I could develop myself to become an (almost) independent researcher, and your trust made it possible to travel to amazing conferences around the world from which I have learned a lot.

Jari Kinaret, my examiner, thank you for your feedback during the last years, especially for taking the time to read my thesis and giving constructive and very helpful comments.

I would also like to thank the examination committee, Prof. Libai Huang, Dr. Claudia Backes, Prof. Christoph Langhammer and Prof. Henrik Johannesson, and the faculty opponent, Dr. Andres Castellanos-Gomez, for accepting to be part of my PhD defence.

A big thanks to all current and former members of the Malic group, in especially Samuel, Raül, Daniel, Joakim, Beatriz, Josh, Jamie, Roberto, Roland, Magdulin, Zahra, Marne, David, August, Simon - thank you for many enjoyable lunch breaks, fikas in the sun, and open ears whenever I was stuck or needed a little push in the right direction. It was a pleasure working with you for the last years and I will keep a lot of nice memories from my time in Chalmers. The Berlin group, Malte, Dominik, Gunnar, Florian, Andreas, thank you for fruitful discussions, fun research visits and the possibility to invite me for a seminar talk.

My friends Walter, Sanna, Linda, Lea, Samuel, Raül, Gemma, William and Evelyn, thank you for being around and making life outside work enjoyable with many walks, Colombian breakfasts, fikas and barbecues. Lisa, Lissi, Rese, Tobi,

Tina, Sabrina, Anna, Madlen, Edita - you are like interlayer excitons - even tough spatially separated, we still feel each other.

Finally, I want to thank my family, especially my parents and grandpa, for all their support and interest in my PhD even though my thesis must seem like a mystery for you. Last, I want to thank my own little family, Iván and Camilo, for being there every day, waking up with a smile and getting ice cream and chocolate for me at any time of the day.

Bibliography

[1] Andre K Geim. Nobel lecture: Random walk to graphene. *Reviews of Modern Physics*, 83(3):851, 2011.

[2] Qianwen Wang, Ping Wu, Gengyu Cao, and Min Huang. First-principles study of the structural and electronic properties of MoS_2–WS_2 and MoS_2–$MoTe_2$ monolayer heterostructures. *Journal of Physics D: Applied Physics*, 46(50):505308, 2013.

[3] Thomas Mueller and Ermin Malic. Exciton physics and device application of two-dimensional transition metal dichalcogenide semiconductors. *npj 2D Materials and Applications*, 2(1):1–12, 2018.

[4] Timothy C. Berkelbach, Mark S. Hybertsen, and David R. Reichman. Theory of neutral and charged excitons in monolayer transition metal dichalcogenides. *Physical Review B*, 88:045318, Jul 2013.

[5] Gunnar Berghäuser and Ermin Malic. Analytical approach to excitonic properties of MoS_2. *Physical Review B*, 89:125309, Mar 2014.

[6] M. Kira and S.W. Koch. Many-body correlations and excitonic effects in semiconductor spectroscopy. *Progress in Quantum Electronics*, 30(5):155 – 296, 2006.

[7] Pierluigi Cudazzo, Ilya V. Tokatly, and Angel Rubio. Dielectric screening in two-dimensional insulators: Implications for excitonic and impurity states in graphane. *Physical Review B*, 84:085406, Aug 2011.

[8] Ermin Malic, Janina Maultzsch, Stephanie Reich, and Andreas Knorr. Excitonic Rayleigh scattering spectra of metallic single-walled carbon nanotubes. *Physical Review B*, 82(11):115439, 2010.

[9] Matthias Hirtschulz, Frank Milde, Ermin Malić, Stefan Butscher, Christian Thomsen, Stephanie Reich, and Andreas Knorr. Carbon nanotube bloch equations: A many-body approach to nonlinear and ultrafast optical properties. *Physical Review B*, 77(3):035403, 2008.

[10] Andreas V Stier, Nathan P Wilson, Genevieve Clark, Xiaodong Xu, and Scott A Crooker. Probing the influence of dielectric environment on excitons in monolayer WSe_2: insight from high magnetic fields. *Nano Letters*, 16(11):7054–7060, 2016.

[11] Gunnar Berghäuser and Ermin Malic. Optical properties of functionalized graphene. *physica status solidi (b)*, 250(12):2678–2680, 2013.

[12] Damien Voiry, Anandarup Goswami, Rajesh Kappera, Cecilia de Carvalho Castro e Silva, Daniel Kaplan, Takeshi Fujita, Mingwei Chen, Tewodros Asefa, and Manish Chhowalla. Covalent functionalization of monolayered transition metal dichalcogenides by phase engineering. *Nature Chemistry*, 7(1):45–49, 2015.

[13] Yunxia Yuan, Runqing Li, and Zhihong Liu. Establishing water-soluble layered WS_2 nanosheet as a platform for biosensing. *Analytical Chemistry*, 86(7):3610–3615, 2014.

[14] Yuan Yong, Liangjun Zhou, Zhanjun Gu, Liang Yan, Gan Tian, Xiaopeng Zheng, Xiaodong Liu, Xiao Zhang, Junxin Shi, Wenshu Cong, et al. WS_2 nanosheet as a new photosensitizer carrier for combined photodynamic and photothermal therapy of cancer cells. *Nanoscale*, 6(17):10394–10403, 2014.

[15] Alexey Chernikov, Timothy C. Berkelbach, Heather M. Hill, Albert Rigosi, Yilei Li, Ozgur Burak Aslan, David R. Reichman, Mark S. Hybertsen, and Tony F. Heinz. Exciton binding energy and nonhydrogenic Rydberg series in monolayer WS_2. *Physical Review Letters*, 113:076802, Aug 2014.

[16] Keliang He, Nardeep Kumar, Liang Zhao, Zefang Wang, Kin Fai Mak, Hui Zhao, and Jie Shan. Tightly bound excitons in monolayer WSe_2. *Physical review letters*, 113(2):026803, 2014.

[17] Ashwin Ramasubramaniam. Large excitonic effects in monolayers of molybdenum and tungsten dichalcogenides. *Physical Review B*, 86:115409, Sep 2012.

[18] Jessica Lindlau, Cedric Robert, Victor Funk, Jonathan Förste, Michael Förg, Léo Colombier, Andre Neumann, Emmanuel Courtade, Shivangi Shree, Takashi Taniguchi, et al. Identifying optical signatures of momentum-dark excitons in transition metal dichalcogenide monolayers. *arXiv preprint arXiv:1710.00988*, 2017.

[19] Jessica Lindlau, Malte Selig, Andre Neumann, Léo Colombier, Jonathan Förste, Victor Funk, Michael Förg, Jonghwan Kim, Gunnar Berghäuser, Takashi Taniguchi, et al. The role of momentum-dark excitons in the elementary optical response of bilayer WSe_2. *Nature Communications*, 9(1):2586, 2018.

[20] MR Molas, Clement Faugeras, AO Slobodeniuk, Karol Nogajewski, Miroslav Bartos, DM Basko, and Marek Potemski. Brightening of dark excitons in monolayers of semiconducting transition metal dichalcogenides. *2D Materials*, 4(2):021003, 2017.

[21] You Zhou, Giovanni Scuri, Dominik S Wild, Alexander A High, Alan Dibos, Luis A Jauregui, Chi Shu, Kristiaan De Greve, Kateryna Pistunova, Andrew Y Joe, et al. Probing dark excitons in atomically thin semiconductors via near-field coupling to surface plasmon polaritons. *Nature Nanotechnology*, 12(9):856, 2017.

[22] Wei-Ting Hsu, Li-Syuan Lu, Dean Wang, Jing-Kai Huang, Ming-Yang Li, Tay-Rong Chang, Yi-Chia Chou, Zhen-Yu Juang, Horng-Tay Jeng, Lain-Jong Li, et al. Evidence of indirect gap in monolayer WSe_2. *Nature Communications*, 8(1):929, 2017.

[23] Ermin Malic, Malte Selig, Maja Feierabend, Samuel Brem, Dominik Christiansen, Florian Wendler, Andreas Knorr, and Gunnar Berghäuser. Dark excitons in transition metal dichalcogenides. *Physical Review Materials*, 2(1):014002, 2018.

[24] Gunnar Berghäuser, Philipp Steinleitner, Philipp Merkl, Rupert Huber, Andreas Knorr, and Ermin Malic. Mapping of the dark exciton landscape in transition metal dichalcogenides. *Physical Review B*, 98(2):020301, 2018.

[25] Malte Selig, Gunnar Berghäuser, Marten Richter, Rudolf Bratschitsch, Andreas Knorr, and Ermin Malic. Dark and bright exciton formation, thermalization, and photoluminescence in monolayer transition metal dichalcogenides. *2D Materials*, 2018.

[26] Maja Feierabend, Gunnar Berghäuser, Andreas Knorr, and Ermin Malic. Proposal for dark exciton based chemical sensors. *Nature Communications*, 8:14776, 2017.

[27] Dominik Christiansen, Malte Selig, Gunnar Berghäuser, Robert Schmidt, Iris Niehues, Robert Schneider, Ashish Arora, Steffen Michaelis de Vasconcellos, Rudolf Bratschitsch, Ermin Malic, et al. Phonon sidebands in monolayer transition metal dichalcogenides. *Physical Review Letters*, 119(18):187402, 2017.

[28] Gunnar Berghäuser, Philipp Steinleitner, Philipp Merkl, Rupert Huber, Andreas Knorr, and Ermin Malic. Mapping of the dark exciton landscape in transition metal dichalcogenides. *Physical Review B*, 98(2):020301, 2018.

[29] J Jadczak, J Kutrowska-Girzycka, P Kapuściński, YS Huang, A Wójs, and L Bryja. Probing of free and localized excitons and trions in atomically thin WSe_2 , WS_2 , $MoSe_2$ and MoS_2 in photoluminescence and reflectivity experiments. *Nanotechnology*, 28(39):395702, 2017.

[30] Philipp Tonndorf, Robert Schmidt, Robert Schneider, Johannes Kern, Michele Buscema, Gary A Steele, Andres Castellanos-Gomez, Herre SJ van der Zant, Steffen Michaelis de Vasconcellos, and Rudolf Bratschitsch. Single-photon emission from localized excitons in an atomically thin semiconductor. *Optica*, 2(4):347–352, 2015.

[31] Carmen Palacios-Berraquero, Dhiren M Kara, Alejandro R-P Montblanch, Matteo Barbone, Pawel Latawiec, Duhee Yoon, Anna K Ott, Marko Loncar, Andrea C Ferrari, and Mete Atatüre. Large-scale quantum-emitter arrays in atomically thin semiconductors. *Nature Communications*, 8:15093, 2017.

[32] Hartmut Haug and Stephan W Koch. *Quantum theory of the optical and electronic properties of semiconductors: fifth edition*. World Scientific Publishing Company, 2009.

[33] A. Knorr, S. Hughes, T. Stroucken, and S.W. Koch. Theory of ultrafast spatio-temporal dynamics in semiconductor heterostructures. *Chemical Physics*, 210(1–2):27 – 47, 1996. Confined Excitations in Molecular and Semiconductor Nanostructures.

[34] Malte Selig, Gunnar Berghäuser, Archana Raja, Philipp Nagler, Christian Schüller, Tony F Heinz, Tobias Korn, Alexey Chernikov, Ermin Malic, and Andreas Knorr. Excitonic linewidth and coherence lifetime in monolayer transition metal dichalcogenides. *Nature Communications*, 7:13279, 2016.

[35] Di Xiao, Gui-Bin Liu, Wanxiang Feng, Xiaodong Xu, and Wang Yao. Coupled spin and valley physics in monolayers of MoS_2 and other group-vi dichalcogenides. *Physical Review Letters*, 108:196802, May 2012.

[36] H. Ochoa and R. Roldán. Spin-orbit-mediated spin relaxation in monolayer MoS_2. *Physical Review B*, 87:245421, Jun 2013.

[37] Gunnar Berghäuser, Andreas Knorr, and Ermin Malic. Optical fingerprint of dark 2p-states in transition metal dichalcogenides. *2D Materials*, 4(1):015029, 2016.

[38] E Malic, A Setaro, P Bluemmel, Carlos F Sanz-Navarro, Pablo Ordejón, S Reich, and A Knorr. Carbon nanotubes as substrates for molecular spiropyran-based switches. *Journal of Physics: Condensed Matter*, 24(39):394006, 2012.

[39] Dong Hoon Keum, Suyeon Cho, Jung Ho Kim, Duk-Hyun Choe, Ha-Jun Sung, Min Kan, Haeyong Kang, Jae-Yeol Hwang, Sung Wng Kim, Heejun Yang, et al. Bandgap opening in few-layered monoclinic $MoTe_2$. *Nature Physics*, 11(6):482, 2015.

[40] Graeme Cunningham, Damien Hanlon, Niall McEvoy, Georg S Duesberg, and Jonathan N Coleman. Large variations in both dark-and photoconductivity in nanosheet networks as nanomaterial is varied from MoS_2 to WTe_2. *Nanoscale*, 7(1):198–208, 2015.

[41] Andor Kormanyos, Guido Burkard, Martin Gmitra, Jaroslav Fabian, Viktor Zolyomi, Neil D Drummond, and Vladimir Falko. $\mathbf{k} \cdot \mathbf{p}$ theory for two-dimensional transition metal dichalcogenide semiconductors. *2D Materials*, 2(2):022001, 2015.

[42] Rafael Roldán, Jose A Silva-Guillén, M Pilar López-Sancho, Francisco Guinea, Emmanuele Cappelluti, and Pablo Ordejón. Electronic properties of single-layer and multilayer transition metal dichalcogenides MX_2 (M= Mo, W and X= S, Se). *Annalen der Physik*, 526(9-10):347–357, 2014.

[43] Ermin Malic and Andreas Knorr. *Graphene and Carbon Nanotubes: Ultrafast Optics and Relaxation Dynamics*. John Wiley & Sons, 2013.

[44] A Thränhardt, S Kuckenburg, A Knorr, T Meier, and SW Koch. Quantum theory of phonon-assisted exciton formation and luminescence in semiconductor quantum wells. *Physical Review B*, 62(4):2706, 2000.

[45] A Steinhoff, M Rosner, F Jahnke, TO Wehling, and C Gies. Influence of excited carriers on the optical and electronic properties of MoS_2. *Nano Letters*, 14(7):3743–3748, 2014.

[46] Raül Perea-Causín, Samuel Brem, and Ermin Malic. Microscopic modeling of pump–probe spectroscopy and population inversion in transition metal dichalcogenides. *physica status solidi (b)*, 257(12):2000223, 2020.

[47] Natalia S Rytova. Screened potential of a point charge in a thin film. *Moscow University Physics Bulletin 3, 30*, 1967.

[48] LV Keldysh. Coulomb interaction in thin semiconductor and semimetal films. *JETPL*, 29:658, 1979.

[49] Gunnar Berghäuser, Ivan Bernal-Villamil, Robert Schmidt, Robert Schneider, Iris Niehues, Paul Erhart, Steffen Michaelis de Vasconcellos, Rudolf Bratschitsch, Andreas Knorr, and Ermin Malic. Inverted valley polarization in optically excited transition metal dichalcogenides. *Nature Communications*, 9(1):971, 2018.

[50] Ivan Bernal-Villamil, Gunnar Berghäuser, Malte Selig, Iris Niehues, Robert Schmidt, Robert Schneider, Philipp Tonndorf, Paul Erhart, Steffen Michaelis de Vasconcellos, Rudolf Bratschitsch, et al. Exciton broadening and band renormalization due to dexter-like intervalley coupling. *2D Materials*, 5(2):025011, 2018.

[51] Chung-Huai Chang, Xiaofeng Fan, Shi-Hsin Lin, and Jer-Lai Kuo. Orbital analysis of electronic structure and phonon dispersion in MoS_2, $MoSe_2$, WS_2, and WSe_2 monolayers under strain. *Physical Review B*, 88(19):195420, 2013.

[52] Qu Yue, Jun Kang, Zhengzheng Shao, Xueao Zhang, Shengli Chang, Guang Wang, Shiqiao Qin, and Jingbo Li. Mechanical and electronic properties of monolayer MoS_2 under elastic strain. *Phys. Lett. A*, 376(12):1166–1170, 2012.

[53] Akshay Singh, Andreas Knorr, Chandriker Kavir Dass, Chang-Hsiao Chen, Ermin Malic, Galan Moody, Genevieve Clark, Gunnar Berghäuser, Kai Hao, Kha Tran, et al. Intrinsic homogeneous linewidth and broadening mechanisms of excitons in monolayer transition metal dichalcogenides. *Nature Communications*, 6:8315, 2015.

[54] Maciej Koperski, Maciej R Molas, Ashish Arora, Karol Nogajewski, Miroslav Bartos, Jan Wyzula, Diana Vaclavkova, Piotr Kossacki, and Marek Potemski. Orbital, spin and valley contributions to Zeeman splitting of excitonic resonances in $MoSe_2$, WSe_2 and WS_2 monolayers. *2D Materials*, 6(1):015001, 2018.

[55] Maja Feierabend, Gunnar Berghäuser, Malte Selig, Samuel Brem, Timur Shegai, Siegfried Eigler, and Ermin Malic. Molecule signatures in photoluminescence spectra of transition metal dichalcogenides. *Physical Review Materials*, 2(1):014004, 2018.

[56] Maja Feierabend, Ermin Malic, Andreas Knorr, and Gunnar Berghäuser. Optical fingerprint of non-covalently functionalized transition metal dichalcogenides. *J. Phys.: Condens. Matter*, 29(38):384003, 2017.

[57] Samuel Brem, August Ekman, Dominik Christiansen, Florian Katsch, Malte Selig, Cedric Robert, Xavier Marie, Bernhard Urbaszek, Andreas

Knorr, and Ermin Malic. Phonon-assisted photoluminescence from indirect excitons in monolayers of transition-metal dichalcogenides. *Nano Letters*, 20(4):2849–2856, 2020.

[58] Andreas Hirsch and Otto Vostrowsky. *Functional Molecular Nanostructures*. Springer Berlin Heidelberg, Berlin, Heidelberg, 2005.

[59] E. Malic, C. Weber, M. Richter, V. Atalla, T. Klamroth, P. Saalfrank, S. Reich, and A. Knorr. Microscopic model of the optical absorption of carbon nanotubes functionalized with molecular spiropyran photoswitches. *Physical Review Letters*, 106(9):097401, March 2011.

[60] Gunnar Berghäuser and Ermin Malic. Molecule–substrate interaction in functionalized graphene. *Carbon*, 69:536 – 542, 2014.

[61] Kazuma Tsuboi, Kazuhiko Seki, Yukio Ouchi, Katsuhiko Fujita, and Kotaro Kajikawa. Formation of merocyanine self-assembled monolayer and its nonlinear optical properties probed by second-harmonic generation and surface plasmon resonance. *Japanese Journal of Applied Physics*, 42(2R):607, 2003.

[62] Qing Hua Wang, Kourosh Kalantar-Zadeh, Andras Kis, Jonathan N Coleman, and Michael S Strano. Electronics and optoelectronics of two-dimensional transition metal dichalcogenides. *Nature Nanotechnology*, 7(11):699, 2012.

[63] Lutz Waldecker, Archana Raja, Roland Koch, Aaron Bostwick, Chris Jozwiak, Eli Rotenberg, and Tony Heinz. Bandgap renormalization and band offset in 2d materials caused by dielectric screening. *Bulletin of the American Physical Society*, 2018.

[64] Aïda Hichri, Imen Ben Amara, Sabrine Ayari, and Sihem Jaziri. Exciton center-of-mass localization and dielectric environment effect in monolayer WS_2. *Journal of Applied Physics*, 121(23):235702, 2017.

[65] Samuel Brem, Malte Selig, Gunnar Berghaeuser, and Ermin Malic. Exciton relaxation cascade in two-dimensional transition metal dichalcogenides. *Scientific Reports*, 8(1):8238, 2018.

[66] Zhenghe Jin, Xiaodong Li, Jeffrey T Mullen, and Ki Wook Kim. Intrinsic transport properties of electrons and holes in monolayer transition-metal dichalcogenides. *Physical Review B*, 90(4):045422, 2014.

[67] W Hoyer, C Ell, M Kira, SW Koch, S Chatterjee, S Mosor, G Khitrova, HM Gibbs, and H Stolz. Many-body dynamics and exciton formation studied by time-resolved photoluminescence. *Physical Review B*, 72(7):075324, 2005.

[68] Ajit Srivastava, Meinrad Sidler, Adrien V Allain, Dominik S Lembke, Andras Kis, and A Imamoğlu. Valley Zeeman effect in elementary optical excitations of monolayer WSe_2. *Nature Physics*, 11(2):141–147, 2015.

[69] Yilei Li, Jonathan Ludwig, Tony Low, Alexey Chernikov, Xu Cui, Ghidewon Arefe, Young Duck Kim, Arend M Van Der Zande, Albert Rigosi, Heather M Hill, et al. Valley splitting and polarization by the Zeeman effect in monolayer $MoSe_2$. *Physical review letters*, 113(26):266804, 2014.

[70] Andreas V Stier, Kathleen M McCreary, Berend T Jonker, Junichiro Kono, and Scott A Crooker. Exciton diamagnetic shifts and valley Zeeman effects in monolayer WS_2 and MoS_2 to 65 Tesla. *Nature communications*, 7(1):1–8, 2016.

[71] Florian Katsch, Malte Selig, Alexander Carmele, and Andreas Knorr. Theory of exciton–exciton interactions in monolayer transition metal dichalcogenides. *physica status solidi (b)*, 255(12):1800185, 2018.

[72] Xiao-Xiao Zhang, Ting Cao, Zhengguang Lu, Yu-Chuan Lin, Fan Zhang, Ying Wang, Zhiqiang Li, James C Hone, Joshua A Robinson, Dmitry Smirnov, et al. Magnetic brightening and control of dark excitons in monolayer WSe_2. *Nature Nanotechnology*, 12(9):883, 2017.

[73] Vanik Shahnazaryan, Ivan Iorsh, IA Shelykh, and O Kyriienko. Exciton-exciton interaction in transition-metal dichalcogenide monolayers. *Physical Review B*, 96(11):115409, 2017.

[74] Iris Niehues, Robert Schmidt, Matthias Drüppel, Philipp Marauhn, Dominik Christiansen, Malte Selig, Gunnar Berghäuser, Daniel Wigger, Robert Schneider, Lisa Braasch, et al. Strain control of exciton–phonon coupling in atomically thin semiconductors. *Nano Letters*, 18(3):1751–1757, 2018.

[75] Minhoon Park, Yong Ju Park, Xiang Chen, Yon-Kyu Park, Min-Seok Kim, and Jong-Hyun Ahn. MoS_2-based tactile sensor for electronic skin applications. *Advanced Materials*, 28(13):2556–2562, 2016.

[76] Meng-Yen Tsai, Alexey Tarasov, Zohreh R Hesabi, Hossein Taghinejad, Philip M Campbell, Corey A Joiner, Ali Adibi, and Eric M Vogel. Flexible MoS_2 field-effect transistors for gate-tunable piezoresistive strain sensors. *ACS Applied Materials & Interfaces*, 7(23):12850–12855, 2015.

[77] F Cadiz, E Courtade, C Robert, G Wang, Y Shen, H Cai, T Taniguchi, K Watanabe, H Carrere, D Lagarde, et al. Excitonic linewidth approaching the homogeneous limit in MoS_2-based van der Waals heterostructures. *Physical Review X*, 7(2):021026, 2017.

[78] Chitraleema Chakraborty, Laura Kinnischtzke, Kenneth M Goodfellow, Ryan Beams, and A Nick Vamivakas. Voltage-controlled quantum light from an atomically thin semiconductor. *Nature Nanotechnology*, 10(6):507, 2015.

[79] M Koperski, K Nogajewski, A Arora, V Cherkez, P Mallet, J-Y Veuillen, J Marcus, P Kossacki, and M Potemski. Single photon emitters in exfoliated WSe_2 structures. *Nature Nanotechnology*, 10(6):503, 2015.

[80] Yu-Ming He, Genevieve Clark, John R Schaibley, Yu He, Ming-Cheng Chen, Yu-Jia Wei, Xing Ding, Qiang Zhang, Wang Yao, Xiaodong Xu, et al. Single quantum emitters in monolayer semiconductors. *Nature Nanotechnology*, 10(6):497, 2015.

[81] Ajit Srivastava, Meinrad Sidler, Adrien V Allain, Dominik S Lembke, Andras Kis, and A Imamoğlu. Optically active quantum dots in monolayer WSe_2. *Nature Nanotechnology*, 10(6):491, 2015.

[82] Saboura Salehi and Alireza Saffarzadeh. Atomic defect states in monolayers of MoS_2 and WS_2. *Surface Science*, 651:215–221, 2016.

[83] Shuai Zhang, Chen-Guang Wang, Ming-Yang Li, Di Huang, Lain-Jong Li, Wei Ji, and Shiwei Wu. Defect structure of localized excitons in a WSe_2 monolayer. *Physical review letters*, 119(4):046101, 2017.

[84] Sivan Refaely-Abramson, Diana Y Qiu, Steven G Louie, and Jeffrey B Neaton. Defect-induced modification of low-lying excitons and valley selectivity in monolayer transition metal dichalcogenides. *Physical review letters*, 121(16):167402, 2018.

[85] Laxmi Narayan Tripathi, Oliver Iff, Simon Betzold, Łukasz Dusanowski, Monika Emmerling, Kihwan Moon, Young Jin Lee, Soon-Hong Kwon, Sven Höfling, and Christian Schneider. Spontaneous emission enhancement in strain-induced WSe_2 monolayer-based quantum light sources on metallic surfaces. *ACS Photonics*, 5(5):1919–1926, 2018.

[86] Yu-Ming He, Sven Höfling, and Christian Schneider. Phonon induced line broadening and population of the dark exciton in a deeply trapped localized emitter in monolayer WSe_2. *Optics express*, 24(8):8066–8073, 2016.

[87] Daniel F Walls and Gerard J Milburn. *Quantum optics*. Springer Science & Business Media, 2007.

[88] Conyers Herring. A new method for calculating wave functions in crystals. *Physical Review*, 57(12):1169, 1940.

[89] HC Schneider, WW Chow, and Stephan W Koch. Influence of coupling between localized and continuum states in ingan quantum-dot systems. *physica status solidi (b)*, 238(3):589–592, 2003.

[90] J Klein, M Lorke, M Florian, F Sigger, L Sigl, S Rey, J Wierzbowski, J Cerne, K Müller, E Mitterreiter, et al. Site-selectively generated photon emitters in monolayer MoS_2 via local helium ion irradiation. *Nature communications*, 10(1):1–8, 2019.

[91] KS Novoselov, o A Mishchenko, o A Carvalho, and AH Castro Neto. 2d materials and van der Waals heterostructures. *Science*, 353(6298), 2016.

[92] Andre K Geim and Irina V Grigorieva. Van der Waals heterostructures. *Nature*, 499(7459):419–425, 2013.

[93] Yuan Liu, Nathan O Weiss, Xidong Duan, Hung-Chieh Cheng, Yu Huang, and Xiangfeng Duan. Van der Waals heterostructures and devices. *Nature Reviews Materials*, 1(9):1–17, 2016.

[94] Miguel M Ugeda, Aaron J Bradley, Su-Fei Shi, H Felipe, Yi Zhang, Diana Y Qiu, Wei Ruan, Sung-Kwan Mo, Zahid Hussain, Zhi-Xun Shen, et al. Giant bandgap renormalization and excitonic effects in a monolayer transition metal dichalcogenide semiconductor. *Nature materials*, 13(12):1091, 2014.

[95] Gang Wang, Alexey Chernikov, Mikhail M Glazov, Tony F Heinz, Xavier Marie, Thierry Amand, and Bernhard Urbaszek. Colloquium: Excitons in atomically thin transition metal dichalcogenides. *Reviews of Modern Physics*, 90(2):021001, 2018.

[96] Xiao-Xiao Zhang, Yumeng You, Shu Yang Frank Zhao, and Tony F Heinz. Experimental evidence for dark excitons in monolayer WSe_2. *Physical Review Letters*, 115(25):257403, 2015.

[97] Pasqual Rivera, John R Schaibley, Aaron M Jones, Jason S Ross, Sanfeng Wu, Grant Aivazian, Philip Klement, Kyle Seyler, Genevieve Clark, Nirmal J Ghimire, et al. Observation of long-lived interlayer excitons in monolayer $MoSe_2$–WSe_2 heterostructures. *Nature communications*, 6(1):1–6, 2015.

[98] Bastian Miller, Alexander Steinhoff, Borja Pano, Julian Klein, Frank Jahnke, Alexander Holleitner, and Ursula Wurstbauer. Long-lived direct and indirect interlayer excitons in van der Waals heterostructures. *Nano letters*, 17(9):5229–5237, 2017.

[99] Philipp Merkl, Fabian Mooshammer, Philipp Steinleitner, Anna Girnghuber, K-Q Lin, Philipp Nagler, Johannes Holler, Christian Schüller, John M

Lupton, Tobias Korn, et al. Ultrafast transition between exciton phases in van der Waals heterostructures. *Nature materials*, 18(7):691–696, 2019.

[100] Xiaoping Hong, Jonghwan Kim, Su-Fei Shi, Yu Zhang, Chenhao Jin, Yinghui Sun, Sefaattin Tongay, Junqiao Wu, Yanfeng Zhang, and Feng Wang. Ultrafast charge transfer in atomically thin MoS_2/WS_2 heterostructures. *Nature Nanotechnology*, 9(9):682, 2014.

[101] Jens Kunstmann, Fabian Mooshammer, Philipp Nagler, Andrey Chaves, Frederick Stein, Nicola Paradiso, Gerd Plechinger, Christoph Strunk, Christian Schüller, Gotthard Seifert, et al. Momentum-space indirect interlayer excitons in transition-metal dichalcogenide van der Waals heterostructures. *Nature Physics*, 14(8):801–805, 2018.

[102] Tong Zhu, Long Yuan, Yan Zhao, Mingwei Zhou, Yan Wan, Jianguo Mei, and Libai Huang. Highly mobile charge-transfer excitons in two-dimensional WS_2/tetracene heterostructures. *Science advances*, 4(1):eaao3104, 2018.

[103] Tobias Breuer, Tobias Maßmeyer, Alexander Mänz, Steffen Zoerb, Bernd Harbrecht, and Gregor Witte. Structure of van der Waals bound hybrids of organic semiconductors and transition metal dichalcogenides: the case of acene films on MoS_2. *physica status solidi (RRL)–Rapid Research Letters*, 10(12):905–910, 2016.

[104] Xiao-Ying Xie, Xiang-Yang Liu, Qiu Fang, Wei-Hai Fang, and Ganglong Cui. Photoinduced carrier dynamics at the interface of pentacene and molybdenum disulfide. *The Journal of Physical Chemistry A*, 123(36):7693–7703, 2019.

[105] Jose CS Costa, Ricardo JS Taveira, Carlos FRAC Lima, Adelio Mendes, and Luís MNBF Santos. Optical band gaps of organic semiconductor materials. *Optical Materials*, 58:51–60, 2016.

[106] Hongwei Li, Zhuo Dong, Yan Zhang, Liqiang Li, Zhongchang Wang, Cong Wang, Kai Zhang, and Han Zhang. Recent progress and strategies in photodetectors based on 2d inorganic/organic heterostructures. *2D Materials*, 8(1):012001, 2020.

[107] Marco Gobbi, Emanuele Orgiu, and Paolo Samorì. When 2d materials meet molecules: opportunities and challenges of hybrid organic/inorganic van der Waals heterostructures. *Advanced Materials*, 30(18):1706103, 2018.

[108] Gwan-Hyoung Lee, Chul-Ho Lee, Arend M Van Der Zande, Minyong Han, Xu Cui, Ghidewon Arefe, Colin Nuckolls, Tony F Heinz, James

Hone, and Philip Kim. Heterostructures based on inorganic and organic van der Waals systems. *Apl Materials*, 2(9):092511, 2014.

[109] T Feldtmann, M Kira, and Stephan W Koch. Phonon sidebands in semiconductor luminescence. *physica status solidi (b)*, 246(2):332–336, 2009.

[110] T Feldtmann, M Kira, and Stephan W Koch. Theoretical analysis of higher-order phonon sidebands in semiconductor luminescence spectra. *Journal of luminescence*, 130(1):107–113, 2010.

[111] A Chernikov, V Bornwasser, M Koch, S Chatterjee, CN Böttge, T Feldtmann, M Kira, SW Koch, T Wassner, S Lautenschläger, et al. Phonon-assisted luminescence of polar semiconductors: Fröhlich coupling versus deformation-potential scattering. *Physical Review B*, 85(3):035201, 2012.

[112] S Shree, M Semina, Cédric Robert, B Han, Thierry Amand, Andrea Balocchi, M Manca, E Courtade, X Marie, T Taniguchi, et al. Observation of exciton-phonon coupling in $MoSe_2$ monolayers. *Physical Review B*, 98(3):035302, 2018.

[113] Manabu Ohtomo, Tadamasa Suzuki, Toshihiro Shimada, and Tetsuya Hasegawa. Band dispersion of quasi-single crystal thin film phase pentacene monolayer studied by angle-resolved photoelectron spectroscopy. *Applied Physics Letters*, 95(12):258, 2009.

[114] GN Gavrila, H Mendez, TU Kampen, DRT Zahn, DV Vyalikh, and W Braun. Energy band dispersion in well ordered N, N′-dimethyl-3, 4, 9, 10-perylenetetracarboxylic diimide films. *Applied physics letters*, 85(20):4657–4659, 2004.

[115] Simon Ovesen, Samuel Brem, Christopher Linderälv, Mikael Kuisma, Tobias Korn, Paul Erhart, Malte Selig, and Ermin Malic. Interlayer exciton dynamics in van der Waals heterostructures. *Communications Physics*, 2(1):1–8, 2019.

[116] Akash Laturia, Maarten L Van de Put, and William G Vandenberghe. Dielectric properties of hexagonal boron nitride and transition metal dichalcogenides: from monolayer to bulk. *npj 2D Materials and Applications*, 2(1):1–7, 2018.

[117] O Leenaerts, B Partoens, and FM Peeters. Adsorption of H_2O, NH_3, CO, NO_2, and NO on graphene: A first-principles study. *Physical Review B*, 77(12):125416, 2008.

[118] Robert D Miller. In search of low-k dielectrics. *Science*, 286(5439):421–423, 1999.

[119] K Doi, K Yoshida, H Nakano, A Tachibana, T Tanabe, Y Kojima, and K Okazaki. Ab initio calculation of electron effective masses in solid pentacene. *Journal of applied physics*, 98(11):113709, 2005.

[120] Samuel Brem, Kai-Qiang Lin, Roland Gillen, Jonas M Bauer, Janina Maultzsch, John M Lupton, and Ermin Malic. Hybridized intervalley moiré excitons and flat bands in twisted WSe_2 bilayers. *Nanoscale*, 12(20):11088–11094, 2020.

[121] Peng Hu, Henan Li, Yongxin Li, Hui Jiang, and Christian Kloc. Single-crystal growth, structures, charge transfer and transport properties of anthracene-F_4TCNQ and tetracene-F_4TCNQ charge-transfer compounds. *CrystEngComm*, 19(4):618–624, 2017.

[122] David A Ruiz-Tijerina and Vladimir I Fal'ko. Interlayer hybridization and moiré superlattice minibands for electrons and excitons in heterobilayers of transition-metal dichalcogenides. *Physical Review B*, 99(12):125424, 2019.

[123] Yong Wang, Zhan Wang, Wang Yao, Gui-Bin Liu, and Hongyi Yu. Interlayer coupling in commensurate and incommensurate bilayer structures of transition-metal dichalcogenides. *Physical Review B*, 95(11):115429, 2017.

[124] Samuel Brem, Christopher Linderälv, Paul Erhart, and Ermin Malic. Tunable phases of moiré excitons in van der Waals heterostructures. *Nano letters*, 20(12):8534–8540, 2020.